Title

Linkage Between Stratospheric Variability and North American Surface Air Temperature

Author

Ding, Xiuyuan

Publication Date

2024

Peer reviewed|Thesis/dissertation

UNIVERSITY OF CALIFORNIA

Los Angeles

Linkage Between Stratospheric Variability and North American Surface Air Temperature

A dissertation submitted in partial satisfaction

of the requirements for the degree

Doctor of Philosophy in Atmospheric and Oceanic Sciences

by

Xiuyuan Ding

2024

ABSTRACT OF THE DISSERTATION

Linkage Between Stratospheric Variability and North American Surface Air Temperature

by

Xiuyuan Ding

Doctor of Philosophy in Atmospheric and Oceanic Sciences

University of California, Los Angeles, 2024

Professor Gang Chen, Chair

North American (NA) surface air temperatures in winter have been suggested to be associated with stratospheric variability, such as sudden stratospheric warmings (SSWs) or extreme stratospheric waves. However, the robustness and underlying mechanisms are not well understood. In particular, further studies are needed to better understand the dynamical processes underlying extreme stratospheric wave events. Yet, analysis is hindered by the limited sample sizes and the difficulty of identifying these wave events. In this dissertation, we show that extreme stratospheric wave activity is accompanied by subseasonal fluctuations between warm and cold spells over North America with reanalyses and a hierarchy of climate

models. Our study identifies a robust precursor of strong stratospheric wave activity for NA cold extremes on subseasonal timescales. Our findings shed light on the dynamical processes underlying extreme stratospheric wave variability, highlighting the role of vertical wave structure in stratosphere-troposphere coupling.

First, we demonstrate that the vertical coupling of extreme stratospheric wave activity is distinct from the well-known anomalous polar vortex events. We measure the stratospheric wave activity using empirical orthogonal function (EOF) analysis of 10 hPa geopotential height. In contrast to the increased persistence of weather regimes following SSWs, we show that extreme stratospheric wave events feature weather transitions between warm and cold spells over North America in reanalyses and climate models with various configurations. Particularly, strong stratospheric wave events are followed by an increased risk of cold extremes over North America 5–25 days later. The NA coldness is more robust following strong stratospheric wave activity than a weak polar vortex.

We further examine the causality between stratospheric wave activity and NA cold extremes with idealized nudging experiments in a climate model with a well-resolved stratosphere. The stratosphere in the nudging run is fully relaxed to its counterpart in a free-running control simulation. By comparing the strong wave events between the two runs, we attribute the observed NA cold anomalies to the strong stratospheric wave activity. Moreover, vertical wave coupling is found to be key to the temperature transition during strong wave events. Further examinations of Coupled Model

Intercomparison Project Phase 6 (CMIP6) reveal large uncertainty in the wave event evolution across individual models. It is found that models with a degraded representation of stratospheric wave structure also show biases in the troposphere during strong wave events.

In order to investigate the role of the Quasi-biennial Oscillation (QBO) in the linkage between extreme stratospheric wave activity and NA temperature, we compare strong wave events during the westerly phase (wQBO) with those during the easterly phase (eQBO). We show that, in contrast to strong stratospheric wave events under wQBO, strong wave events under eQBO do not change the cold risk over North America nor alter the vertical wave structure in the observation. We further examine this QBO dependence in QBO-resolving CMIP6 models, finding that the strong wave events in models are largely insensitive to QBO phases, a possible bias in numerical models.

The dissertation of Xiuyuan Ding is approved.

Rong Fu

Gudrun Magnusdottir

J. David Neelin

Gang Chen, Committee Chair

University of California, Los Angeles

2024

TABLE OF CONTENTS

LIST OF FIGURES

LIST OF TABLES

ACKNOWLEDGMENTS

I would like to thank my advisor, Professor Gang Chen, for teaching me how to conduct scientific research. He is always willing to guide me and give me time to grow. I am grateful for Gang's trust in me, especially during moments when my self-confidence wavered. If I were fortunate enough to become a faculty member, I would benefit greatly from having Gang as my role model. I would look up to him in both doing research and advising students.

I am also profoundly grateful to have Professors Rong Fu, David Neelin, and Gudrun Magnusdottir on my doctoral committee. In particular, I greatly appreciate the discussions with Gudrun Magnusdottir, which inspire part of this thesis. In addition, I would like to thank my collaborators: Lantao Sun, Pengfei Zhang, Daniela Domeisen, and Clara Orbe. I have learned a lot from their constructive feedback and insightful comments. I would also like to thank all the students and postdocs in my research group, especially Weiming Ma and Bowen Ge, for the helpful discussions and feedback.

I would like to thank all the friends I made during the PhD and fellow AOS students. I especially enjoyed frequent hiking trips with Jiarui Liu and many others. I was fortunate to know Donglai Ma, Yidongfang Si, and Jiaqi Shen, who were always generous in helping me and giving suggestions.

I am very thankful to my wife, Liping Wang. I cannot imagine getting through the PhD journey without her. I am greatly indebted to her support, comfort, trust, and all her effort to make it work for us. Her love is my light in the darkness.

Last, I would like to thank my parents for believing in me and supporting my studies in the United States.

VITA

2021-2024	Ph.D. Candidate in Atmospheric and Oceanic Sciences, University of California, Los Angeles, USA
2019-2021	M.S. in Atmospheric and Oceanic Sciences, University of California, Los Angeles, USA
2015-2019	B.S. in Atmospheric Sciences, Lanzhou University, China

PUBLICATIONS

1. **Ding, X.,** Chen, G., Sun, L., & Zhang, P. (2022). Distinct North American Cooling Signatures Following the Zonally Symmetric and Asymmetric Modes of Winter Stratospheric Variability. *Geophysical Research Letters*, *49*(6), e2021GL096076. https://doi.org/10.1029/2021GL096076

2. **Ding, X.,** Chen, G., Zhang, P., Domeisen, D. I. V., & Orbe, C. (2023). Extreme stratospheric wave activity as harbingers of cold events over North America. *Communications Earth & Environment*, *4*(1), 187. https://doi.org/10.1038/s43247-023-00845-y

3. **Ding, X.,** Chen, G., & Ma, W. (2023). Stratosphere-Troposphere Coupling of Extreme Stratospheric Wave Activity in CMIP6 Models. *Journal of Geophysical Research: Atmospheres*, *128*(16), e2023JD038811. https://doi.org/10.1029/2023JD038811

CHAPTER 1

Overview

Anthropogenic global warming is anticipated to reduce wintertime cold extremes (Lorenz et al., 2019; Oldenborgh et al., 2019), yet recent years have witnessed extreme cold events driven by atmospheric dynamics (Cohen et al., 2021, 2023; Johnson et al., 2018; Ma & Zhu, 2019). Particularly, North America has experienced several intense cold air outbreaks in recent years, notably the exceptional 2021 cold wave of February (Doss-Gollin et al., 2021). Due to the tremendous socioeconomic damages caused by these cold events, it is of great interest to understand their potential causes and seek better predictions. Stratospheric variability is known to influence tropospheric weather conditions during boreal winter (e.g., Baldwin et al., 2021; Domeisen, Butler, et al., 2020b; Sigmond et al., 2013). In the winter stratosphere, a powerful cyclonic system termed the polar vortex develops over the polar region as the result of large solar radiation gradients. The strength of a stratospheric polar vortex is also modulated by wave drag due to planetary waves propagating from the troposphere to the stratosphere (e.g., Charney & Drazin, 1961; Matsuno, 1970). Both weak and strong polar vortex events have been shown to influence the troposphere and surface on subseasonal to seasonal timescales (e.g., Baldwin & Dunkerton, 2001; Limpasuvan et al., 2004, 2005).

Several mechanisms are proposed for the stratospheric impacts on the surface, involving different aspects of the planetary wave-zonal flow interaction. Planetary waves propagate upwards into the stratosphere, where waves are absorbed and under certain conditions result in an extremely weak polar vortex, known as sudden stratospheric warming (SSW) (Charney

& Drazin, 1961; Garfinkel et al., 2010; Polvani & Waugh, 2004). Following SSWs, downward propagation of negative zonal wind anomalies may be amplified and sustained by tropospheric synoptic eddy feedbacks (Domeisen et al., 2013; Gerber et al., 2010; Kushner & Polvani, 2004; Martineau et al., 2018; Song & Robinson, 2004; Sun et al., 2012). The surface signals of SSWs are characterized by the negative phase of the Arctic Oscillation (AO) or North Atlantic Oscillation (NAO) and more frequent cold spells in the mid-latitudes, particularly in northern Eurasia (Butler et al., 2017; Domeisen & Butler, 2020; Garfinkel et al., 2017; Hitchcock & Simpson, 2014; Kidston et al., 2015; P. Zhang et al., 2020). However, it is noted that, compared to the Atlantic sector, the Pacific sector tends to be less affected by SSW events (Butler et al., 2017; Greatbatch et al., 2012). An analysis of North American (NA) weather regimes also shows that the regime most strongly associated with NA coldness does not depend on the strength of the stratospheric polar vortex (Lee et al., 2019).

Another mechanism refers to planetary wave reflection in the stratosphere. Upward-propagating waves from the troposphere get reflected downwards and influence the tropospheric circulation (Perlwitz & Harnik, 2003; Shaw & Perlwitz, 2010). The planetary wave reflection is associated with a particular stratospheric basic state that consists of a meridional waveguide and a vertical wave reflecting surface. This vertical wave reflecting surface coincides with a region of negative vertical zonal wind shear (Perlwitz & Harnik, 2003, 2004). In addition, the duration of the upward pulse of wave activity entering the stratosphere is found to be an important factor during wave reflection (Harnik, 2009). Short pulses of wave activity help to create regions of negative vertical zonal wind shear and corresponding downward wave reflection, while long pulses lead to a weak polar vortex. Planetary wave reflection events are linked to a strong stratospheric polar vortex and positive NAO at the surface (Kodera et al., 2013, 2016; Shaw & Perlwitz, 2013).

Other mechanisms for the stratosphere's downward impacts include the role of the residual circulation (Thompson et al., 2006; Yang et al., 2015), remote effects of stratospheric potential vorticity anomalies (Ambaum & Hoskins, 2002; Black, 2002; White et al., 2020), or modulation of tropical deep convection (Collimore et al., 2003; Gray et al., 2018; Liess & Geller, 2012).

Planetary wave reflection events have drawn increasing attention recently due to their connection to NA surface air temperature (e.g., Kretschmer et al., 2018). Particularly, Cohen et al. (2021) argue that a stretched polar vortex in the lower stratosphere, characterized by its horizontal elongation, is linked to NA cold extremes such as the February 2021 Texas cold spell via wave reflection. An important feature of these reflection events is the negative eddy heat flux in the lower stratosphere, which indicates downward wave propagation. Negative extremes of zonal mean eddy heat flux are instantaneously linked to positive NAO and NA cooling, while positive eddy heat flux extremes are linked to negative NAO and Eurasian cooling (Dunn-Sigouin & Shaw, 2018; Shaw et al., 2014; Shaw & Perlwitz, 2013). Messori et al. (2022) further suggest that reflection events featured by regionally negative eddy heat flux relate to the tropospheric evolution from a Pacific Trough regime to an Alaskan Ridge regime, accompanied by a continental-scale temperature decrease over North America. However, Tan and Bao (2020) find no evidence of wave reflection linked with NA cold spells. They argue that the tropospheric circulation regime associated with NA cold spells only acts as a precursor for the suppressed planetary wave-1 (a wave structure with one crest and one trough at a latitude circle) activity in the stratosphere. Ding et al. (2022, 2023), in contrast, show that strong stratospheric wave activity, featured by a pattern of enhanced climatological wave-1 in the stratosphere, precedes positive NAO-like NA cooling at the

surface with a 10-day lag. The divergent conclusions underscore that the surface impacts of stratospheric waves remain an area of active research.

A key challenge in understanding stratosphere-troposphere coupling is the large internal variability in both the stratosphere and troposphere (Afargan-Gerstman et al., 2022; Charlton-Perez et al., 2018; Kolstad et al., 2022). Only about two-thirds of SSWs are followed by visible downward influences characterized by persistent negative AO, and less than a quarter of negative NAO events are preceded by an SSW (Domeisen, 2019). Davis et al. (2022) find that the February 2021 Texas cold spell is largely attributed to unpredictable internal atmospheric variability, with no discernible contribution from the stratosphere. To deal with the limited sample size of events, one approach is to use large ensembles of model simulations. But the role of extreme stratospheric wave variability in NA temperature variability is underexplored in climate models.

Stratospheric wave events have received much less attention than anomalous polar vortex events and SSWs. Potential reasons include the lack of a full understanding of the dynamical processes and the challenge of diagnosing stratospheric wave events consistently in different datasets. Previous studies have identified stratospheric wave events using eddy heat fluxes (Dunn-Sigouin & Shaw, 2015; Messori et al., 2022), time-integrated upward wave activity flux (Reichler & Jucker, 2022), clustered 100 hPa circulation patterns (Cohen et al., 2021; Kretschmer et al., 2018; Liang et al., 2022; Zou et al., 2023), or time-filtered 10 hPa circulation patterns (Shen et al., 2022). However, many of these studies only analyzed reanalyses, and the sensitivities of these methods are unclear when applied to climate models. Besides, events in these studies are often based on the lower-stratospheric circulation patterns that may be strongly related to tropospheric variability, the contribution of

stratospheric variability to NA temperature remains unclear. In this dissertation, I will address the research gaps listed above in the following chapters.

In Chapter 2, we introduce a simple measure to characterize stratospheric wave variability at 10 hPa using empirical orthogonal function (EOF) analysis. We demonstrate that strong stratospheric wave activity is linked with positive NAO-like cold anomalies over North America in about 10 days through a deep planetary wave-1 structure, distinct from a weak polar vortex both in terms of surface patterns and mechanisms. We further examine this linkage between stratospheric waves and NA temperature in models with different configurations, consistently finding more robust NA cooling following strong stratospheric wave activity than a weak polar vortex. These results suggest strong stratospheric wave activity acts as a better predictor for cold spells in the northern U.S. and Canada compared with a weak polar vortex on subseasonal timescales.

In Chapter 3, we first investigate the surface fingerprints of extreme stratospheric wave activity in observations and the historical simulations from 30 models in the Coupled Model Intercomparison Project Phase 6 (CMIP6). We find that both weak and strong wave activity is associated with cold anomalies over North America, but only during strong stratospheric wave events do the stratospheric signals precede the surface coldness. Using nudging experiments, we attribute the observed NA coldness to the strong stratospheric wave activity since the nudging isolates the contribution of the stratosphere. We further demonstrate in observations and nudging simulations that the vertical wave coupling between stratospheric and tropospheric waves is key to the observed weather transition from warm to cold anomalies during strong stratospheric wave events. The findings of this study shed light on

the dynamical mechanism underlying the tropospheric influence of stratospheric waves and lend support to considering stratospheric wave activity in subseasonal predictions.

In Chapter 4, we systematically investigate the stratosphere-troposphere coupling of extreme stratospheric wave events and evaluate their representations in CMIP6 models. Aside from quantifying the risk of both cold and warm extremes associated with extreme stratospheric wave events, we demonstrate the hydroclimate influences by showing the anomalous frequency of atmospheric river (AR) events during the life cycle of stratospheric wave events. We further examine the CMIP6 models and find that models with a degraded representation of stratospheric wave structure exhibit biases in the troposphere during strong stratospheric wave events. We also compare extreme stratospheric wave events with other extreme stratospheric events in the literature, demonstrating that extreme stratospheric wave events are distinct from other stratospheric events. This work suggests that the vertical coupling of extreme stratospheric wave activity should be evaluated in the model representation of stratosphere-troposphere coupling.

In Chapter 5, we explore the potential role of the Quasi-biennial Oscillation (QBO) in the linkage between extreme stratospheric wave activity and NA temperature. By comparing strong wave events during the westerly phase (wQBO) with those during the easterly phase (eQBO), we find that the NA cooling signature following strong wave events depends on the QBO phase in the observation. In contrast to strong stratospheric wave events under wQBO, we show that strong wave events under eQBO do not change the cold risk over North America nor alter the vertical wave structure. We further examine this QBO dependence in QBO-resolving CMIP6 models, finding that the strong wave events in models are largely insensitive to QBO phases, a possible bias in numerical models. These findings add to the

growing body of research on the QBO's global impacts and reveal potential model deficits in representing stratospheric planetary waves.

CHAPTER 2

Distinct North American Cooling Signatures Following the Zonally Symmetric and Asymmetric Modes of Winter Stratospheric Variability

[**Ding, X.,** Chen, G., Sun, L., & Zhang, P. (2022). Distinct North American Cooling Signatures Following the Zonally Symmetric and Asymmetric Modes of Winter Stratospheric Variability. *Geophysical Research Letters*, *49*(6), e2021GL096076.]

Abstract

This paper compares surface signatures of the zonally symmetric and asymmetric modes of stratospheric variability, which describe the strength of the polar vortex and a planetary wave-1 pattern, respectively. Unlike a weak polar vortex followed by negative Arctic Oscillation (AO)–like anomalies, strong stratospheric wave activity features a polar vortex displacement with a deep planetary wave-1 structure, resulting in positive North Atlantic Oscillation (NAO)–like North American cooling in about 10 days. Moreover, the linkage between the stratosphere and surface is examined in two reanalyses and four models of different configurations, which show more robust North American cooling following the displacement of the polar vortex due to strong stratospheric wave activity than the zonally symmetric weakening of the polar vortex. This suggests strong stratospheric wave activity acts as a better predictor for cold spells in the northern U.S. and Canada compared with a weak polar vortex.

2.1 Introduction

While it is expected that severe cold spells would become less frequent under global warming, there were some extreme cold winter events over the Northern Hemisphere in recent decades (e.g., Overland et al., 2021). Particularly, North America has experienced several intense cold air outbreaks in recent years, notably the exceptional 2021 cold wave of February (Doss-Gollin et al., 2021). Due to the tremendous socioeconomic damages caused by these cold events, it is of great interest to understand their potential causes and seek better predictions. Winter stratospheric variability is known to influence tropospheric circulation and thus may provide an important source of predictability for North American cooling on the intraseasonal timescale.

A primary topic of interest is Sudden Stratospheric Warming (SSW), characterized as a rapid weakening of the polar vortex due to the abrupt deceleration or even reversal of circumpolar westerlies in the stratosphere. On the one hand, a large number of studies have documented that SSWs are followed by downward propagation of Northern Annular Mode (NAM) from the stratosphere to the troposphere on the weekly to monthly timescales, with surface signatures featuring the negative phase of Arctic Oscillation (AO) or North Atlantic Oscillation (NAO; Hurrell, 1995) and cooling over Northern Eurasia (e.g., Baldwin et al., 2003; Baldwin & Dunkerton, 2001; Butler et al., 2017; Domeisen, Butler, et al., 2020b; Garfinkel et al., 2017; Hitchcock & Simpson, 2014; Kidston et al., 2015; Sigmond et al., 2013). This downward influence of weak vortex events is generally understood as planetary wave-zonal flow interactions with tropospheric synoptic eddy feedbacks, which is corroborated by mechanistic models of stratosphere-troposphere coupling (Gerber & Polvani, 2009; Kushner & Polvani, 2004; Martineau et al., 2017; Song & Robinson, 2004; Sun et al., 2011, 2012). On

the other hand, the predictability originated from SSWs is limited by the diversity of individual SSWs and strong tropospheric weather variability. Only about two-thirds of SSWs are followed by visible downward influences featured by the negative AO (Charlton-Perez et al., 2018; Domeisen, 2019). The tropospheric signals also vary with the types of SSWs, such as displacement events (the polar vortex displaced off the pole) and split events (the polar vortex splits into two pieces) (Charlton & Polvani, 2007; Maycock & Hitchcock, 2015; Mitchell et al., 2013; Seviour et al., 2016; White et al., 2021).

Stratospheric variability is also characterized by features of stratospheric planetary waves. Shaw and Perlwitz (2013) and Shaw et al. (2014) showed that events with negative stratospheric meridional heat flux are instantaneously linked to the positive phase of NAO, and they further argued that the negative heat flux events are due to planetary wave reflection rather than wave absorption that is typical for weak polar vortex events (Dunn-Sigouin & Shaw, 2018). From the perspective of zonal mean momentum budget for the stratosphere, wave events with anomalous upward/downward wave activity fluxes will cause the deceleration/acceleration of circumpolar westerlies, which, in turn, may lead to weak/strong vortex events (e.g., Dunn-Sigouin & Shaw, 2015). Thus, in terms of zonal mean dynamics, stratospheric events of positive/negative meridional heat flux and weak/strong polar vortex can be thought of as different aspects of the same planetary wave-zonal flow interaction rather than different dynamical mechanisms.

Nevertheless, negative heat flux events are seemingly associated with distinct surface conditions as compared with weak vortex events, especially over the North American sector. Several previous studies have proposed wave reflection as a cause of North American cold spells, by either examining the sign of lower-stratospheric meridional heat flux during the

polar vortex recovery (Kodera et al., 2013, 2016) or using clustering analysis (Kretschmer et al., 2018). They argued that the stratospheric anomalies with positive heat flux involve wave absorption, characterized by the typical downward propagation of NAM signals and the negative phase of AO, and that the anomalies with negative heat flux involve wave reflection, followed by the amplification of blocking over the North Pacific. However, Tan and Bao (2020) found no evidence of wave reflection linked with North American cold spells and argued that the associated tropospheric circulation regime, characterized by Pacific blocking, is the precursor of a displacement in the polar vortex rather than the effect. W. Guan et al. (2020) also found that the leading mode of surface air temperature (SAT) over the North American sector precedes a planetary wave-1 pattern extending from the surface to the stratosphere. Additional work is warranted to better understand the linkage between stratospheric planetary wave activity and North American cooling.

In this paper, we will assess the surface influences of stratospheric variability in observations and climate models, focusing on the leading intraseasonal modes of zonally symmetric and asymmetric components of geopotential height at 10 hPa (denoted as Z10 hereafter). It is found that the zonally asymmetric mode that describes the intensification/weakening of a planetary wave-1 pattern, is followed by distinct surface signatures in SAT and sea level pressure (SLP), as compared with the zonally symmetric mode that characterizes the weakening/strengthening of the polar vortex. These suggest two different mechanisms by which the stratosphere impacts cold spells.

The paper is organized as follows. In section 2.2, we first describe the reanalysis and model datasets and diagnostic methods. Section 2.3 compares distinct surface signatures associated with the two stratospheric modes of variability. A summary is provided in section 2.4.

2.2 Data and Methods

2.2.1 Reanalysis and model data

The intraseasonal variability of the atmosphere is analyzed for the extended boreal winter from November to March. We use daily data from the European Centre for Medium-Range Weather Forecasts (ECMWF) Interim reanalysis (ERA-Interim) in 1979–2017 with a resolution of 0.75°×0.75° for surface data and 1.5°×1.5° for atmospheric data (Dee et al., 2011). After detrending the data, we remove the seasonal cycle, which is defined as the time mean and first two harmonics of the all-year climatology. Then, we subtract the interannual variability represented by the seasonal mean of each winter, and the remaining data describes the intraseasonal variability. Moreover, the same analysis is performed on daily data from Japanese 55-year Reanalysis (JRA-55) in 1958–2020 with a resolution of 1.25°×1.25° for surface and 2.5°×2.5° for atmospheric data (Kobayashi et al., 2015). The longer record in JRA-55 with more SSW events is employed to verify the surface influences of stratospheric variability in ERA-Interim.

We also investigate daily outputs from two sets of atmospheric model experiments, Polar Amplification Model Intercomparison Project (PAMIP; D. M. Smith et al., 2019) and Atmospheric Model Intercomparison Project (AMIP). The PAMIP simulations consist of 100 one-year runs, initialized with the conditions on April 1st, 2000, and driven with the present-day climatology of sea surface temperature (SST) and sea ice concentration (SIC). Because of the fixed surface boundary conditions, differences among ensemble members are due to atmospheric internal variability. Two PAMIP models are compared: version 6 of Community Atmosphere Model (CAM6) from the National Center for Atmospheric Research (NCAR) version 2 of Community Earth System Model (CESM2; Danabasoglu et al., 2020), and the

University of Tokyo version 6 of Model for Interdisciplinary Research on Climate (MIROC6; Tatebe et al., 2019). CAM6 has a horizontal resolution of 0.9°×1.25° and 32 vertical levels with a top level of 2.25hPa. MIROC6 has 256×128 horizontal grids and 81 vertical levels up to 0.004hPa. Meanwhile, the AMIP simulations are driven by historical SST and SIC in 1950–2013. Two versions of CESM2 are examined here: "low-top" CAM6 and "high-top" Whole Atmosphere Community Climate Model (WACCM; Gettelman et al., 2019). The CAM6 simulations in AMIP are run with the same settings as in PAMIP except for more realistic historical forcings. WACCM has 0.9°×1.25° horizontal resolution and 70 vertical levels extending to 4.5e-6hPa. As such, the different configurations in CESM2 help examine the robustness of stratosphere-troposphere coupling in the models. The models we examined are likely too few to make a quantitative conclusion about the difference between low- versus high-top models.

2.2.2 Leading intraseasonal modes of stratospheric variability

We quantify the intraseasonal variability modes of the stratosphere by two metrics, one for the zonal mean stratospheric circulation, termed as polar vortex index, and the other for the zonally asymmetric circulation, termed as planetary wave index. These two indices are based on empirical orthogonal function (EOF) analysis of Z10 that is area-weighted by the square root of the cosine of the latitudes (results are not sensitive to the chosen pressure level). The polar vortex index is equivalent to the Northern Annular Mode (NAM) index (Baldwin & Thompson, 2009; Gerber et al., 2010), defined as the standardized principal component of the first EOF of zonally averaged intraseasonal Z10 north of 20°N. The planetary wave index is defined as the standardized principal component of the first EOF of the zonally asymmetric

Z10 north of 20°N. Note that the leading EOFs of zonally symmetric and asymmetric Z10 are not necessarily the same as the first two EOFs of the total Z10 field.

The phases of the wave index may be related to events of extreme positive or negative eddy heat fluxes (e.g., Shaw et al., 2014). Figure 2.A.1 shows the joint probability density distribution between the 50°–70°N wave-1 eddy heat flux at 100 hPa and the wave index at 10 hPa. Since the positive heat flux represents an enhancement in upward propagation of planetary waves at 100 hPa, the positive phase of the wave index may be comparable to extreme positive heat flux events. But we also note that negative values of the wave index correspond to eddy heat flux values of both positive and negative signs. More importantly, we use lagged regression to characterize the lead-lag relationship rather than composite analysis (i.e., regressing atmospheric variables onto the two stratospheric indices with positive and negative lags). For example, the regression coefficients of the inverted polar vortex index for day 0 roughly correspond to the composite for negative one standard deviation of the vortex index (i.e., a weak vortex based on negative values of NAM). Day 5/-5 indicates that the stratospheric index leads/lags the other variables by 5 days. A detailed description of the lagged regression analysis can be found in Text 2.A.1.

Figure 2.5.1a and b display the regressed spatial patterns of the intraseasonal variability modes of the stratosphere in the ERA-Interim reanalysis. The negative phase of the polar vortex index (Figure 2.5.1a) is nearly zonally symmetric, characterized by a high anomaly in the polar region that superposes onto the climatological low center. Thus, the negative/positive phase of the vortex index represents the weakening/strengthening of the stratospheric polar vortex. In contrast, the positive phase of the planetary wave index (Figure 2.5.1b) is primarily a planetary wave-1 pattern or a displacement of the polar vortex,

composed of a high anomaly over northern North America and a low anomaly over northern Eurasia. Compared with the climatological wave pattern, the positive/negative phase of the wave index largely describes the intensification/weakening of the planetary wave-1, due to constructive/destructive interference with the climatological wave-1 (K. L. Smith & Kushner, 2012). Note that we have used effective degrees of freedom for all the regression analyses to account for the autocorrelation in the time series, which would otherwise cause substantial biases in estimating statistical significance (Bretherton et al., 1999).

We also characterize the surface variability by the AO and an SAT mode over North America (Figure 2.5.1c, d). The AO is defined as the first EOF of zonally averaged intraseasonal SLP north of 20°N. The SAT mode is defined as the first EOF of intraseasonal SAT over the North American sector (20°–90°N, 0°–180°W). The surface regressions to the inverted AO index (Figure 2.5.1c) describe the well-known negative AO pattern: high pressure over the Arctic and low pressure over the North Atlantic and North Pacific, with two cooling centers over North America and Eurasia, and two small regions of warming over Greenland and eastern Siberia (Thompson & Wallace, 1998). We can also interpret the warming over eastern Canada and cooling over Eurasia as the signature of NAO, which can be seen as a regional counterpart of the AO. Meanwhile, the positive phase of the North American SAT mode (Figure 2.5.1d) consists of a strong cooling center over North America, a warming center over Bering Strait, and a high pressure center over Alaska (e.g., W. Guan et al., 2020; Tan & Bao, 2020).

2.3 Results

We begin by comparing the evolution of SAT and SLP with respect to the two stratospheric indices in ERA-Interim. Figure 2.5.2 compares the lagged regression patterns of surface

conditions over a 15-day period. The lagged regressions for the inverted polar vortex index are largely similar through day 0–10 (Figure 2.5.2b–d): the SLP anomaly displays an annular structure between the midlatitudes and Arctic; the SAT anomaly shows cooling over Northern Eurasia and midlatitude North America and warming over eastern Canada and midlatitude Asia. Both anomalies bear resemblance to the negative phase of AO (Figure 2.5.1c). Thus, this may be described as zonally symmetric surface signatures following the zonally symmetric variability mode in the stratosphere, as SSWs (e.g., Baldwin & Dunkerton, 2001).

By comparison, the lagged regressions for the planetary wave index show transitions from a pattern of North American warming and Alaska cooling at day -5 to the opposite condition at day 10 (Figure 2.5.2e–h). The SAT pattern over North America at day -5 (Figure 2.5.2e) resembles the negative phase of North American SAT mode. The strong North American warming is associated with the northward temperature advection favored by the deepened Aleutian Low. The temporal evolution during day -5–10 could be thought of as a negative-to-positive transition of the SAT mode (Figure 2.5.1d, also see W. Guan et al., 2020). While the SLP anomaly is consistent with the SAT pattern over North America, it is better described as a planetary wave-1 pattern at day 10, which projects onto positive NAO, with North American cooling and Eurasian warming.

We have also examined the lagged regressions of geopotential height at 500 hPa (denoted as Z500 hereafter) over the same period, which exhibit a zonally symmetric structure following the weak polar vortex in comparison with a planetary wave-1 pattern associated with the wave index (Figure 2.A.2), like the comparison made with SAT and SLP between the two stratospheric indices. Additionally, we have performed regression analysis for the JRA-55

reanalysis spanning over a longer period of 1958–2020 (Figure 2.A.3). The JRA-55 results are quantitatively similar to Figure 2.5.2, supporting the distinct surface signatures following the two stratospheric modes of variability in ERA-Interim.

To further illustrate the temporal evolutions in the stratosphere and on the surface, we plot the lagged regressions with the vortex and wave indices over a 60-day period (Figure 2.5.3). Besides the two reanalyses, we include results from the PAMIP and AMIP simulations. Figure 2.5.3a presents the Z10 over the polar cap (north of 60°N) regressed onto the inverted vortex index, confirming that the negative phase of vortex index describes a weak polar vortex state. The regression to the wave index in Figure 2.5.3b, in contrast, indicates a transition from a stronger-than-normal polar vortex to a weaker-than-normal state from day -10 to day 10. The stronger-than-normal polar vortex at negative lags may be related to the stratospheric preconditioning for upward wave activity (e.g., McIntyre, 1982).

The lagged regressions of AO onto stratospheric indices reveal distinct temporal evolutions in SLP (Figure 2.5.3c, d). The regression to the inverted vortex index (Figure 2.5.3c) suggests that a weak polar vortex precedes persistent negative AO after day 0, consistent with Figure 2.5.2b–d and the well-known downward influence of SSWs (e.g., Baldwin & Dunkerton, 2001). By contrast, the AO regressed onto the wave index is positive during day -10–10. But the SLP pattern identified here exhibits more of a wave-1 structure rather than an annular structure (cf. Figure 2.5.2e–h versus Figure 2.5.1c). A similar comparison between the annular and wave-1 patterns is also seen in Z500 (Figure 2.A.2). We have also computed the lagged regressions with NAO in Figure 2.A.4. The results are similar, except that the NAO regression is not positive before day 0 when the center of action in SLP is located over the

North Pacific. Thus, the distinct SLP and Z500 patterns associated with the two stratospheric modes indicate different mechanisms by which the stratosphere impacts the surface.

Figure 2.5.3e and f further compare the regressions of North American SAT index onto the stratospheric indices. The regression with the wave index (Figure 2.5.3f) is characterized by strong negative values around day -5 and positive values around day 10. This indicates surface warming over North America (Figure 2.5.2e) acts as a precursor to the intensification of stratospheric planetary wave-1, which is followed by North American cooling in about 10 days (Figure 2.5.2h). A similar change in sign but with a smaller magnitude is observed in association with the inverted vortex index (Figure 2.5.3e), with negative coefficients around day -10 and positive around day 5. More importantly, there is a large agreement among observations and models for the lagged regressions of the SAT index onto the wave index. These regression coefficients are statistically significant for both the positive and negative peaks in nearly all the model and reanalysis data examined here, indicating a robust time-lagged relationship between the stratospheric wave activity and North American SAT mode. While previous studies have reported connections between anomalous stratospheric wave activity and North American cooling (e.g., Kretschmer et al., 2018; Tan & Bao, 2020), our results highlight that strong stratospheric wave activity is associated with a surface transition from North American warming at day -5 to cooling at day 10, with important implications for the intraseasonal predictability of surface temperature in the northern U.S. and Canada.

Figure 2.A.5 presents the surface patterns with respect to the vortex and wave indices in models, in accordance with the timing of the largest positive regression coefficients between them and the SAT index in Figure 2.5.3e, f. The regressions with the inverted vortex index

at day 5 display a negative AO-like pattern in SAT and SLP in all four models as in observations, although CAM6-AMIP underestimates the positive SLP anomaly near Greenland (cf. Figure 2.5.2c and Figure 2.A.5a–d). The SAT patterns regressed onto the wave index at day 10 show a consistent wave-1 structure, with North American cooling and Eurasian warming (cf. Figure 2.5.2h and Figure 2.A.5e–h). This can be attributed to the projection of a planetary wave-1 pattern onto positive NAO, but the cooling extends more westwards beyond the east coast that NAO typically influences. The general agreement among model simulations supports the surface signatures of stratospheric variability identified in reanalyses. Remarkably, the North American cooling following strong stratospheric wave activity is more pronounced and robust than that following a weak polar vortex, consistent with the lagged regressions in Figure 2.5.3e, f. This indicates that strong stratospheric wave activity is a better precursor for cold spells over North America than a weak polar vortex.

Finally, we turn to the vertical structure of the linkage between the stratosphere and surface in ERA-Interim. Figure 2.5.4a, b show the zonal wind (averaged over 50°–70°N) regressed onto the two stratospheric indices, both of which display a downward propagation of zonal wind anomalies, as typically found following SSWs (e.g., Baldwin and Dunkerton, 2001). However, the regression to the inverted vortex index indicates a zonal wind minimum at day 0 at 10 hPa, followed by persistent negative zonal wind anomalies in the troposphere, whereas the regression to the wave index corresponds to a strong zonal wind deceleration around day 0, with positive zonal wind anomalies in the troposphere. These results agree with the sign of the regressed AO in Figure 2.5.3c, d, and the positive stratospheric wind anomalies at negative lags are consistent with the strong polar vortex state in Figure 2.5.3b.

We further examine the variability in wave-1 amplitude difference due to wave interference, which is described in detail in Text 2.A.2. The anomalous wave-1 meridional heat flux and the wave-1 amplitude difference due to wave interference (averaged over 50°–70°N) regressed to the inverted vortex index (Figure 2.5.4c, e) are, by and large, positive before day 0 and negative after day 0, consistent with the sign of zonal wind anomaly tendency. However, the regressions to the wave index (Figure 2.5.4d, f) indicate an enlarged amplitude of planetary wave-1 in the stratosphere during day -10–10. The enhancement in stratospheric wave-1 heat flux is associated with the change in the sign of anomalous heat flux at 500 hPa from upward before day 0 to downward after day 0 (Figure 2.5.4d). This vertical structure is similar to that of positive heat flux events (e.g., Dunn-Sigouin & Shaw, 2015). The upward/downward heat flux anomalies also correspond to the constructive/destructive interference between the anomalous and stationary wave-1 patterns (Figure 2.5.4f). These changes in wave-1 are consistent with the shift from North American warming to cooling, implying a planetary wave mechanism rather than the downward propagation of annular modes. Additional analysis (Figure 2.A.6) shows that the wave-2 component of meridional heat flux plays a relatively minor role compared with wave-1 for both indices of stratospheric variability.

2.4 Conclusions

In this paper, we have compared the surface signatures of two leading intraseasonal modes of stratospheric variability, one on the zonal mean circulation, and the other on the zonally asymmetric circulation, which measure the strength of the polar vortex and a planetary wave-1 pattern, respectively. The surface pattern following a weak polar vortex displays negative AO–like anomalies, with cooling over northern Eurasia and midlatitude North America and warming over eastern Canada and midlatitude Asia, as SSWs (e.g., Baldwin

and Dunkerton, 2001). In contrast, strong stratospheric wave activity is associated with a planetary wave-1 structure extending from the stratosphere to the troposphere, which is qualitatively similar to that of stratospheric positive heat flux events (e.g., Dunn-Sigouin & Shaw, 2015). Our lagged regression analysis further shows that the associated surface pattern projects onto the positive phase of NAO, with North American cooling and Eurasian warming in about 10 days. We highlight distinct surface temperature patterns over North America, whereas most previous studies focused on circulation patterns. Our results suggest that the zonally symmetric and asymmetric components of stratospheric variability impact the surface through the annular and planetary wave-1 patterns, respectively. Furthermore, a North American warming pattern precedes the positive phase of the wave index by about 5 days (Figure 2.5.3f). The anomalously warm weather in winter could have important societal implications such as energy prices, but strong stratospheric wave activity does not provide predictive skills because the warm temperature precedes stratospheric variability. In contrast, the anomalous warming pattern transitions to North American cooling with a 10-day lag following the strong stratospheric wave activity (Figure 2.5.3f), which offers a source of predictability for cold spells over North America. Note that it is hard to identify this lead-lag relationship with the composite mean over the entire life cycle of few extreme events as the cooling signal is much weaker than the preceding warming.

The robustness of the linkage between the stratospheric and surface variability is examined in two reanalysis products and four models with different configurations. There is a broader region of statistically significant cooling over North America following strong stratospheric wave activity than following a weak polar vortex. This may be attributed to the structure of planetary wave-1 following strong stratospheric wave activity (Figure 2.A.2e–h, Figure 2.5.4d, f), which likely leads to the intensification of Alaska blocking and the deepening of the North

American trough that favor the cold spells over North America. Thus, strong stratospheric wave activity is regarded as a better predictor for North American cooling than a weak polar vortex.

Acknowledgments. We thank two anonymous reviewers for constructive comments on the manuscript. Xiuyuan Ding and Gang Chen are supported by NSF Grant AGS-1832842 and NASA Grant 80NSSC21K1522. We would like to acknowledge high performance computing support from Cheyenne (https://doi.org/10.5065/D6RX99HX) provided by NCAR's Computational and Information Systems Laboratory, sponsored by the National Science Foundation.

2.5 Figures

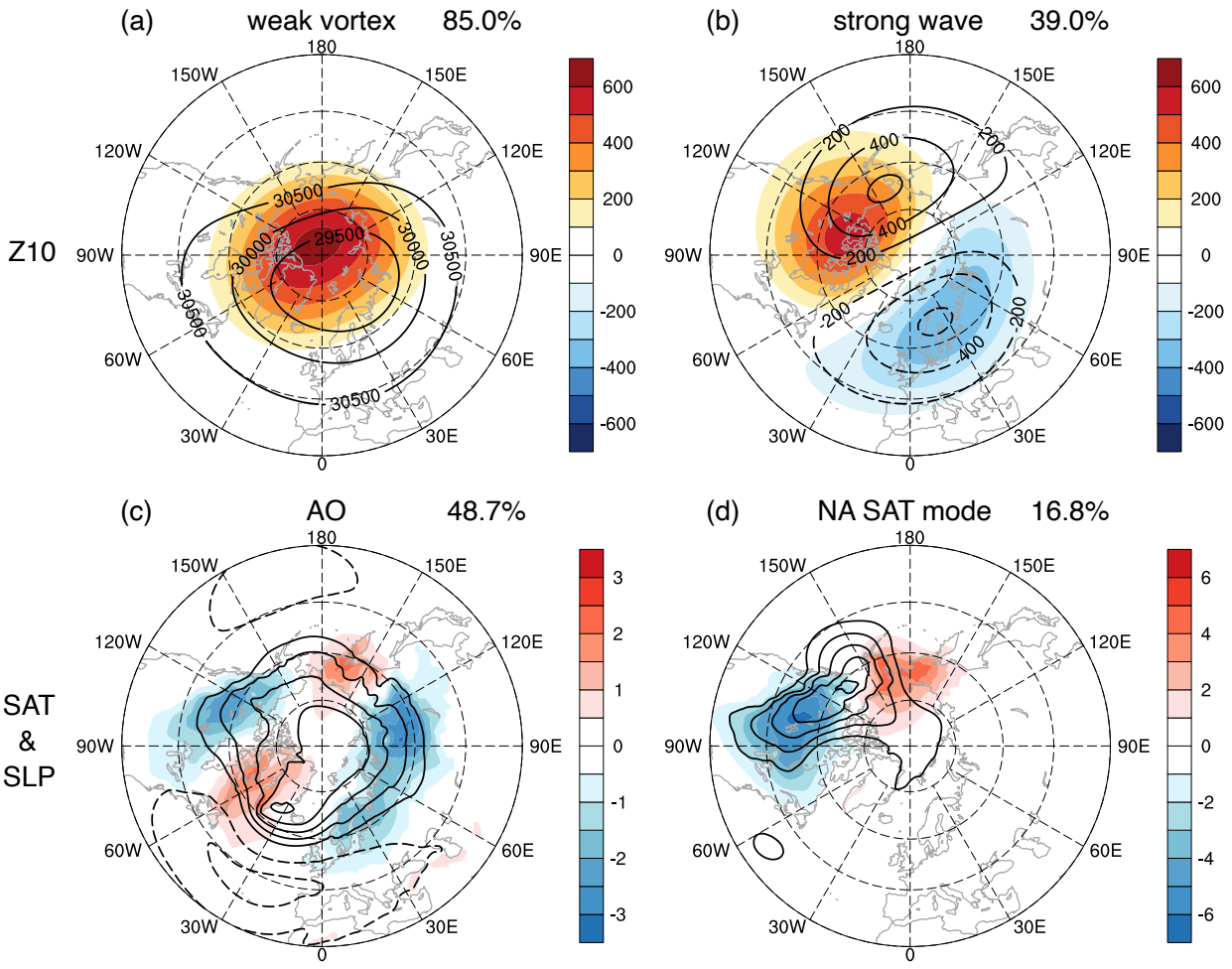

Figure 2.5.1: The leading intraseasonal variability modes of the stratosphere and surface conditions in extended boreal winter (November–March) in ERA-Interim. (a, b) Regression patterns (shading) of Z10 (m), to (a) the inverted polar vortex index and (b) planetary wave index, respectively. The two indices are defined by the first EOF of zonally symmetric and asymmetric components of Z10, respectively. The black contours indicate the climatology of Z10 [contour intervals (CI): 500m] in (a) and its wave-1 component (CI: 200m) in (b). (c, d) Regression patterns (shading) of SAT (K) to (c) the inverted AO index and (d) North American SAT mode, respectively. The AO is defined by the first EOF of zonal mean SLP, and the North American SAT mode is defined by the first EOF of the SAT over the North American sector. Note different colorbars are used in (c, d). The black contours in (c, d) indicate the corresponding SLP regression patterns (CI: 1.5hPa). The fraction of variance explained by each EOF is displayed in the upper right corner of each panel.

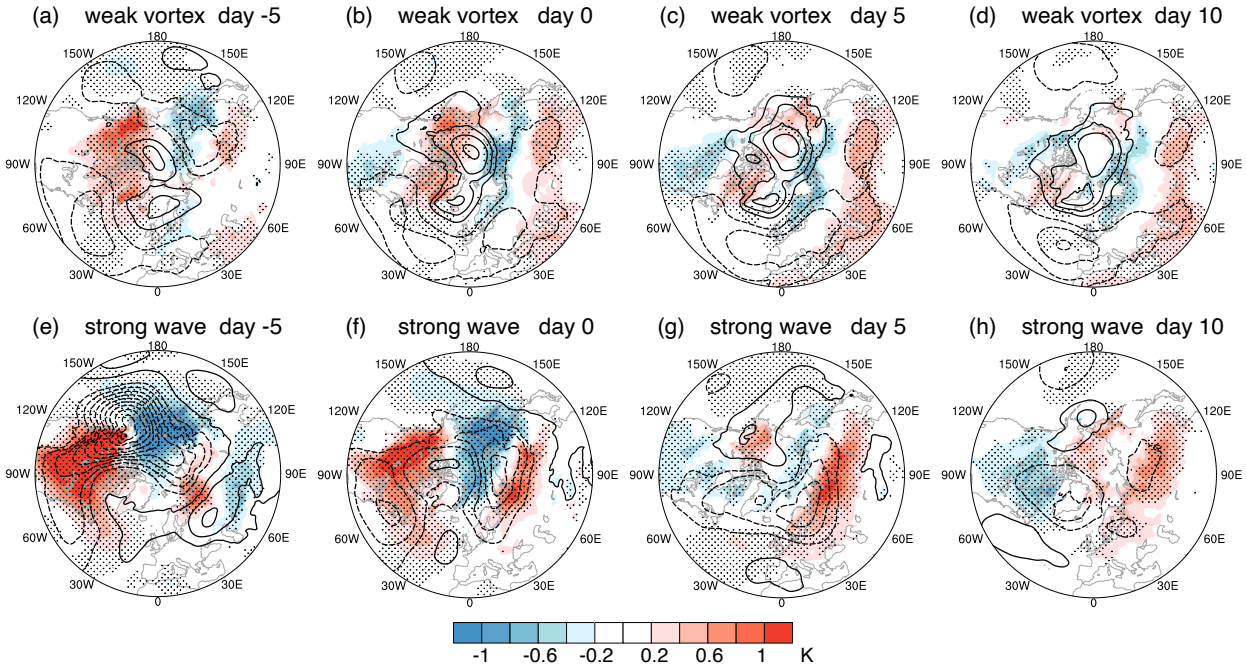

Figure 2.5.2: Lagged regression patterns of SAT and SLP onto (top) the inverted vortex index and (bottom) wave index: (a, e) day -5, (b, f) day 0, (c, g) day 5, and (d, h) day 10. Shading denotes SAT, and contours denote SLP (CI: 0.5hPa). Positive lags indicate that the stratospheric variability precedes the surface variability. Stippling represents the SAT regression significant at the 95% confidence level based on the student's *t*-test. See the results for JRA-55 in Figure 2.A.3.

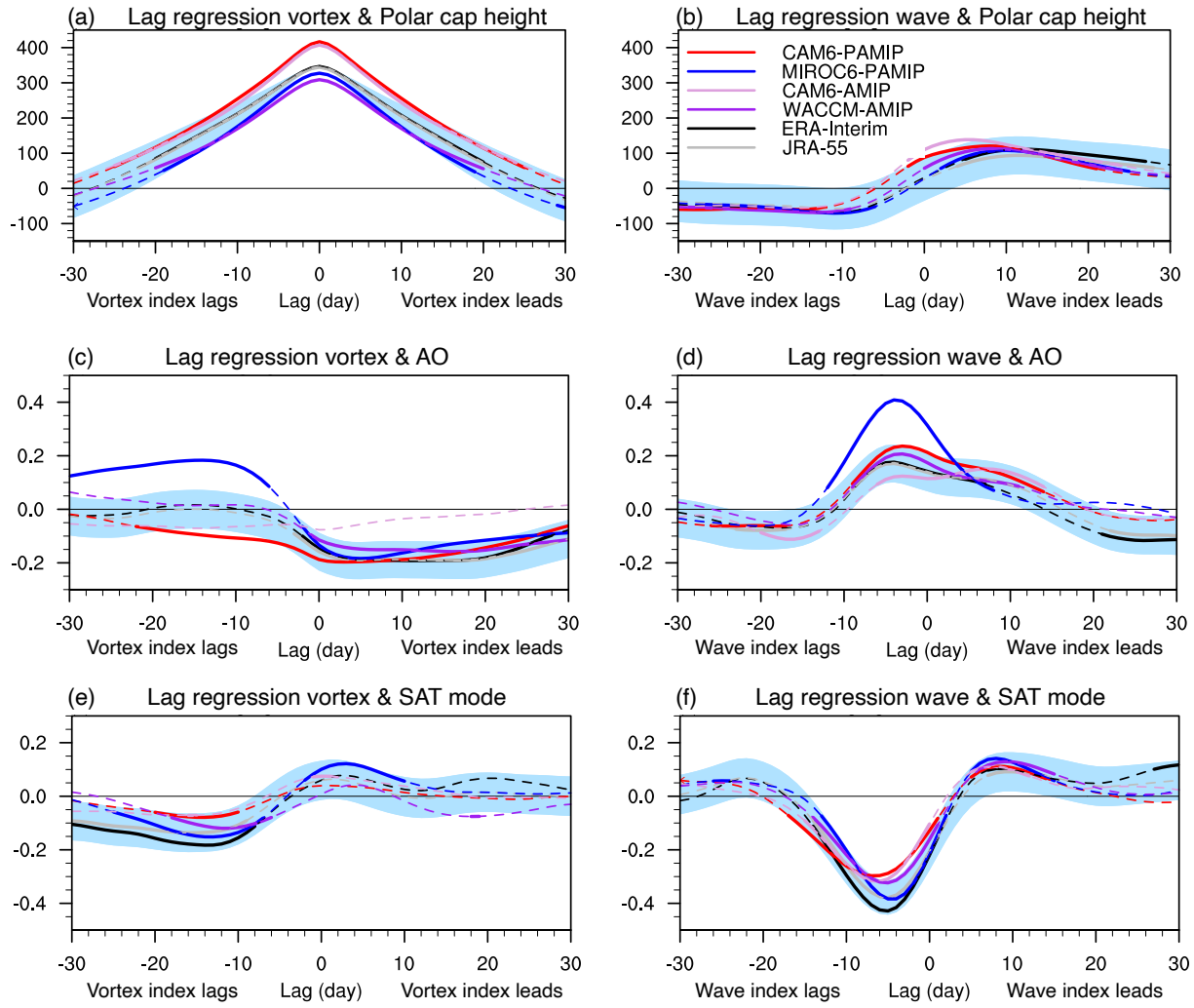

Figure 2.5.3: Lagged regressions with respect to (left) the inverted vortex index and (right) wave index in two reanalyses and four models. (a, b) Z10 averaged over the polar cap (north of 60°N; meter), (c, d) AO index, and (e, f) North American SAT index. Positive lags indicate that the stratospheric indices lead the other variables. Positive values of the North American SAT index indicate cooling over North America (Figure 2.5.1d). The lines in red, blue, plum, purple, black and grey represent CAM6-PAMIP, MIROC6-PAMIP, CAM6-AMIP, WACCM-AMIP, ERA-Interim and JRA-55, respectively. Solid parts of the lines represent regression coefficients significant at the 95% confidence level based on the student's *t*-test. The light blue shading denotes the 2.5–97.5% confidence interval estimated using JRA-55 data.

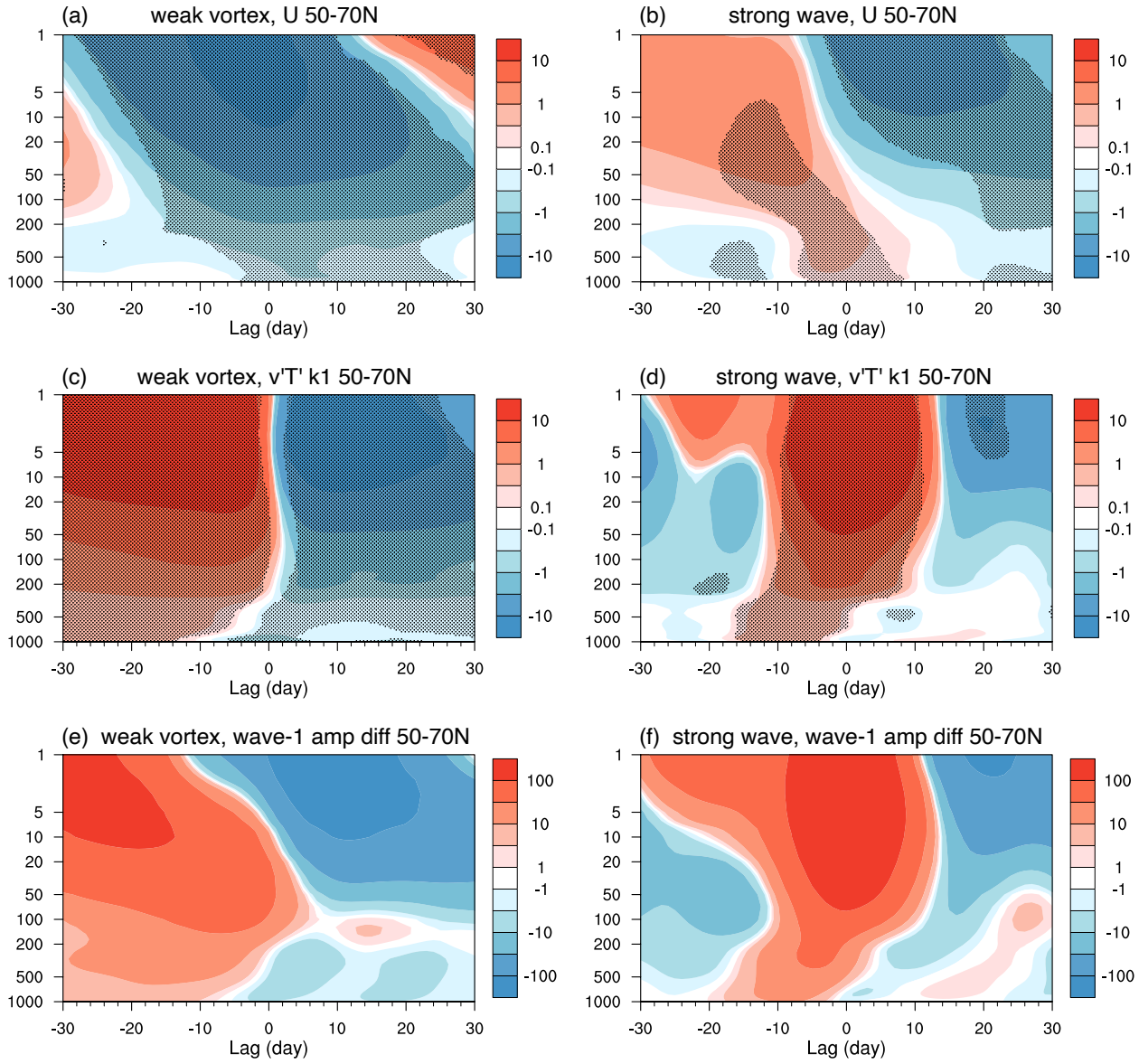

Figure 2.5.4: Lagged regressions in ERA-Interim as a function of pressure with respect to (left) the inverted vortex index and (right) wave index, respectively. Zonally averaged (50°–70°N) (a, b) zonal wind (m/s), (c, d) wave-1 meridional heat flux (K*m/s), and (e, f) wave-1 amplitude difference due to wave interference (m). Positive lags indicate that the stratospheric indices lead the other variables. The wave-1 amplitude difference due to wave interference is calculated from the amplitude of the total (stationary + anomalous) wave-1 pattern subtracted by that of the stationary wave-1 pattern, described in detail in Supporting Information. Positive/negative values indicate the anomalous wave-1 pattern is constructive/destructive to the stationary wave-1. Note the colorbar scale is logarithmic. Stippling in (a–d) represents the regression significant at the 95% confidence level based on the student's *t*-test.

2.A Appendices

Text 2.A.1: In the text, we performed regression analysis between the stratospheric indices and the surface fields for a range of time lags between the predictor and predictand. Taking the shading in Figure 2.5.2a–d for example, at the time lag of Δt days, the two variables used for lagged regressions are the inverted polar vortex index (t) and anomaly of SAT $(x, t + \Delta t)$. The corresponding linear model can be expressed as

$$SAT(x, t + \Delta t) = \beta(x) \times inverted\ polar\ vortex(t),$$

where $\beta(x)$ is the regression coefficient. Day $\Delta t > 0$ ($\Delta t < 0$) indicates that the stratospheric index leads (lags) the surface variable by $|\Delta t|$ days. As such, day 5 means that the inverted stratospheric polar vortex index leads the surface variables by 5 days. Similarly, day 0 represents the instantaneous regressions between the inverted polar vortex index and other variables, and this roughly corresponds to the composite for negative one standard deviation of the vortex index (i.e., a weak vortex).

Text 2.A.2: To calculate wave interference, we first compute the amplitude of the total (climatological + anomalous fields) wave-1 pattern. Then the amplitude of the stationary wave-1 is calculated from the climatology and subtracted from the amplitude of the total wave-1, with the remaining part being the wave-1 amplitude difference shown in Figure 2.5.4e, f. For constructive wave interference, the remaining part will be positive by definition, because the total wave-1 pattern has a larger wave amplitude than the stationary wave due to the amplification by the anomalous wave-1. Conversely, the remaining part will be negative for destructive wave interference, because the total wave-1 has a smaller wave amplitude than the stationary wave. We also note that the total wave amplitude of the superposition of stationary and anomalous planetary waves is not linearly additive because it is also affected by the phases of two waves. Thus, the wave-1 amplitude difference in our calculation is not equal to the amplitude of the anomalous planetary wave.

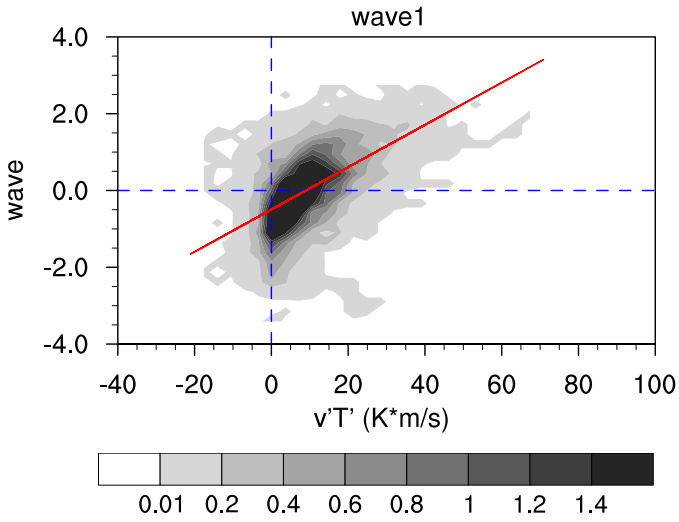

Figure 2.A.1: Joint probability density distribution (unit: %) between the planetary wave-1 eddy heat flux at 100 hPa (50°–70°N averaged) and the planetary wave index at 10 hPa.

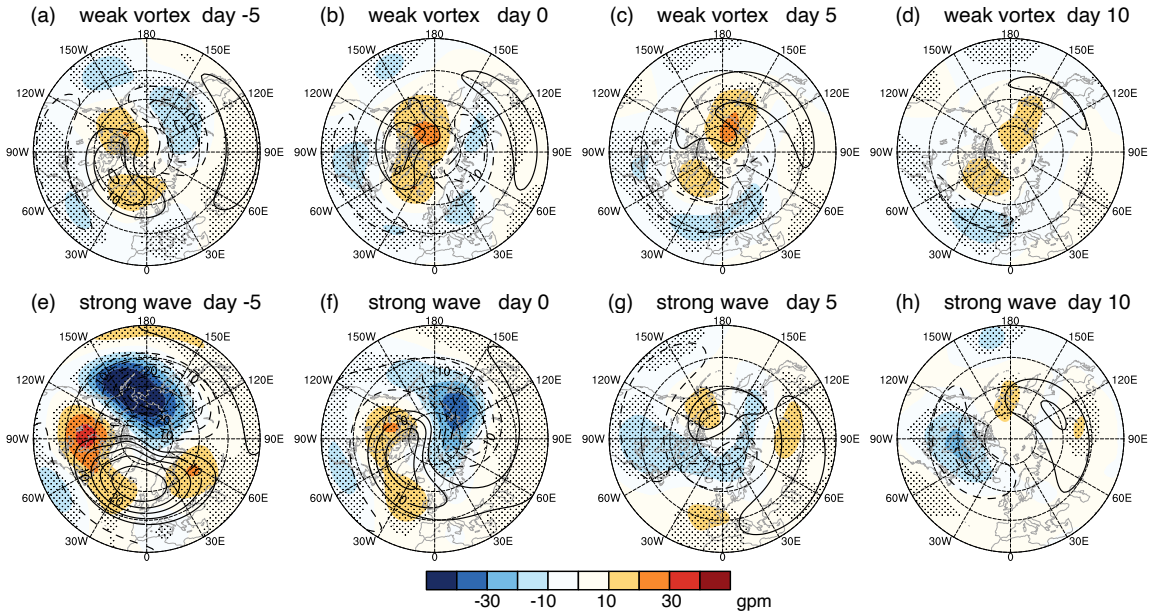

Figure 2.A.2: As in Figure 2.5.2, but for Z500 and its wave-1 component regressed onto (top) the inverted vortex index and (bottom) wave index in ERA-Interim, respectively. (a, e) day -5, (b, f) day 0, (c, g) day 5, and (d, h) day 10. Shading denotes Z500, and contours denote the wave-1 component of Z500 (CI: 5m). Stippling represents the Z500 regression significant at the 95% confidence level based on the student's *t*-test.

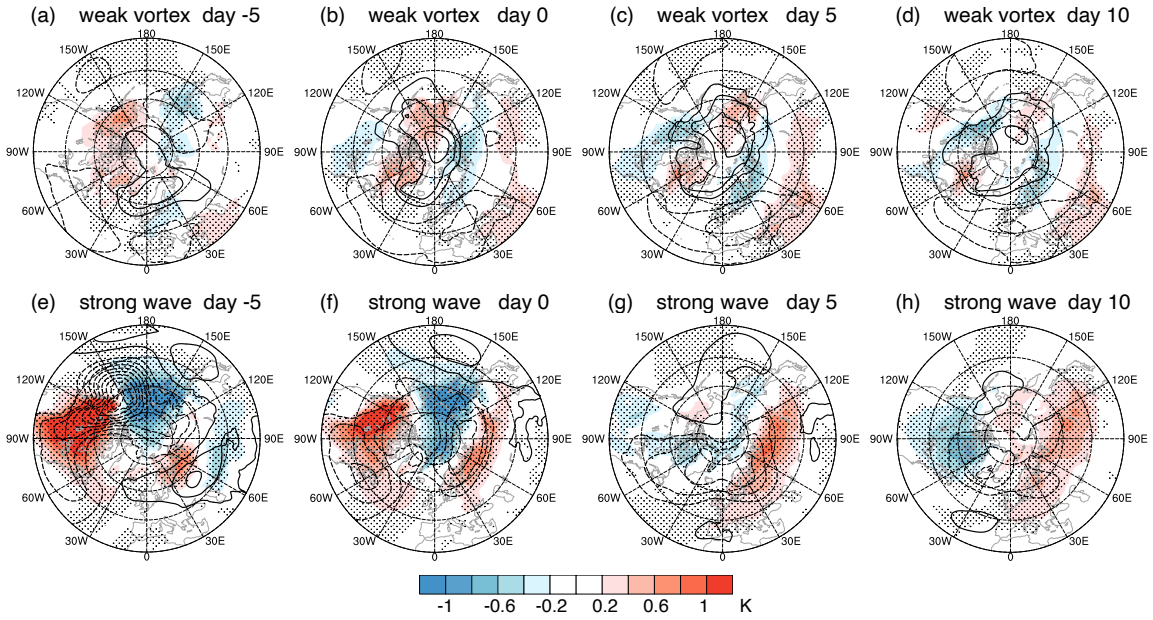

Figure 2.A.3: As in Figure 2.5.2, but for SAT and SLP (CI: 0.5 hPa) in the JRA-55 reanalysis over a longer period of 1958–2020.

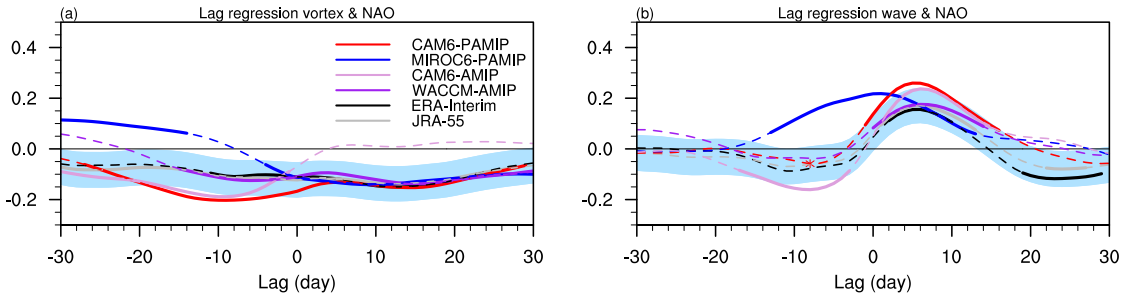

Figure 2.A.4: Lagged regressions of NAO with respect to (a) the inverted vortex index and (b) wave index in two reanalyses and four models. NAO is calculated as the standardized area-weighted SLP difference between the regions of 55°–90°N, 90°W–60°E and 20°–55°N, 90°W–60°E. Positive lags indicate that the stratospheric variability leads NAO. The lines in red, blue, plum, purple, black and grey represent CAM6-PAMIP, MIROC6-PAMIP, CAM6-AMIP, WACCM-AMIP, ERA-Interim and JRA-55, respectively. Solid parts of the lines represent regression coefficients significant at the 95% confidence level based on the student's *t*-test. The light blue shading denotes the 2.5–97.5% confidence interval estimated using JRA-55 data.

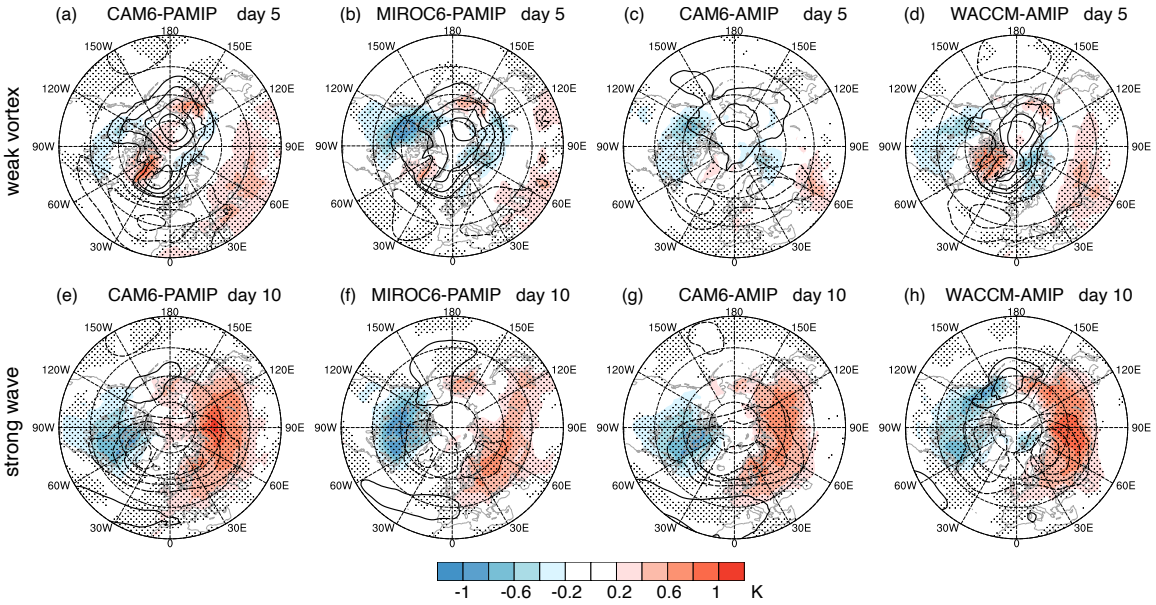

Figure 2.A.5: As in Figure 2.5.2d and h, but for the lagged regressions in four model simulations. (a, e) CAM6-PAMIP, (b, f) MIROC6-PAMIP, (c, g) CAM6-AMIP, and (d, h) WACCM-AMIP. The regressions are shown for day 5 with respect to the inverted vortex index and for day 10 with the wave index, in accordance with the timing of the largest regression coefficients between stratospheric indices and North American SAT mode in Figure 2.5.3e and f. Stippling represents the SAT regression significant at the 95% confidence level based on the student's *t*-test.

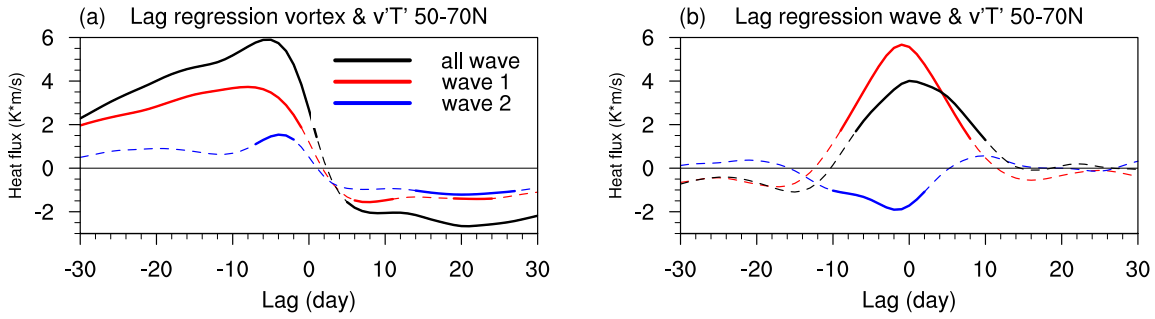

Figure 2.A.6: Lagged regressions of the meridional heat flux at 100 hPa averaged over 50°–70°N with respect to (a) the inverted vortex index and (b) wave index. The meridional heat flux is shown for zonal wave-1, wave-2, and all zonal wavenumbers, respectively. Solid parts of the lines represent regression coefficients significant at the 95% confidence level based on the student's *t*-test.

CHAPTER 3

Extreme Stratospheric Wave Activity as Harbingers of Cold Events over North America

[**Ding, X.**, Chen, G., Zhang, P., Domeisen, D. I. V., & Orbe, C. (2023). Extreme stratospheric wave activity as harbingers of cold events over North America. *Communications Earth & Environment*, *4*(1), 187.]

Abstract

Extreme cold events over North America such as the February 2021 cold wave have been suggested to be linked to stratospheric polar vortex stretching. However, it is not resolved how robustly and on which timescales the stratosphere contributes to the surface anomalies. Here we introduce a simple measure of stratospheric wave activity for reanalyses and model outputs. In contrast to the well-known surface influences of sudden stratospheric warmings (SSWs) that increase the intraseasonal persistence of weather regimes, we show that extreme stratospheric wave events are accompanied by intraseasonal fluctuations between warm and cold spells over North America in observations and climate models. Particularly, strong stratospheric wave events are followed by an increased risk of cold extremes over North America 5–25 days later. Idealized simulations in an atmospheric model with a well-resolved stratosphere corroborate that strong stratospheric wave activity precedes North American cold spells through vertical wave coupling. These findings potentially benefit the predictability of high-impact winter cold extremes over North America.

3.1 Introduction

As global warming is expected to reduce the frequency of severe cold spells, the causes of recent winter cold extremes in the Northern Hemisphere have attracted much public attention and scientific debate (Albers et al., 2022; Bolinger et al., 2022; Cohen et al., 2021; Tyrlis et al., 2019, 2020; R. Zhang et al., 2022). Notably, the exceptional North American cold wave in February 2021 was suggested to be related to the sudden stratospheric warming (SSW) in January 2021 (Lee, 2021; Wright et al., 2021), which was further proposed to be linked to Arctic sea ice loss under global warming (Cohen et al., 2021; R. Zhang et al., 2022). However, numerical weather forecasts for the February 2021 cold wave suggest that the January 2021 SSW event exerted only a limited influence on surface temperature (Albers et al., 2022; Davis et al., 2022; Millin & Furtado, 2022). Given the disproportionate impacts of winter cold extremes on energy and society (Doss-Gollin et al., 2021), an improved understanding of the role of the stratosphere in the predictability of surface cold spells is warranted.

There exist different types of stratospheric impacts on surface air temperature (SAT). SSWs feature an abrupt deceleration and reversal of the zonal wind in the winter stratosphere primarily due to planetary wave breaking and wave absorption, which is followed by downward propagation of negative zonal wind anomalies to the lower stratosphere on weekly to monthly timescales (Afargan-Gerstman & Domeisen, 2020; Baldwin & Dunkerton, 2001; Butler et al., 2017; Domeisen, Butler, et al., 2020b; Garfinkel et al., 2017; Hitchcock & Simpson, 2014; Karpechko et al., 2017; Polvani & Waugh, 2004; Sigmond et al., 2013). The surface composite of SSWs is characterized by an anomalous high pressure center near Greenland, with anomalous cooling over northern Eurasia and warming over eastern Canada

that resemble the negative phase of the Arctic Oscillation (AO). In contrast, extreme stratospheric wave events, featuring negative meridional eddy heat flux due to planetary wave reflection, are instantaneously linked to the positive phase of the North Atlantic Oscillation (NAO) and anomalous North American cooling (Dunn-Sigouin & Shaw, 2015; Shaw et al., 2014; Shaw & Perlwitz, 2013).

These two types of stratospheric impacts on the surface can be distinguished by the sign of lower-stratospheric meridional heat flux during the recovery stage of SSWs (Kodera et al., 2013, 2016), clustering analysis (Cohen et al., 2021; Kretschmer et al., 2018; Lee et al., 2019; Liang et al., 2022), or empirical orthogonal function (EOF) analysis (Ding et al., 2022; Shen et al., 2022). Particularly, Cohen et al. (2021) argues that stratospheric polar vortex stretching involving planetary wave reflection is linked to North American cold spells such as the February 2021 Texas cold wave. However, the Alaskan ridge weather regime associated with widespread severe North American cold does not show a dependency on stratospheric vortex strength (Lee et al., 2019). Stratospheric wave reflection events are further associated with an evolution from a Pacific trough regime with surface warm anomalies over North America to an Alaskan ridge regime that favors North American cold (Messori et al., 2022). In contrast to circulation regimes, the relevant stratosphere-troposphere coupling can be characterized as an intraseasonal variability mode (Shen et al., 2022). As the wave reflection events in these studies are often based on the lower-stratospheric (i.e., 100. hPa) circulation patterns that may be strongly related to tropospheric variability, the contribution of stratospheric variability to North American cold snaps remains unclear.

Identifying the surface signals of stratospheric variability is also hindered by large internal variability in both the stratosphere and troposphere. Distinct surface signals are found to follow different types of SSW events, such as the displacement of a polar vortex off the pole versus the split of a polar vortex into two smaller vortices (Charlton et al., 2007; Mitchell et al., 2013). Strong tropospheric weather variability can obscure the predictability from the downward propagation of signals, with only about two-thirds of SSWs being followed by visible downward influences featured by negative AO (Afargan-Gerstman et al., 2022; Charlton-Perez et al., 2018; Domeisen, Grams, et al., 2020). Using large ensembles from a climate model that differ only by small changes to the initial conditions, previous studies have found that even a 100-member ensemble may be insufficient to detect the surface influences of stratospheric variability under climate change, due to the large internal atmospheric variability (Peings et al., 2021; Sun et al., 2022). A previous study finds that the February 2021 North American cold event was largely affected by unpredictable internal atmospheric variability (Albers et al., 2022). We will thus use both observations and climate model ensembles to evaluate the robustness and mechanisms of the contributions of extreme stratospheric events to surface temperature anomalies.

In this study, we will first present the surface fingerprints of extreme stratospheric wave activity in observations and the historical simulations from 30 climate models from the Coupled Model Intercomparison Project Phase 6 (CMIP6), showing that strong stratospheric wave events are consistently followed by North American cold anomalies 5–25 days later. This indicates that strong stratospheric wave activity can serve as a sub-seasonal predictor for cold air outbreaks over North America. In contrast to the persistent weather regimes associated with stratospheric polar vortex events (Baldwin & Dunkerton, 2001; Butler et al., 2017; Domeisen, Butler, et al., 2020b; Garfinkel et al., 2017; Hitchcock & Simpson, 2014;

Karpechko et al., 2017; Polvani & Waugh, 2004; Sigmond et al., 2013) or lower-stratospheric wave reflection events (Cohen et al., 2021; Kretschmer et al., 2018), we substantiate an emerging linkage between extreme stratospheric wave events and the intraseasonal fluctuations between warm and cold snaps over North America (Ding et al., 2022; Messori et al., 2022; Shen et al., 2022). We further support this linkage through idealized nudging simulations in the Specified Chemistry Whole Atmosphere Community Climate Model (SC-WACCM4) (K. L. Smith et al., 2014), which suggests that the vertical wave coupling plays a key role in the North American cold extremes following strong stratospheric wave events.

3.2 Methods

3.2.1 Reanalysis data and CMIP6 models

We use atmospheric and surface data from the fifth generation of atmospheric reanalysis from the European Centre for Medium-Range Weather Forecasts (ERA5) (Hersbach et al., 2020). The daily data at a resolution of 1.5◦ ×1.5◦ is analyzed for the extended boreal winter from November to March over the period 1950–2021. After detrending, we remove the seasonal cycle in the data, which is defined as the time mean and first two harmonics of the full-year climatology.

We also employ historical simulations of 30 CMIP6 models. The daily data are examined for the period of 1950–2014 (except for GISS-E2-2-G in 1970–2014 due to limited data availability). All model data are bilinearly interpolated to a common 1.5◦×1.5◦ grid. Only a single member of each model ensemble is analyzed here. See the list of CMIP6 models, the ensemble members used, and vertical resolution in Table 3.A.1.

3.2.2 Definition and statistics of extreme stratospheric wave events

We use a planetary wave index that is simple and readily applicable to reanalyses and climate model outputs. Extreme stratospheric wave events are defined based on empirical orthogonal function (EOF) analysis of the geopotential height at 10 hPa, for ERA5 reanalysis and each CMIP6 model individually (Figure 3.A.1). The planetary wave index is obtained as the standardized principal component of the first EOF of the zonally asymmetric 10-hPa geopotential height north of 20◦N, weighted by the square root of the cosine of latitude.

For both the reanalysis and models, a weak stratospheric wave event is detected as the consecutive days when the planetary wave index is below the 5th percentile, and a strong wave event corresponds to the consecutive days when the index is above the 95th percentile. No minimum duration is required for an event. The first day satisfying the threshold criterion is referred to as day 0 of the event, day -5 denotes 5 days before day 0, and day 5 denotes 5 days after day 0. This results in 89 weak wave events and 93 strong events out of 71 winters in ERA5, at the frequency of 1.25 weak and 1.31 strong events per year. The CMIP6 model ensemble produces an average frequency of 1.29±0.16 weak and 1.32±0.21 strong events per year. The uncertainty is estimated by the SD across the CMIP6 models. Moreover, in the SC-WACCM4 simulations described below, 56 weak and 64 strong wave events are detected out of 49 winters, at the frequency of 1.14 weak and 1.31 strong events per year. This indicates that the frequency of extreme stratospheric wave events is consistent among reanalysis and models, and hence the models represent a valid tool for studying these events.

3.2.3 SC-WACCM4 and nudging experiments

SC-WACCM4 is the stratosphere-resolving atmospheric component of the National Center for Atmospheric Research (NCAR) Community Earth System Model version 1.2 (CESM1), with specified chemistry to reduce the computational cost without changing the climatology and variability of the atmospheric circulation in the troposphere and stratosphere (K. L. Smith et al., 2014). SC-WACCM4 has 66 vertical levels and a horizontal resolution of 1.9◦×2.5◦, with a model lid at 5.1×10−6 hPa.

Two SC-WACCM4 experiments, a control run (CTL) and a nudged run (NUDG), are employed to examine the surface signatures of extreme stratospheric wave activity. The two experiments are the same as those from a previous study (P. Zhang et al., 2020). In CTL, the boundary condition of the model is prescribed by the repeating climatological seasonal SST and SIC, which are obtained from the CESM1-WACCM4 historical outputs from the CMIP5 and averaged during 1980–1999 from 7 ensemble members. The nudged run is the same as CTL, but a nudging method was applied. Specifically, the temperature, zonal wind, and meridional wind above 90 hPa were nudged toward those in the CTL with a damping time scale of 6 hours. The fields were fully nudged above 54 hPa, with no nudging applied below 90 hPa and a linearly tapering region in between. The nudging was performed at every time step of the model integration, but the target states from the CTL run were read in every 6 hours, and the model fields were nudged toward the linear interpolation between consecutive target states, which, in this case, were the time-evolving CTL simulation.

By the experimental design, the evolution of the stratospheric circulation is largely the same (but not identical) in NUDG and CTL. Although the surface boundary condition in NUDG is the same for the troposphere as in CTL, the small differences in the stratosphere resulting

from nudging produce distinct trajectories in tropospheric weather from CTL due to the chaotic nature of weather systems. Thus, the tropospheric circulation in NUDG can be regarded as a distinct realization of weather systems, including the downward influence from the stratospheric variability in the CTL run. We note that the nudging technique does not change the winter climatology or standard deviation of SAT over North America. More details of the experimental design and the evaluation of nudging method can be found in a previous study (P. Zhang et al., 2018). Note that instead of nudging only the zonal mean fields (P. Zhang et al., 2018), the full fields were nudged (P. Zhang et al., 2020) in the current study such that the same stratospheric events are found in both CTL and NUDG experiments. The model experiments were integrated for 60 years for both CTL and NUDG, and the last 50 years are analyzed.

3.2.4 Plumb wave activity flux

We use the 3D Plumb wave activity flux to describe zonal, meridional, and vertical wave propagation of quasi-stationary waves (Plumb, 1985).

$$\{F^{\lambda}, F^{\phi}, F^{z}\} = p\cos(\phi)\left\{v'^{2} - \frac{1}{fa\cos(\phi)}\frac{\partial(v'\Phi')}{\partial\lambda}, -u'v' + \frac{1}{fa\cos(\phi)}\frac{\partial(u'\Phi')}{\partial\lambda},\right.$$
$$\left.\frac{f}{\partial\tilde{T}/\partial z + \kappa\tilde{T}/H}\left[v'T' - \frac{1}{fa\cos(\phi)}\frac{\partial(T'\Phi')}{\partial\lambda}\right]\right\}$$

where λ is longitude, ϕ is latitude, z is height, and p is pressure. T is temperature, Φ is geopotential height, u is the zonal wind, and v is the meridional wind. f is the Coriolis parameter and a is Earth's radius. κ is the specific gas constant of dry air divided by the specific heat of dry air. $\tilde{T}$ is the domain-averaged temperature. H is the log-pressure scale height. Primes denote the deviations from zonal means.

The vertical component of the Plumb flux approximately corresponds to the vertical phase tilt of a planetary wave: the upward Plumb flux corresponds to the typical westward phase tilt of a trough or ridge with increasing height, and the downward Plumb flux coincides with an eastward phase tilt with height.

3.3 Results

3.3.1 Surface signatures of extreme stratospheric wave events

We begin by characterizing the surface signatures of extreme stratospheric wave events. Strong and weak wave events are identified by extreme percentiles of the wave index, which is defined as the leading principal component of the zonally asymmetric component of geopotential height at 10 hPa for the extended boreal winter from November to March in ERA5 reanalysis and CMIP6 models (see details in Methods). The corresponding EOF mode of 10 hPa geopotential height features a transient planetary wave-1 pattern, with the positive phase amplifying the climatological wave pattern through constructive wave interference and the negative phase weakening the climatological wave via destructive interference (Ding et al., 2022) (Figure 3.A.1). Consecutive days above the 95th percentile of the wave index are referred to as strong wave events, and the days below the 5th percentile are termed weak wave events. No minimum duration is required for an event. We note that the EOF pattern of transient waves does not fully align with the climatological wave pattern, and a weak wave event may still produce a polar vortex stretching (Figure 3.5.1a). Compared with previous definitions of stratospheric wave events such as eddy heat fluxes (Dunn-Sigouin & Shaw, 2015), cluster analysis (Cohen et al., 2021; Kretschmer et al., 2018; Liang et al., 2022), or temporal filtering (Shen et al., 2022), we believe that the simplicity of this stratospheric wave event definition is appealing, especially in regard to model intercomparison and evaluation.

The consistency among different data sets provides strong support for surface signatures of extreme stratospheric wave events.

The weak wave event composite displays a stretching of the stratospheric polar vortex at 10 hPa towards North America from day -5 to day 0, with an anomalous ridge over Eurasia and a trough over North America (Figure 3.5.1a), resembling the 10-hPa composite of the tropospheric Alaskan ridge weather regime (Lee et al., 2019). The polar vortex in the lower stratosphere (100 hPa) is also stretched, but with an anomalous ridge over Alaska and Eastern Siberia and a trough over North America (Figure 3.5.1b), similar to the circulation pattern observed for polar vortex stretching (Cohen et al., 2021; Kretschmer et al., 2018). Interestingly, while the anomalous upward Plumb wave activity flux over North America and downward flux over Siberia are consistent with the vortex stretching (Figure 3.5.1c), these anomalous fluxes differ from the vertical wave activity fluxes during polar vortex stretching disruptions (Cohen et al., 2021; Kretschmer et al., 2018). Moreover, the anomalous cooling over North America and warming over Alaska and Eastern Siberia occur before and near the event onset (i.e., days -5 and 0) (Figure 3.5.1d). Thus, the surface cooling may contribute to the weak stratospheric wave event rather than being an effect of the stratospheric event (W. Guan et al., 2020; Tan & Bao, 2020). It is also noteworthy that the cold anomalies over northern Eurasia become more extensive from day -5 to day 10.

The strong wave composite, in contrast, exhibits a displacement of the stratospheric polar vortex towards Eurasia at both 10 hPa and 100 hPa (Figure 3.5.2a-b). The overall circulation anomalies of strong wave events are opposite to those of the weak wave events (Figure 3.5.1a-b). Importantly, both the total and anomalous vertical wave activity fluxes are negative over northern North America and persist from the onset day to 10 days later, indicating a local

feature of planetary wave reflection (Figure 3.5.2c). This feature coincides with a transition from anomalous warming over North America before the event onset to cooling 10 days after the onset, as well as the development of a cyclonic anomaly in sea level pressure (SLP) over Greenland 5 to 10 days after the event onset (Figure 3.5.2d). We also observe that warm anomalies over northern Eurasia are amplified and persist from day -5 to day 10. The relatively long timescale of Eurasian warm anomalies indicates that they could be remnants of positive AO, which is a surface response to the anomalously strong polar vortex prior to strong wave events (Figure 3.A.2). On the other hand, weak wave events exhibit much smaller zonal wind anomalies than strong wave events, implying an asymmetry between weak and strong stratospheric wave events.

As the number of extreme stratospheric wave events are limited in observations (1.25 weak and 1.31 strong events per year on average for 1950–2021; see the statistics in Methods), we have also analyzed the historical simulations in 30 CMIP6 models (Figure 3.A.3 and 4). The general characteristics of the extreme wave events in CMIP6 models are strikingly similar to reanalysis in Figure 3.5.1 and 2. These reanalysis and model results consistently indicate that weak stratospheric wave events are associated with North American cooling before and near the polar vortex stretching, and that strong stratospheric wave activity is characterized by a vortex displacement to Eurasia and downward wave activity fluxes over northern North America, followed by North American cooling about 10 days later.

3.3.2 Strong wave events increase the risk of North American cold extremes

We next compare the evolution of SAT anomalies over North America for weak and strong stratospheric wave events in ERA5 and CMIP6 models (Figure 3.5.3a-b), confirming the transitions between warm and cold spells over North America (Figure 3.5.1d and 2d). The

cold SAT anomalies following strong wave events are also consistent with the positive NAO anomalies from day 0 to day 15 (Figure 3.5.3d), which correspond to the cyclonic anomaly in SLP near Green- land and associated cold air advection over North America (Figure 3.5.2d). Since the surface cold anomalies over North America take place 5–25 days after the stratospheric event onset, the strong stratospheric wave events can be used as a sub-seasonal predictor for North American cold extremes. It is then tempting to ask whether extreme stratospheric wave events may be related to the February 2021 Texas cold wave, given its proposed linkage to a stratospheric polar vortex stretching (Cohen et al., 2021). The daily evolutions of the stratospheric wave index and the SAT anomaly for winter 2020/2021 are plotted in Figure 3.5.3e. Following the strong wave activity around January 18, 2021, cold SAT anomalies are observed from late January to mid-February concurrently with weak stratospheric wave activity. While the linkage between individual cold events and stratospheric wave activity should be interpreted with caution, these are largely consistent with the composite analysis in Figure 3.5.3a-b. But given that the cold anomalies in response to stratospheric wave events are mostly north of 40◦N (Figure 3.5.2d), the strong stratospheric wave activity around January 18, 2021, is unlikely a primary contributor to the deep cold in 2021 that reached Texas (30◦N), consistent with previous studies (Albers et al., 2022; Davis et al., 2022).

We will hereafter focus on strong stratospheric wave events, as they are potentially useful for extended-range forecasting of cold events, and their impacts on winter cold extremes are quantified by the risk ratio of extreme cold days. An extreme cold day is defined as a day when the local SAT lies at least 1.5 standard deviations (SD) below its climatology. Figure 3.5.4a shows the risk ratio of extreme cold days for 5–25 days after strong stratospheric wave events. Compared to all the winter days, strong stratospheric wave events enhance the risk

of extreme cold days by about 30% across much of Canada and the Northeast U.S. Moreover, the probability density function (PDF) for the area-averaged SAT anomalies over North America during 5–25 days after strong wave events indicates a general shift towards colder SAT (blue) as compared to the PDF for all the winter days (black) (Figure 3.5.4b). The risk ratios in the ERA5 reanalysis for the exceedance frequency below -1, -1.5, and -2 SD of the PDF are 1.5, 1.8, and 1.9, respectively. These observed characteristics are remarkably similar to the CMIP6 multi-model means, albeit with lower risk ratios in CMIP6 (Figure 3.5.4c-d). Furthermore, we examine the PDF of North American SAT for finer time windows (i.e., day 5–9, day 10–14, day 15–19, and day 20–24) in CMIP6. This confirms similar shifts towards colder SAT over shorter periods, with the largest cold anomalies for day 10-14 (Figure 3.A.5). These results provide consistent observational and modeling evidence that strong stratospheric wave events can increase the frequency of cold snaps over North America.

3.3.3 Strong stratospheric wave events impact the surface via vertical wave coupling

How does strong stratospheric wave activity influence the surface temperature? We first investigate the mechanisms in ERA5, using Plumb wave activity fluxes (See details in Methods) averaged over 50◦–70◦N as a function of longitude and pressure for days -5, 0, 5, and 10 (Figure 3.5.5a). Over Siberia (roughly 90◦–135◦E), Plumb fluxes in the lower stratosphere are predominantly upward and eastward throughout the strong wave events, contributing to the amplification and persistence of an anomalous stratospheric ridge over North America from 5 days before the event onset to 5 days after onset. As the anomalous ridge intensifies, the initial westward tilt of the ridge with increasing altitude on day -5 transitions to a nearly barotropic structure starting at the event onset. After the event onset, the eastern edge of the anomalous ridge (or the trough from 90◦W to 0◦) displays an eastward

tilt with increasing altitude, marking the region of downward wave activity flux and a tropospheric trough that develops over eastern North America from day 0 to day 10. This change in vertical phase line is also pronounced for the planetary wave-1 alone (black lines in Figure 3.5.5). The amplification and increasingly more barotropic structure of the stratospheric ridge over North America from day -5 to day 5 might be thought of as local planetary wave reflection, although the zonal mean of vertical wave flux at 100 hPa is positive throughout the wave event (Figure 3.5.2) and thus does not meet the criterion of planetary wave reflection for a given zonal mean background flow (Shaw et al., 2010).

To understand the contributions of stratosphere-troposphere coupling to the anomalous SAT, we further analyze two idealized simulations of an atmospheric global circulation model with a well-resolved stratosphere (i.e., control (CTL) and nudged (NUDG) runs in SC-WACCM4; See details in Methods). The NUDG run is the same as CTL, except that the model's prognostic variables in the stratosphere are nudged to the corresponding stratospheric evolution in CTL while the underlying troposphere is allowed to evolve freely, with the nudging strength gradually decreasing to zero below 90 hPa. The evolution of the stratosphere in the NUDG run is almost the same as CTL, and thus the same stratospheric wave events are selected based on the 10-hPa wave index as in CTL (1.14 weak and 1.31 strong wave events per year on average).

In the CTL experiment, the surface composite of strong wave events (Figure 3.5.6b) is similar to that in ERA5 (Figure 3.5.6a), with a transition from anomalous North American warming before the event onset to cooling by day 10, as well as the cyclonic anomaly in SLP near Greenland 5–10 days after the onset. While the stratospheric circulation in the NUDG simulation is almost the same as that in the CTL run, the small differences from CTL produce

distinct trajectories in tropospheric weather due to the chaotic nature of weather, and thus the stratospheric wave events produced by nudging are decoupled from tropospheric weather precursors. Indeed, the NUDG experiment cannot reproduce the SAT and SLP anomalies before the event onset in CTL and reanalysis (Figure 3.5.6). In contrast, as the stratospheric wave events often bear a large vertical scale, nudging the stratospheric component of a deep wave structure may produce the surface signatures of stratospheric waves due to vertical wave coupling. This is manifested by the North American cooling and Eurasian warming 10 days after the event onset, similar to CTL and reanalysis (Figure 3.5.6).

We now link the distinct surface evolution in CTL and NUDG runs to vertical wave coupling. In the CTL run, an anomalous ridge over North America extends from the troposphere to the stratosphere and becomes increasingly barotropic from day -5 to day 5, and an anomalous tropospheric trough starts to emerge over Eastern North America 5 days after the event onset (Figure 3.5.5b), similar to ERA5 (Figure 3.5.5a). The NUDG experiment displays the same stratospheric evolution throughout the events as the CTL simulation by design, but the tropospheric precursors are absent on day -5, as tropospheric weather precursors are decoupled from the stratospheric evolution produced by nudging due to the chaotic behavior inherent in weather. Interestingly, the NUDG run exhibits a coherent eastward tilt of the ridge and trough anomalies with increasing height starting from the event onset, and therefore these tropospheric anomalies occurring after the event onset are plausibly linked to the stratospheric conditions nudged to the CTL simulation. This eastward tilt in wave phase after the event onset indicates that an anomalous tropospheric trough over Eastern North America below the anomalous stratospheric ridge (Figure 3.5.5b-c), which, in turn, corresponds to the cyclonic anomaly in SLP over Greenland and cold air advection over North America (Figure 3.5.6). While additional theoretical analysis is required to understand

whether this vertical wave coupling over North America is due to planetary wave reflection (Cohen et al., 2021; Kretschmer et al., 2018; Messori et al., 2022) or other mechanisms, these results provide evidence that the vertical coupling between stratospheric and tropospheric waves plays a key role in the North American cold anomalies following strong stratospheric wave events.

Finally, since the lowest SAT over North America on February 13, 2021 is followed by a local minimum of the stratospheric wave index on February 18 (Figure 3.5.3e), we use the nudging simulations to test the causal relationship between surface cold wave events and concurrent weak stratospheric wave activity. Weak stratospheric wave events in the NUDG simulations show similar results as strong wave events but with opposite signs (Figure 3.A.6). The cold anomalies before and around weak wave events largely diminish in the NUDG simulation, implying a tropospheric rather than stratospheric origin for the North American cold. This suggests a predominant role of tropospheric variability in the February 2021 cold spell, consistent with previous studies (Albers et al., 2022; Davis et al., 2022).

3.4 Discussion

Considering the proposed linkage between stratospheric polar vortex stretching and cold extremes over North America such as the February 2021 cold wave (Cohen et al., 2021), we have investigated the robustness and mechanisms of the contributions of extreme stratospheric wave events to surface cold anomalies. Using observations and the historical simulations of 30 CMIP6 models, we show that strong stratospheric wave events, due to the constructive interference between transient and climatological planetary waves (Figure 3.A.1), are characterized by a polar vortex displacement to Eurasia, followed by an increased risk of cold air outbreaks over North America 5–25 days later (Figure 3.5.4). This suggests

that strong stratospheric wave events can be used as a predictor for North American cold events on sub-seasonal timescales.

Importantly, extreme stratospheric wave events are accompanied by intraseasonal fluctuations between warm and cold spells over North America (Figure 3.5.3), which are distinct from the well-known surface influences of the stratosphere such as SSWs and strong vortex events that increase the intraseasonal persistence of weather regimes (Baldwin & Dunkerton, 2001; Butler et al., 2017; Domeisen, 2019; Garfinkel et al., 2017; Hitchcock & Simpson, 2014; Karpechko et al., 2017; Polvani & Waugh, 2004; Sigmond et al., 2013) or the lower-stratospheric planetary wave reflection events (Cohen et al., 2021; Kretschmer et al., 2018). While SSWs are followed by negative AO on weekly to monthly timescales (Baldwin & Dunkerton, 2001; Domeisen, 2019; Sigmond et al., 2013), the cold anomalies over North America and positive NAO following strong wave events largely vanish 25 days later (Figure 3.5.3). This relatively short timescale of strong wave events implies a distinct physical mechanism from SSWs (Ding et al., 2022). If one takes a time average of 20 days or longer around the strong wave event onset, the North American warming precursor would overwhelm the following cooling signal, leading to weak surface warming associated with strong wave events. This is partly why this lead-lag relationship between strong stratospheric wave activity and surface cooling received little attention in the literature (J. Huang et al., 2018; Liang et al., 2022). Moreover, under certain circumstances, a weak stratospheric wave event may transition to a strong wave event that in turn precedes surface cold anomalies, which may be thought of as an intraseasonal mode of stratosphere-troposphere oscillation (Shen et al., 2022). Although some strong stratospheric wave events are indeed preceded by negative planetary wave indices, the stratospheric conditions prior to

strong wave events exhibit a very large uncertainty, indicating a small signal-to-noise ratio beyond the timescale of a strong wave event (Figure 3.A.7).

We further demonstrate in observations and idealized nudging simulations that the vertical coupling between stratospheric and tropospheric waves is key to the observed North American cooling following strong stratospheric wave events. Strong wave events feature upward and eastward wave activity fluxes in the lower stratosphere over Siberia and downward wave activity fluxes over northern North America, and the latter corresponds to an anomalous tropospheric trough (Figure 3.5.5b-c) and associated cold anomalies over North America (Figure 3.5.6) 5–25 days later. The upward fluxes over Siberia might also be traced back to tropospheric precursors that further extend the timescale of predictability. Future work may use the Subseasonal to Seasonal Prediction (S2S) data set (Domeisen, Butler, et al., 2020b; Domeisen, Grams, et al., 2020) or linear inverse model (LIM) (Albers et al., 2022) to quantify the contributions of extreme stratospheric wave events to surface variability as compared with other sources of intraseasonal predictability. These findings can potentially improve the predictability of severe winter cold events in the U.S. and Canada and consequently benefit the transportation sector (Hou et al., 2022; Vajda et al., 2014), energy planning and use (Perera et al., 2020; Yalew et al., 2020), and human health (Charlton-Perez et al., 2019; W. T. K. Huang et al., 2020).

Acknowledgments. We acknowledge the WCRP Working Group on Coupled Modeling which is responsible for the CMIP. We also acknowledge high-performance computing support from Cheyenne (https://doi.org/10.5065/D6RX99HX) provided by NCAR's Computational and Information Systems Laboratory, sponsored by the National Science Foundation. G.C. is supported by the U.S. NSF grant AGS-2232581 and NASA grant 80NSSC21K1522. Support

from the Swiss National Science Foundation through project PP00P2_198896 to D.I.V.D. is gratefully acknowledged.

3.5 Figures

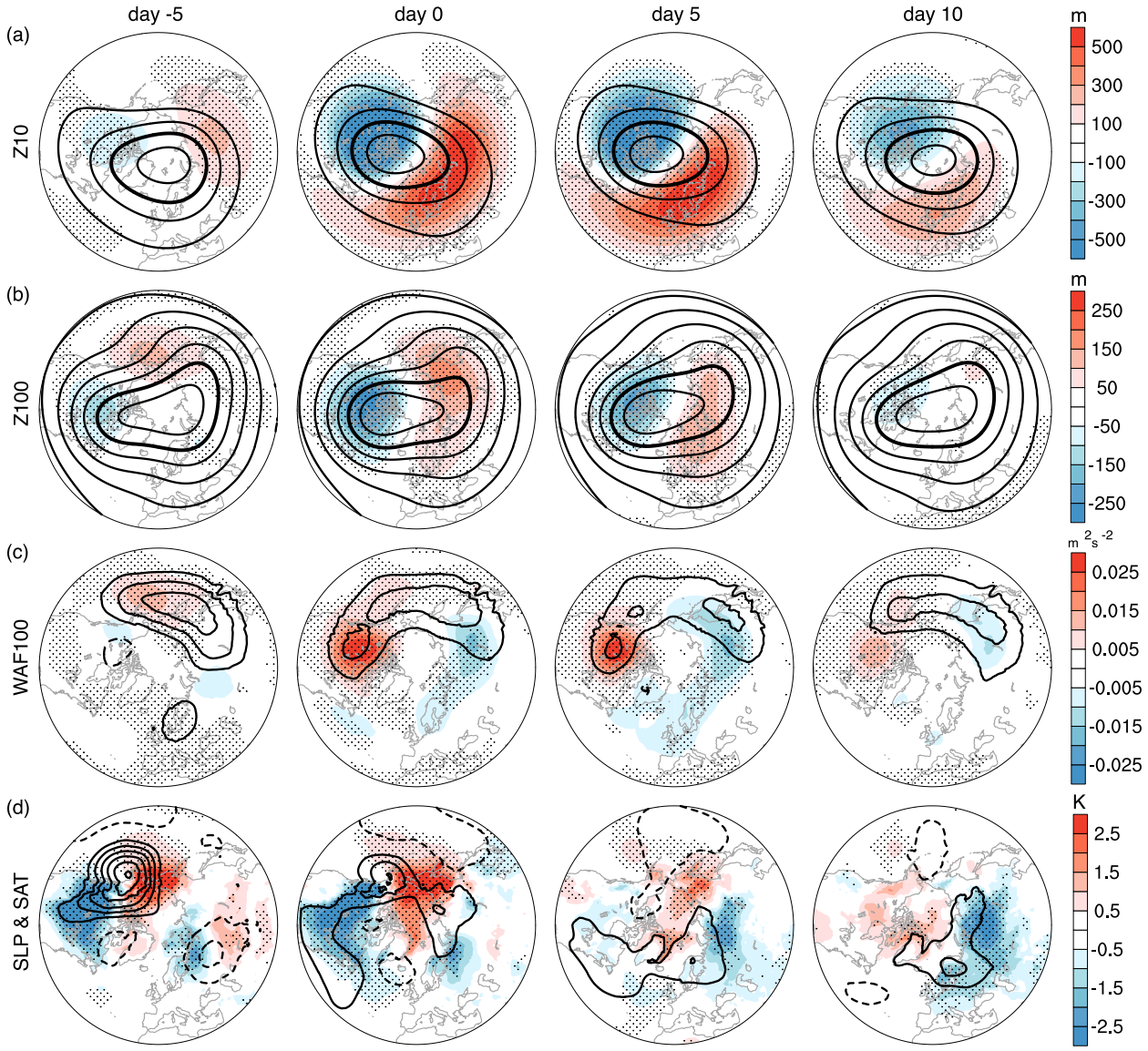

Figure 3.5.1: Weak stratospheric wave events in ERA5 reanalysis. Composites of days -5, 0, 5 and 10 with respect to the onset of weak stratospheric wave events: a, 10-hPa geopotential height (contours at 500 m intervals, 29000 m contour bolded, anomalies shaded). b, 100-hPa geopotential height (contours at 200 m intervals, 15200 m contour bolded, anomalies shaded). c, 100-hPa vertical component of Plumb wave activity flux (contours at 0.01 m2s−2 intervals, anomalies shaded). d, anomalous SLP (contours at 2 hPa intervals) and SAT (shading). The time evolution is smoothed by a 5-day running average (i.e. day -5 is the average of days -7 to -3). The weak wave events are defined by the 5th percentile of the first principal component of the zonally asymmetric component of 10-hPa geopotential height. See details in Methods. Stippling indicates the regions where the anomalies are significant at the 95% confidence level based on the Student's *t*-test.

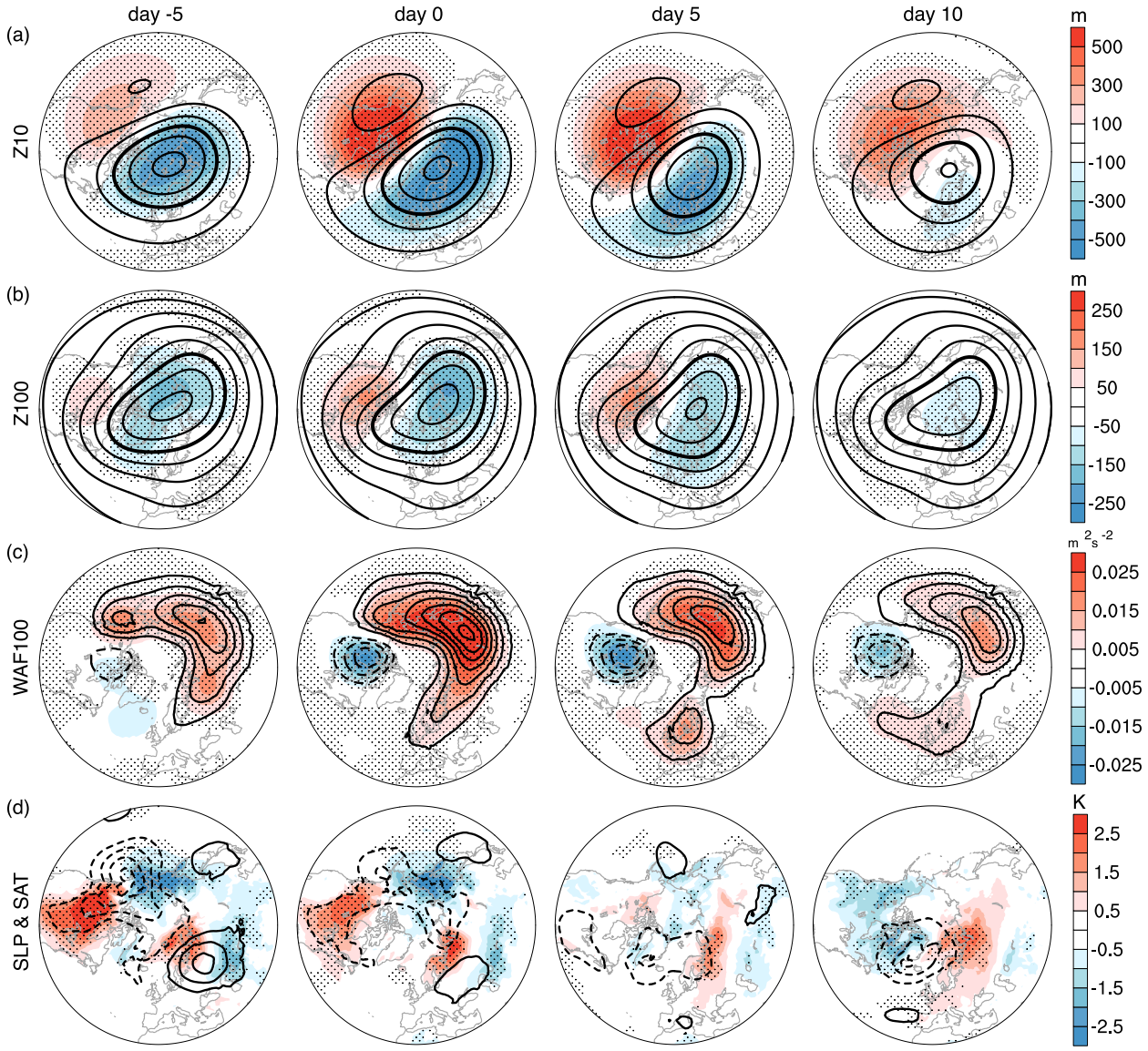

Figure 3.5.2: Strong stratospheric wave events in ERA5 reanalysis. As in Figure 3.5.1, but for composites of strong stratospheric wave events. The strong wave events are defined by the 95th percentile of the first principal component of the zonally asymmetric component of 10-hPa geopotential height. See details in Methods.

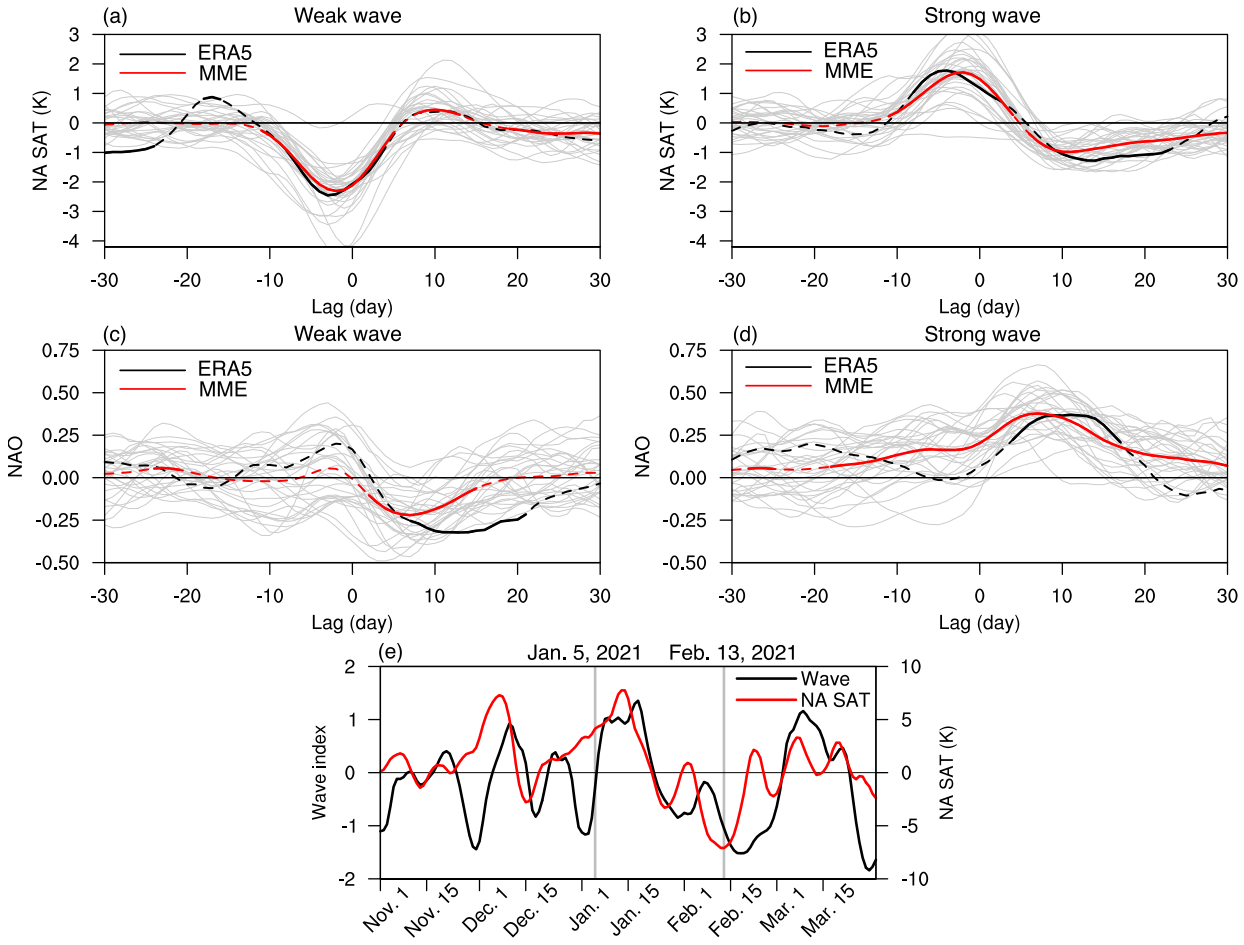

Figure 3.5.3: Evolution of North American SAT anomalies linked to extreme stratospheric wave events. a-b, Composites of North American SAT (NA SAT) anomalies for weak (a) and strong (b) stratospheric wave events in ERA5 reanalysis and CMIP6 models. ERA5 is depicted as black lines, the CMIP6 multi-model ensemble (MME) means in red, and individual models in light gray. c-d, As in (a-b), but for the NAO index. e, Evolution of the stratospheric wave index and NA SAT anomalies for winter 2020/2021. Solid parts of the lines for ERA5 and CMIP6 MME in (a-d) represent the composites significant at the 95% confidence level based on the Student's *t*-test. Gray lines in (e) denote the onset date of the SSW on January 5, 2021, and the lowest NA SAT on February 13, 2021, for the winter. NA SAT anomalies are averaged over the land regions of 40◦–70◦N, 70◦–130◦W. The NAO index is defined as the SLP difference between 20◦–55◦N, 90◦W–60◦E and 55◦–90◦N, 90◦ W–60◦ E.

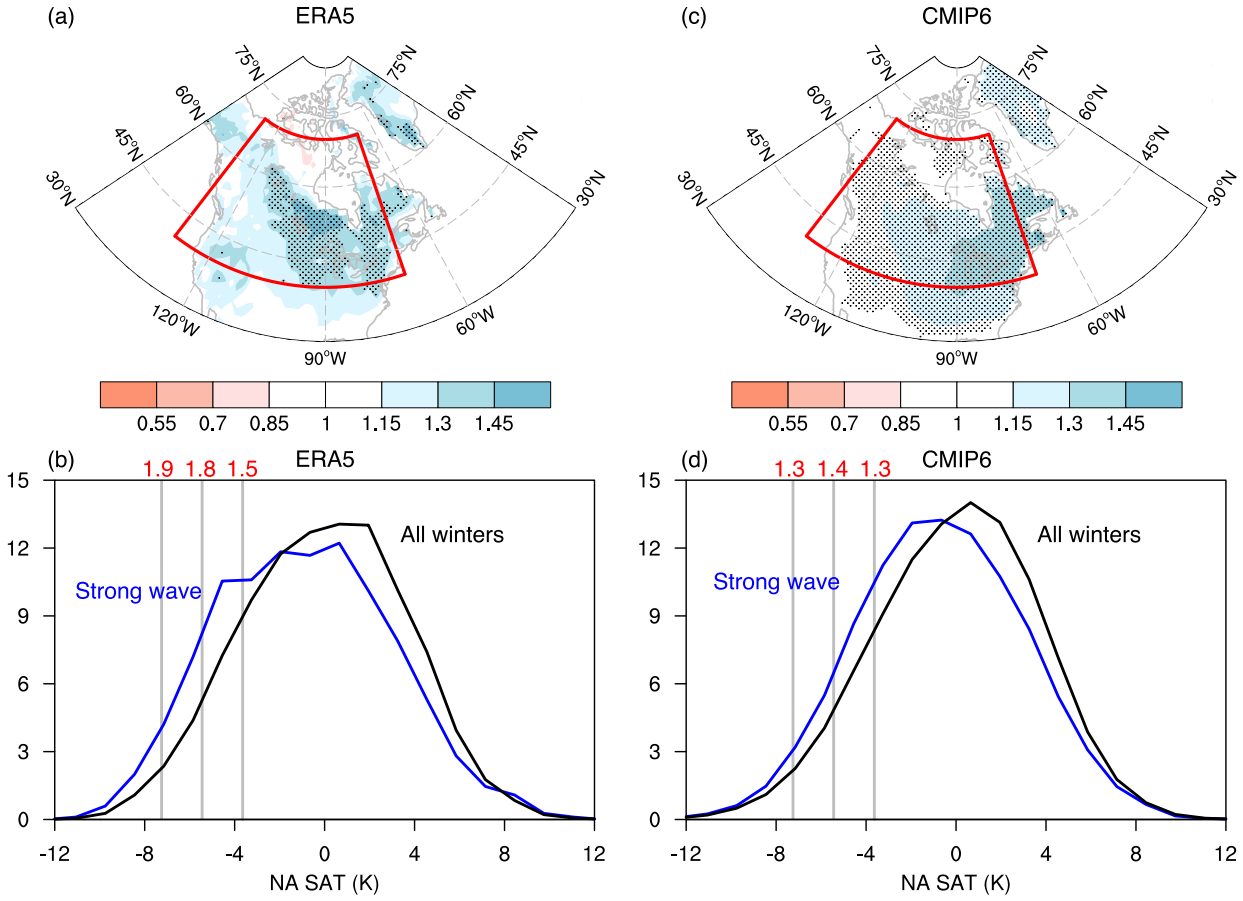

Figure 3.5.4: Risk ratio of extreme cold days and probability density function (PDF) of NA SAT anomalies following strong stratospheric wave events. a-b, The spatial pattern of the risk ratio of extreme cold days (a) and the PDF of NA SAT anomalies (b) in ERA5 during days 5–25 after the onset of strong stratospheric wave events, compared with the statistics of all winters. The risk ratio in (a) is defined as the probability of cold days (i.e., SAT is at least 1.5 SD below its climatology) in days 5–25 divided by the probability of cold days in any random 21-day period in winter. Stippling indicates where the risk ratio is significant at the 95% confidence interval based on a Student's *t*-test. c-d, As in (a-b), but for CMIP6 models. The red boxes in (a) and (c) indicate the region where the NA SAT anomalies are calculated. The vertical gray lines in (b) and (d) denote -1, -1.5, and -2 SD of NA SAT anomalies in all the winter days, and the values in red depict the risk ratios of the exceedance frequency due to strong wave events.

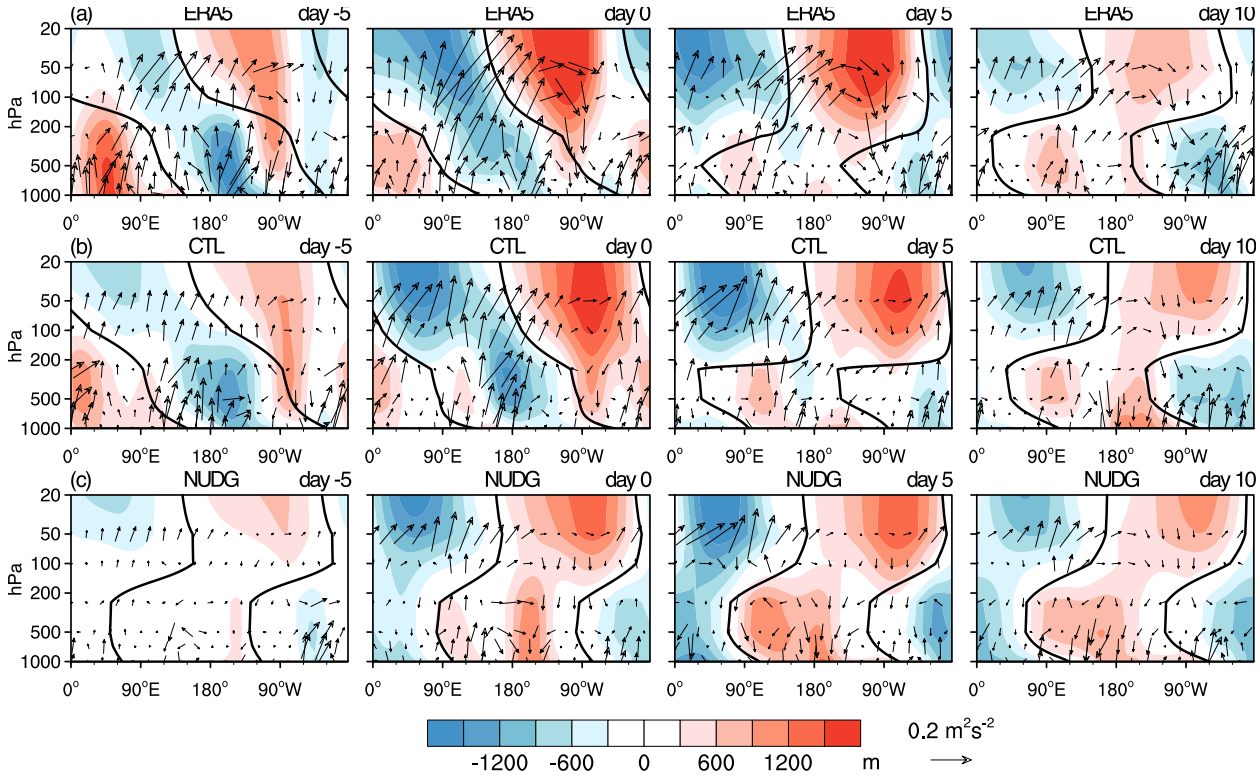

Figure 3.5.5: Vertical wave coupling during strong stratospheric wave events. a, Composites of the zonally asymmetric component of anomalous geopotential height (shading) and the vertical and zonal components of anomalous Plumb wave activity flux (vector) averaged over 50◦–70◦N as a function of longitude and pressure on days -5, 0, 5 and 10 in ERA5. b-c, As in (a), but for the CTL (b) and NUDG (c) experiments of SC-WACCM4. Black lines are zero contours of the wave-1 component of anomalous geopotential height, indicating the phase tilt of wave-1. To account for the smaller air density with decreasing pressure, the magnitude of the Plumb flux is scaled by $(1000/p)^{1/2}$, and geopotential height is scaled by $(p/1000)^{1/2}$, where p is pressure. The vertical component of the Plumb flux is also scaled by a factor of 200. See Figure 3.A.8 for the total field of anomalous height and absolute Plumb flux.

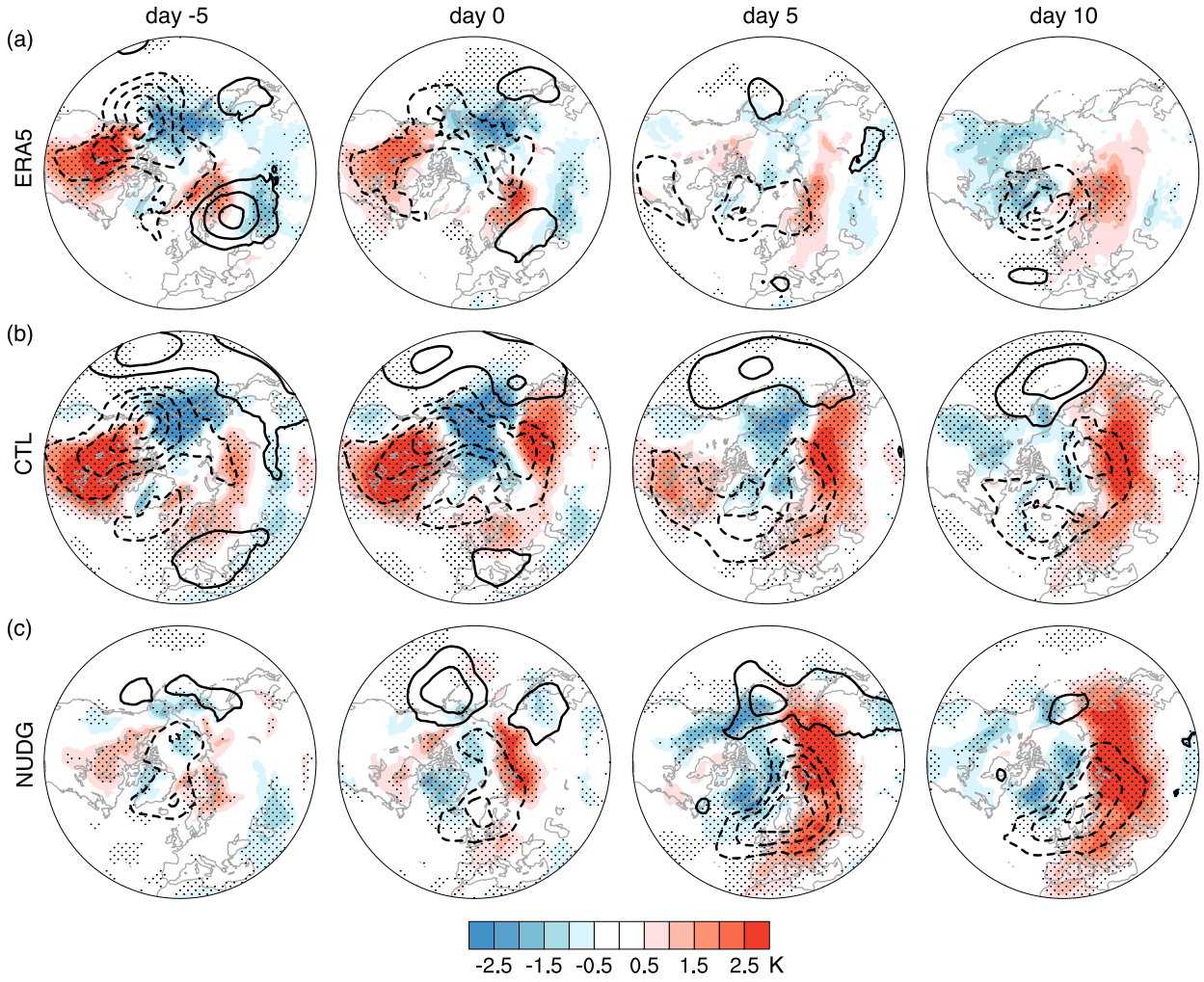

Figure 3.5.6: Surface signatures of strong stratospheric wave events in SC-WACCM4. Composites of anomalous SLP (contours at 2 hPa intervals) and SAT (shading) for the CTL (b) and NUDG (c) experiments of SC-WACCM4, as compared with ERA5 (a, same as Figure 3.5.2d). Stippling indicates the regions where the SAT anomalies are significant at the 95% confidence level based on the Student's *t*-test.

3.A Appendices

Table 3.A.1: List of the CMIP6 models used in this study.

Model	No. of Vertical Levels	Lid Height (hPa)	Ensemble Member
ACCESS-CM2	85	0.0054	r1i1p1f1
AWI-ESM-1-1-LR	47	0.011	r1i1p1f1
BCC-ESM1	26	2.19	r1i1p1f1
CESM2	32	2.25	r1i1p1f1
CESM2-WACCM	70	4.5e-6	r1i1p1f1
CNRM-CM6-1	91	0.014	r1i1p1f2
CNRM-CM6-1-HR	91	0.014	r1i1p1f2
CNRM-ESM2-1	91	0.014	r1i1p1f2
CanESM5	49	1	r1i1p1f1
EC-Earth3	91	0.01	r1i1p1f1
FGOALS-f3-L	32	2.16	r1i1p1f1
FGOALS-g3	26	2.19	r1i1p1f1
GFDL-ESM4	49	1	r1i1p1f1
GISS-E2-1-G	40	1	r1i1p1f2
GISS-E2-2-G	102	0.002	r1i1p1f1
HadGEM3-GC31-LL	85	0.0054	r1i1p1f3
HadGEM3-GC31-MM	85	0.0054	r1i1p1f3
INM-CM4-8	21	10	r1i1p1f1
INM-CM5-0	73	0.2	r1i1p1f1
IPSL-CM6A-LR	79	0.011	r1i1p1f1
KACE-1-0-G	85	0.0054	r1i1p1f1
MIROC-ES2L	40	3	r1i1p1f2
MIROC6	81	0.004	r1i1p1f1
MPI-ESM-1-2-HAM	47	0.01	r1i1p1f1
MPI-ESM1-2-HR	95	0.01	r1i1p1f1
MPI-ESM1-2-LR	47	0.01	r1i1p1f1
MRI-ESM2-0	80	0.01	r1i1p1f1
NorESM2-LM	32	3	r1i1p1f1
NorESM2-MM	32	3	r1i1p1f1
UKESM1-0-LL	85	0.0054	r1i1p1f2

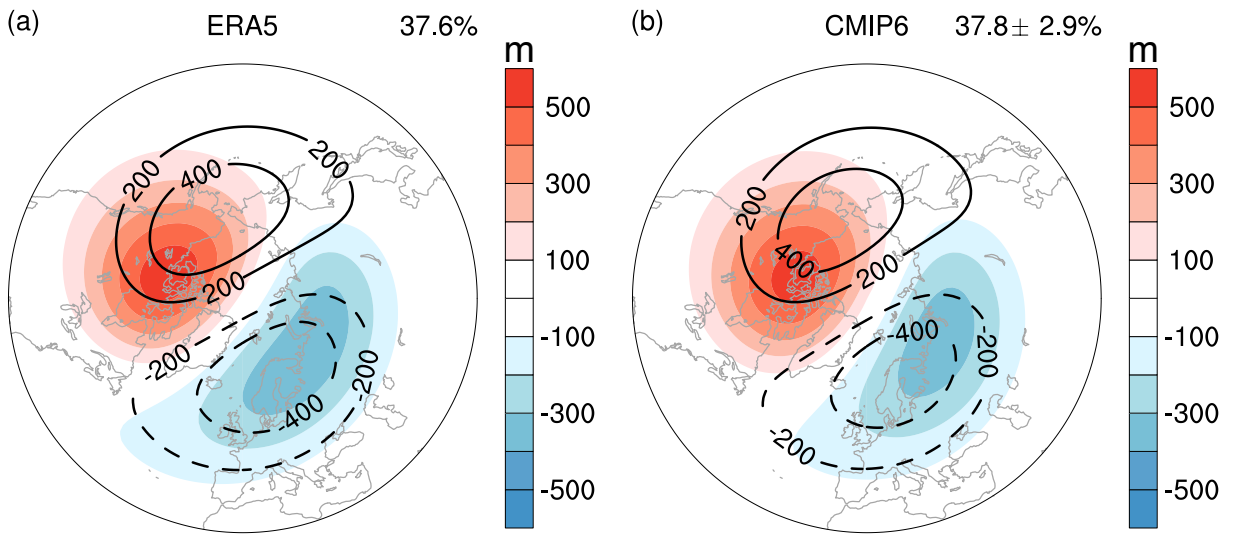

Figure 3.A.1: Leading EOFs of the zonally asymmetric component of 10-hPa geopotential height. a-b, The leading EOF pattern for ERA5 (a) and the multi-model mean of leading EOFs of CMIP6 models (b). The climatological wave pattern is shown in black contours. The percentage of variance explained by the leading EOF is depicted at the upper right corner. The uncertainty of CMIP6 models is given as the SD among 30 models.

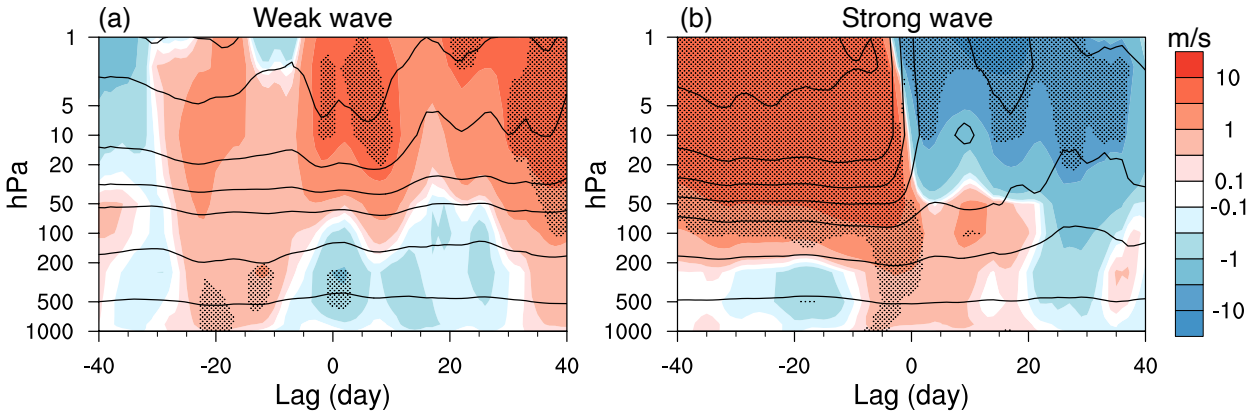

Figure 3.A.2: Zonally averaged high-latitude zonal wind for extreme stratospheric wave events in ERA5. a-b, Zonal wind (contours at 10 m s−1, anomalies shaded) averaged over 60◦–90◦N during weak stratospheric wave events (a) and strong stratospheric wave events (b). A 5-day running average is applied. Stippling indicates the regions where the anomalies are significant at the 95% confidence level based on the Student's *t*-test.

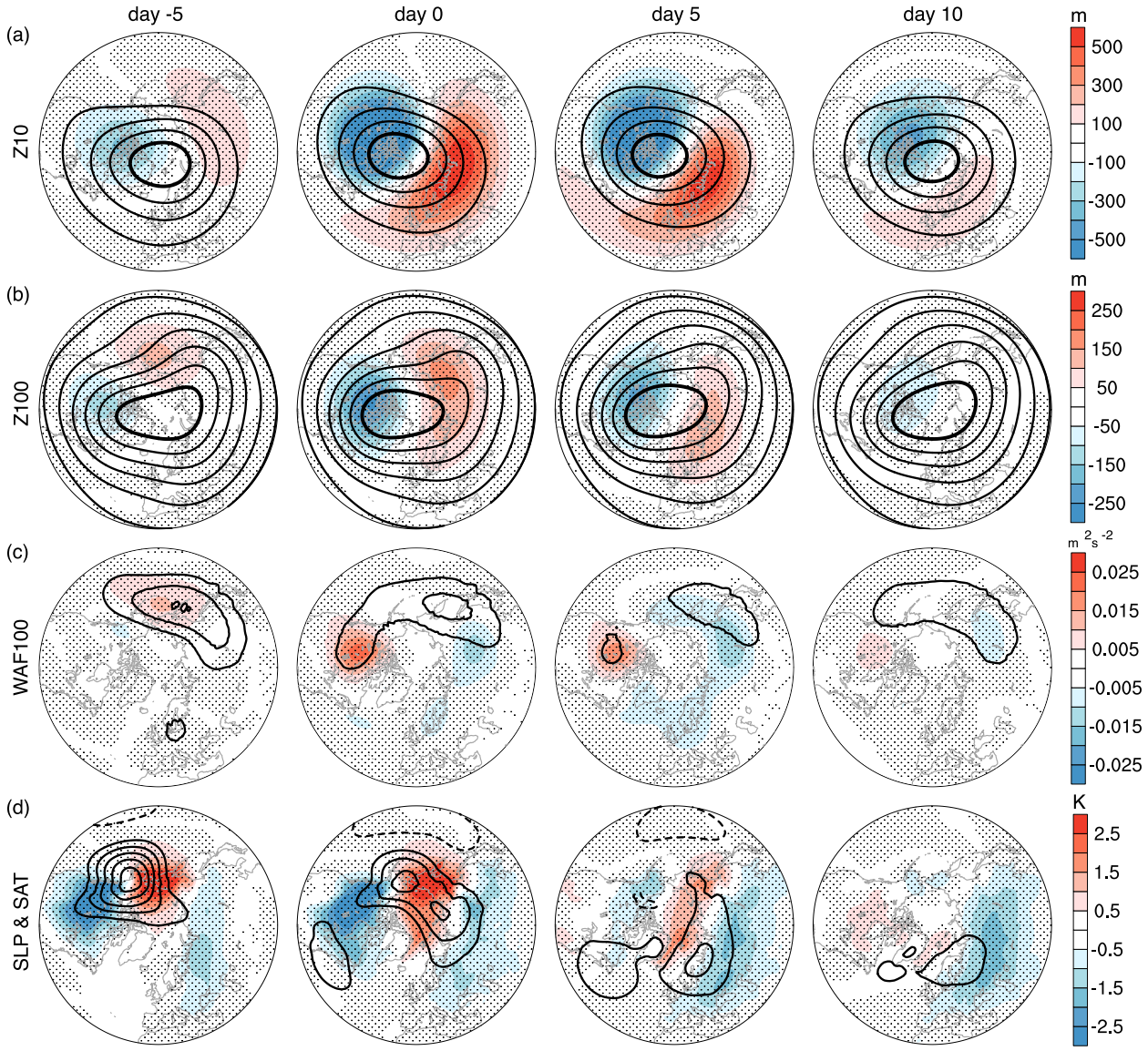

Figure 3.A.3: Weak stratospheric wave events in CMIP6 models. As in Figure 3.5.1, but for the composites in CMIP6 models. See details of CMIP6 models in Methods.

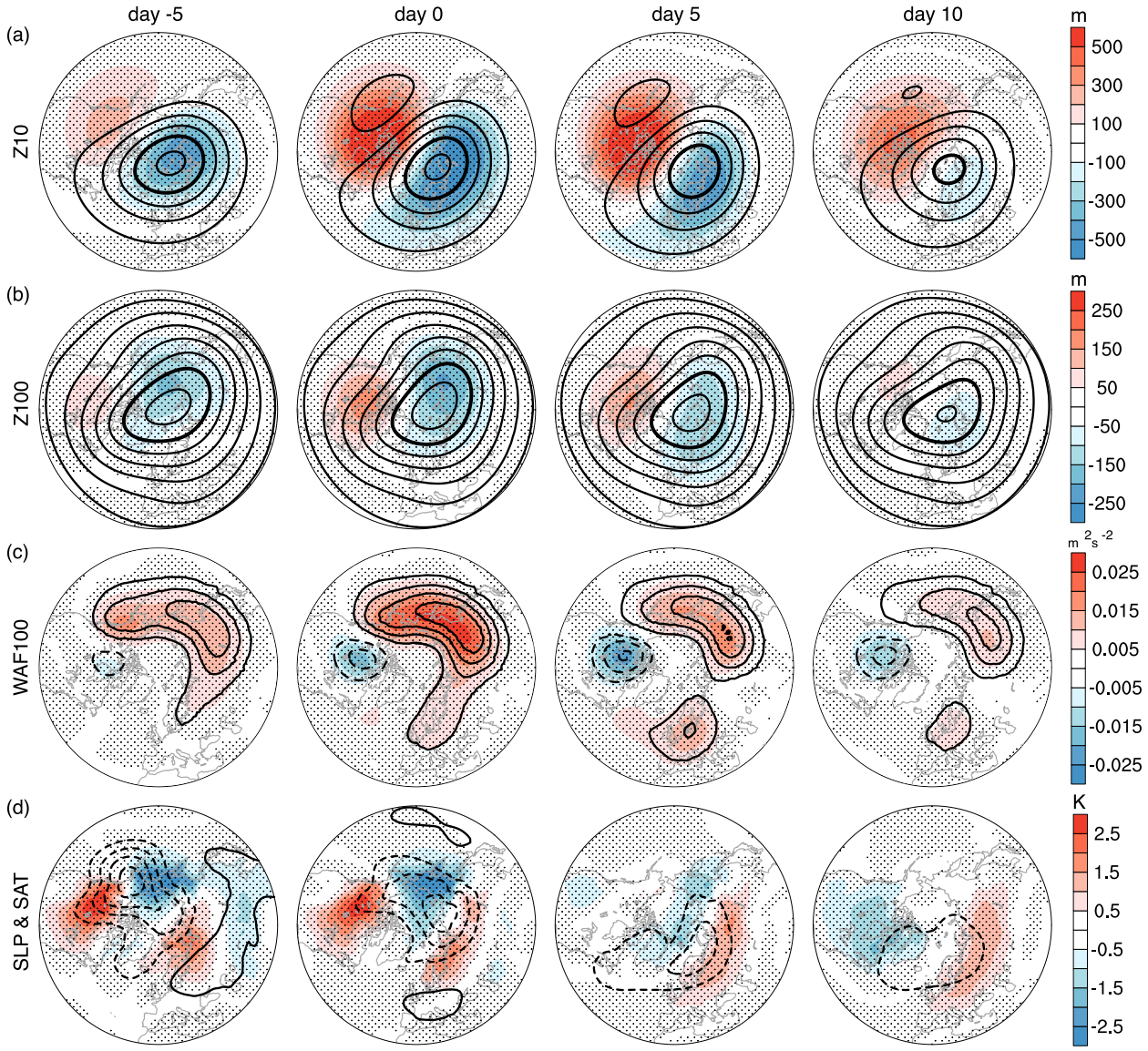

Figure 3.A.4: Strong stratospheric wave events in CMIP6 models. As in Figure 3.5.2, but for the composites in CMIP6 models. See details of CMIP6 models in Methods.

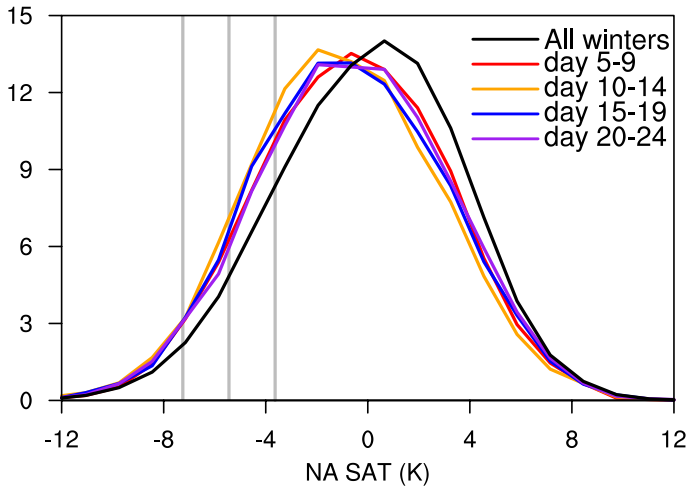

Figure 3.A.5: PDF of NA SAT anomalies following strong stratospheric wave events in CMIP6. As in Figure 3.5.4d, but for finer time windows (i.e., day 5–9, day 10–14, day 15–19, and day 20–24). The vertical gray lines denote -1, -1.5, and -2 SD of NA SAT anomalies in all the winter days.

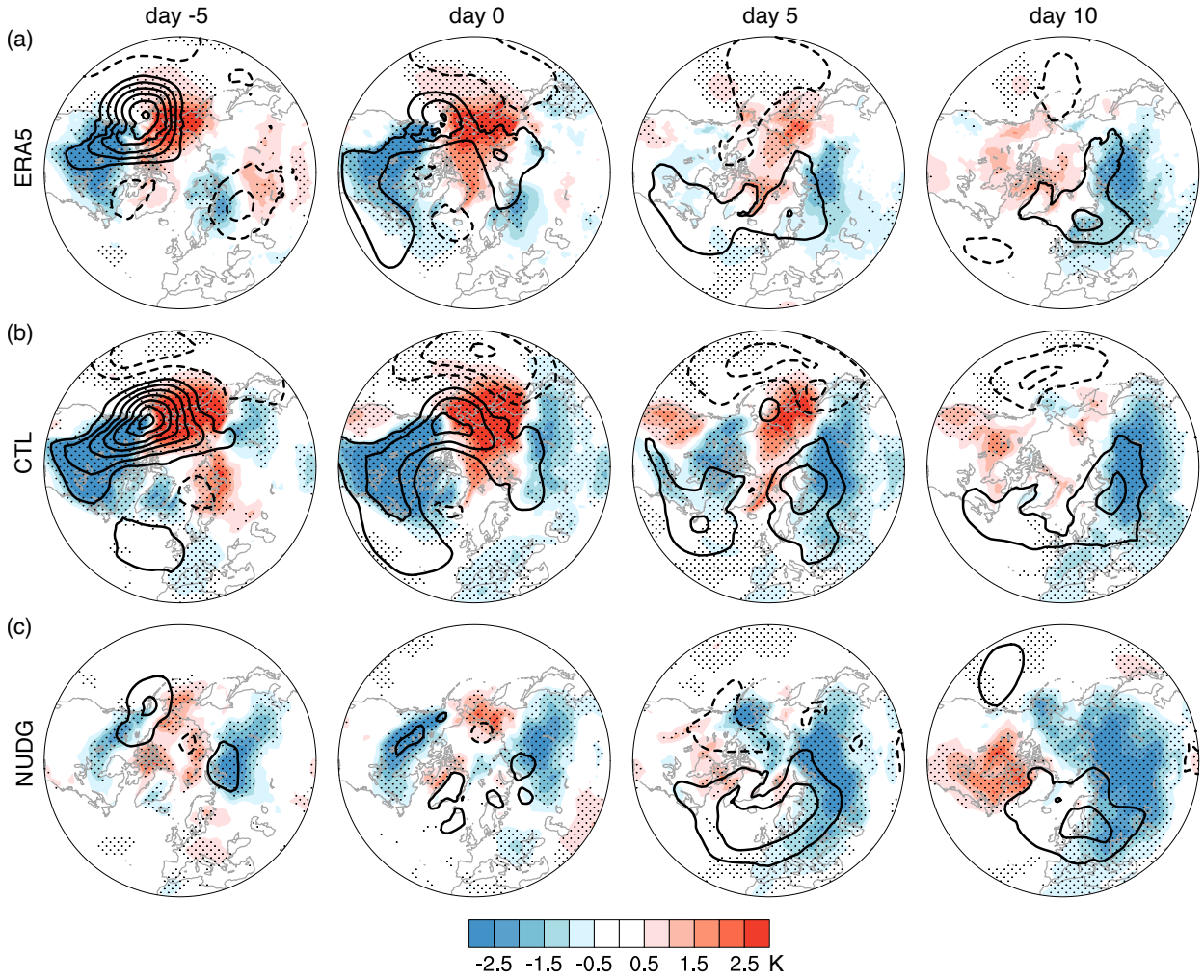

Figure 3.A.6: Surface signatures of weak stratospheric wave events in SC-WACCM4. Composites of anomalous SLP (contours at 2 hPa intervals) and SAT (shading) for the CTL (b) and NUDG (c) experiments of SC-WACCM4, as compared with ERA5 (a, same as Figure 3.5.1d). Stippling indicates the regions where the SAT anomalies are significant at the 95% confidence level based on the Student's *t*-test.

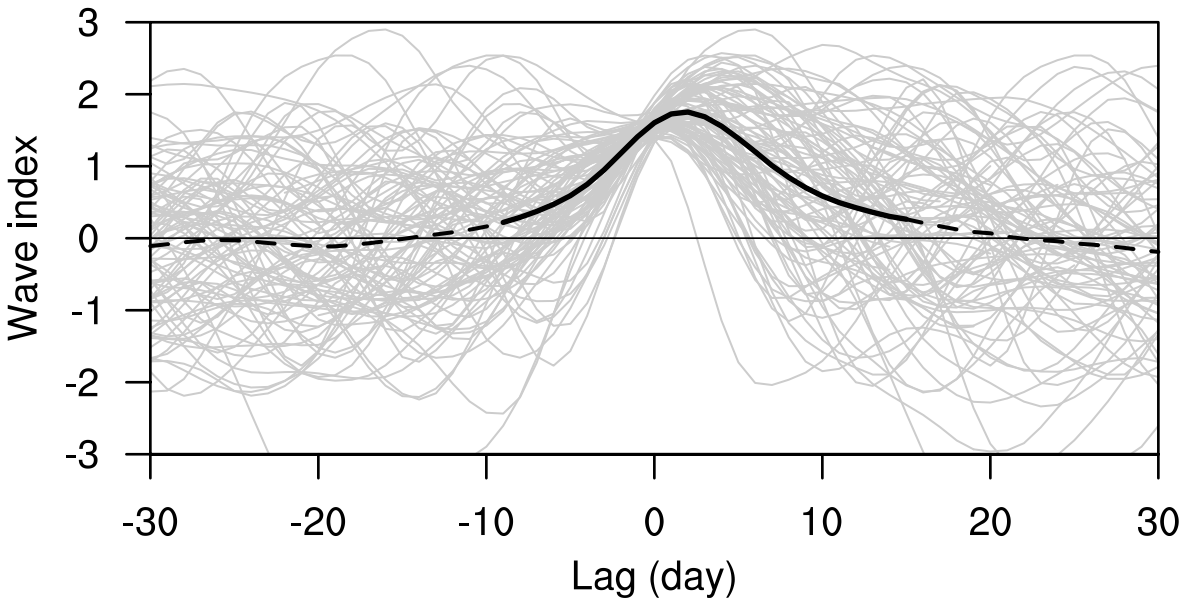

Figure 3.A.7: Evolution of the planetary wave index linked to strong stratospheric wave events in ERA5. Composites of all the events are depicted as the black line and individual events are shown in light gray. Solid parts of the line represent the composites significant at the 95% confidence level based on the Student's *t*-test.

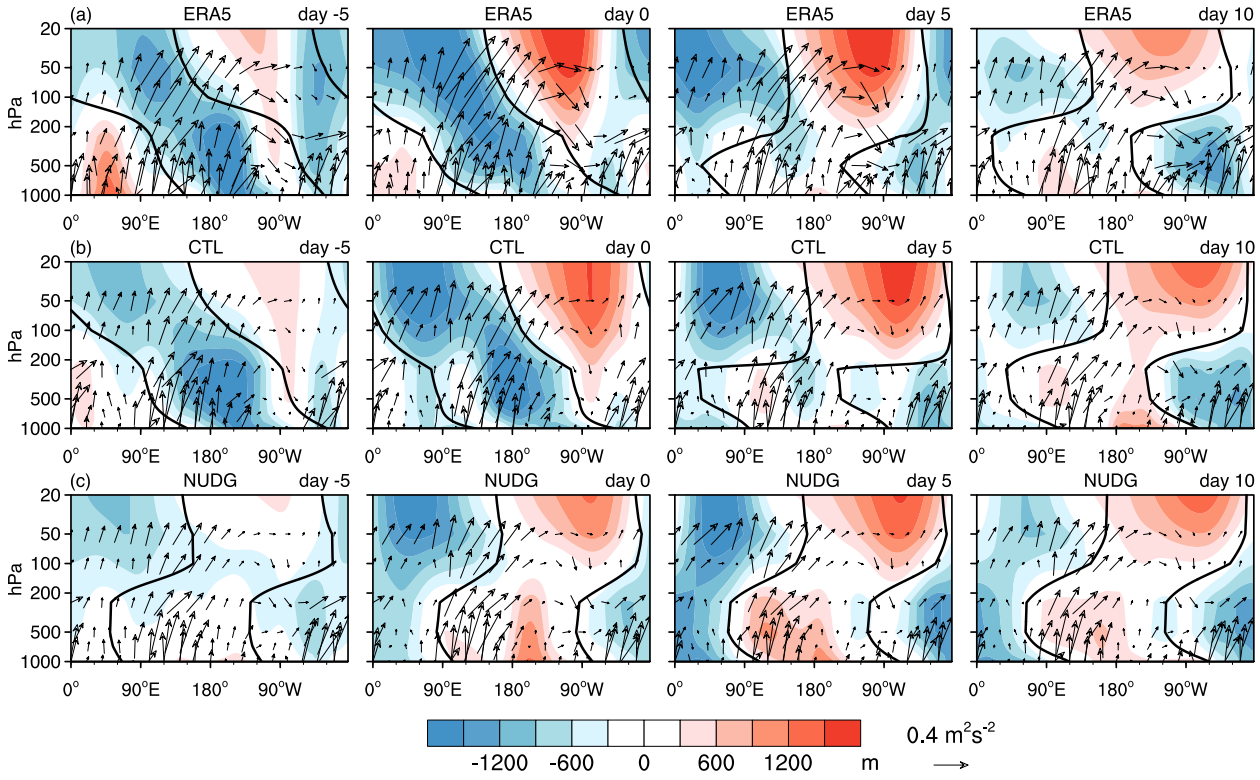

Figure 3.A.8: Vertical wave coupling during strong stratospheric wave events. As in Figure 3.5.5, but for composites of the total field of anomalous geopotential height (zonal mean plus zonal asymmetry, shading) and the vertical and zonal components of absolute Plumb wave activity flux (climatology plus anomalies, vector).

CHAPTER 4

Stratosphere-Troposphere Coupling of Extreme Stratospheric Wave Activity in CMIP6 Models

[**Ding, X.,** Chen, G., & Ma, W. (2023). Stratosphere-Troposphere Coupling of Extreme Stratospheric Wave Activity in CMIP6 Models. *Journal of Geophysical Research: Atmospheres*, *128*(16), e2023JD038811.]

Abstract

Extreme stratospheric wave activity has been suggested to be connected to surface temperature anomalies, but some key processes are not well understood. Using observations, we show that the stratospheric events featuring weaker-than-normal wave activity are associated with increased North American (NA) cold extreme risks before and near the event onset, accompanied by less frequent atmospheric river (AR) events on the west coast of the United States. Strong stratospheric wave events, on the other hand, exhibit a tropospheric weather regime transition. They are preceded by NA warm anomalies and increased AR frequency over the west coast, followed by increased risks of NA cold extremes and north-shifted ARs over the Atlantic. Moreover, these links between the stratosphere and troposphere are attributed to the vertical structure of wave coupling. Weak wave events show a wave structure of westward tilt with increasing altitudes, while strong wave events feature a shift from westward tilt to eastward tilt during their life cycle. This wave phase shift indicates vertical wave coupling and likely regional planetary wave reflection. Further examinations of CMIP6 models show that models with a degraded representation of stratospheric wave structure exhibit biases in the troposphere during strong wave events.

Specifically, models with a stratospheric ridge weaker than the reanalysis exhibit a weaker tropospheric signal. Our findings suggest that the vertical coupling of extreme stratospheric wave activity should be evaluated in the model representation of stratosphere-troposphere coupling.

4.1 Introduction

It is widely recognized that stratospheric variability is connected to tropospheric weather conditions during boreal winter (e.g., Baldwin et al., 2021; Domeisen, Butler, et al., 2020b; Sigmond et al., 2013). In the winter stratosphere, a powerful cyclonic system termed the polar vortex develops over the polar region as the result of large solar radiation gradients. The strength of a stratospheric polar vortex is also modulated by wave drag due to planetary waves propagating from the troposphere to the stratosphere (e.g., Charney & Drazin, 1961; Matsuno, 1970). Both weak and strong polar vortex events have been shown to influence the troposphere and surface on sub-seasonal to seasonal timescales (e.g., Baldwin & Dunkerton, 2001; Limpasuvan et al., 2004, 2005).

Several mechanisms are proposed for the stratospheric impacts on the surface, involving different aspects of the planetary wave-zonal flow interaction. Planetary waves propagate upwards into the stratosphere, where waves are absorbed and under certain conditions result in an extremely weak polar vortex, known as sudden stratospheric warming (SSW; Charney & Drazin, 1961; Garfinkel et al., 2010; Polvani & Waugh, 2004). Following SSWs, downward propagation of negative zonal wind anomalies may be amplified and sustained by tropospheric synoptic eddy feedbacks (Domeisen et al., 2013; Gerber et al., 2010; Kushner & Polvani, 2004; Martineau et al., 2018; Song & Robinson, 2004; Sun et al., 2012). The surface signals of SSWs are characterized by the negative phase of the Arctic Oscillation (AO) or

North Atlantic Oscillation (NAO) and more frequent cold spells in the mid-latitudes, particularly in northern Eurasia (Butler et al., 2017; Domeisen & Butler, 2020; Garfinkel et al., 2017; Hitchcock & Simpson, 2014; Kidston et al., 2015; P. Zhang et al., 2020). Another mechanism refers to planetary wave reflection in the stratosphere. Upward-propagating waves from the troposphere get reflected downwards and influence the tropospheric circulation (Perlwitz & Harnik, 2003; Shaw & Perlwitz, 2010). Planetary wave reflection events are linked to a strong stratospheric polar vortex and positive NAO at the surface (Kodera et al., 2013, 2016; Shaw & Perlwitz, 2013). Other mechanisms include the role of the residual circulation (Thompson et al., 2006; Yang et al., 2015), or modulation of tropical deep convection (Collimore et al., 2003; Gray et al., 2018; Liess & Geller, 2012). Moreover, various tropospheric precursors have been identified as the source of anomalous upward wave propagation (Davies, 1981; Garfinkel et al., 2010; Kolstad & Charlton-Perez, 2011; Schneidereit et al., 2017; Sun et al., 2012), including atmospheric blocking over Euro-Atlantic and Pacific (Martius et al., 2009; Nishii et al., 2011; Woollings et al., 2010), Arctic sea ice (B.-K. Kim et al., 2014; Sun et al., 2015; P. Zhang et al., 2018, 2020), and El Niño-Southern Oscillation (ENSO) (Butler et al., 2014, 2016; Butler & Polvani, 2011; Domeisen et al., 2015, Domeisen, Butler, et al., 2020a).

Planetary wave reflection events have drawn increasing attention recently due to their connection to North American (NA) cold spells (e.g., Kretschmer et al., 2018). Particularly, Cohen et al. (2021) argue that a stretched polar vortex in the lower stratosphere, characterized by its horizontal elongation, is linked to NA cold extremes such as the February 2021 Texas cold spell via wave reflection. An important feature of these reflection events is the negative eddy heat flux in the lower stratosphere, which indicates downward wave propagation. Negative extremes of zonal mean eddy heat flux are instantaneously linked to

positive NAO and NA cooling, while positive eddy heat flux extremes are linked to negative NAO and Eurasian cooling (Dunn-Sigouin & Shaw, 2018; Shaw et al., 2014; Shaw & Perlwitz, 2013). Messori et al. (2022) further suggest that reflection events featured by regionally negative eddy heat flux relate to the tropospheric evolution from a Pacific Trough regime to an Alaskan Ridge regime, accompanied by a continental-scale temperature decrease over North America. However, Tan and Bao (2020) find no evidence of wave reflection linked with NA cold spells. They argue that the tropospheric circulation regime associated with NA cold spells only acts as a precursor for the suppressed planetary wave-1 (a wave structure with one crest and one trough at a latitude circle) activity in the stratosphere. Ding et al. (2022, 2023), in contrast, show that strong stratospheric wave activity precedes positive NAO-like NA cooling at the surface with a 10-day lag. The divergent conclusions underscore that the surface impacts of stratospheric waves remain an area of active research.

A key challenge in understanding stratosphere-troposphere coupling is the large internal variability in both the stratosphere and troposphere (Afargan-Gerstman et al., 2022; Charlton-Perez et al., 2018; Kolstad et al., 2022). Only about two-thirds of SSWs are followed by visible downward influences characterized by persistent negative AO, and less than a quarter of negative NAO events are preceded by an SSW (Domeisen, 2019). Davis et al. (2022) find that the February 2021 Texas cold spell is largely attributed to unpredictable internal atmospheric variability, with no discernible contribution from the stratosphere. To deal with the limited sample size of events, one approach is to use large ensembles of model simulations. In comparison with high-top models, low-top models are found to underestimate the SSW frequency (Charlton-Perez et al., 2013). Shaw et al. (2014) demonstrate that a degraded model representation of stratospheric eddy heat fluxes is linked to biases in the troposphere through downward wave coupling. Wu and Reichler (2020) further show that not only a high

model lid but also a fine vertical resolution in the stratosphere is important for properly simulating stratospheric variability.

The role of extreme stratospheric wave events in NA cold extremes is also underexplored in climate models. One possible reason is the challenge in diagnosing these events consistently in different datasets. Previous studies have identified stratospheric wave events using eddy heat fluxes (Dunn-Sigouin & Shaw, 2015), time-integrated upward wave activity flux (Reichler & Jucker, 2022), clustered 100 hPa circulation patterns (Cohen et al., 2021; Kretschmer et al., 2018; Liang et al., 2022), or time-filtered 10 hPa circulation patterns (Shen et al., 2022). However, many of these studies only analyzed reanalyzes, and the sensitivities of these methods are unclear when applied to climate models. Ding et al. (2022) measure stratospheric wave activity with a simple metric based on the EOF analysis of the zonally asymmetric component of 10 hPa geopotential height, which can be readily applied to climate models. Ding, Chen, Zhang, et al. (2023) further show the impact of extreme stratospheric wave events on NA cold spells consistently across reanalysis and Coupled Model Intercomparison Project Phase 6 (CMIP6) ensemble means. The present study will assess extreme stratospheric wave activity in CMIP6 models. We examine the stratosphere-troposphere coupling of extreme stratospheric wave activity, including the impacts on temperature and precipitation extremes. We also quantify the statistical relationship between stratospheric and tropospheric circulation anomalies in the CMIP6 model ensemble for the vertical wave coupling during strong wave events.

Besides the well-studied surface signatures of stratospheric variability, we will examine the frequency of Atmospheric rivers (ARs) that play an important role in the hydroclimate. ARs are narrow regions of strong horizontal water vapor transport, responsible for more than 90%

of the poleward moisture transport at midlatitudes (Zhu & Newell, 1998). They can lead to extreme events including extreme precipitation (W. Ma et al., 2020), extreme wind events (Waliser & Guan, 2017) and flooding (Leung & Qian, 2009), particularly along the western coasts of North America and Europe. Recent studies show that anomalies in the strength of stratospheric polar vortex can influence the frequency of ARs and the associated precipitation through an anomalous tropospheric jet (Baek et al., 2023; Lee et al., 2022; W. Ma & Chen, 2022). However, given the distinct planetary wave mechanism and surface impacts, the potential influence of extreme stratospheric wave events on ARs remains elusive.

The paper is organized as follows. Section 4.2 describes the data, definition of stratospheric wave event, and AR detection. In Section 4.3, we analyze the linkages between stratospheric wave activity and tropospheric extremes in the reanalysis data. Section 4.4 examines the representation of stratospheric wave activity in CMIP6 models and its linkage to the troposphere. Section 4.5 draws a comparison between stratospheric wave events and several other types of stratospheric events. Section 4.6 provides a summary.

4.2 Data and Methods

4.2.1 Observations and CMIP6 Models

We use the fifth generation of atmospheric reanalysis from the European Center for Medium-Range Weather Forecasts (ERA5; Hersbach et al., 2020). The daily data we analyzed has a spatial resolution of 1.5° × 1.5°. We focus on the extended boreal winter from November to March over the period of 1950–2021. After detrending, we remove the seasonal cycle in the data, which is defined as the time mean and first two harmonics of the full-year climatology.

We also analyze the historical simulations from 30 CMIP6 models. The daily data covers the period of 1950–2014 (except that GISS-E2-2-G covers 1970–2014 due to limited data availability). All model data are bilinearly interpolated to a common grid of 1.5° × 1.5°. Only one member in each model ensemble is used. The list of CMIP6 models, the ensemble members used, and lid height are briefly summarized in Table 4.A.1. In addition to the CMIP6 ensemble, we examine another model ensemble by incorporating eight additional members of CESM2, constituting a 9-member CESM2 ensemble. Because each member of this CESM2 ensemble differs only by small perturbations to initial conditions, their differences are attributed to the internal variability of the climate system. We repeat the CMIP6 analysis with this 9-member ensemble to estimate the internal variability in CESM2.

4.2.2 Definition of Extreme Stratospheric Wave Events

We define extreme stratospheric wave events based on the EOF analysis of 10 hPa geopotential height for ERA5 and individual CMIP6 models, as in Ding et al. (2022). After removing the zonal mean, EOF is applied to the zonally asymmetric component of geopotential height at 10 hPa north of 20°N, weighted by the square root of the cosine of latitudes. The stratospheric planetary wave index is defined as the standardized principal component of the leading EOF mode. The positive/negative phase of the wave index largely describes the intensification/ weakening of the planetary wave-1 in the stratosphere (Figure 4.7.1), due to constructive/destructive interference with the climatological wave-1 (K. L. Smith & Kushner, 2012). A weak stratospheric wave event is then defined as the consecutive days when the planetary wave index is below its fifth percentile, and a strong wave event is defined as the consecutive days when the index is above its 95th percentile. No minimum duration is required to detect an event. Day 0 refers to the first day that meets the event

definition. Day −5 denotes 5 days before day 0, and day 5 indicates 5 days after day 0. This definition yields 89 weak wave events and 93 strong wave events out of 71 winters in ERA5 and on average 82 weak and 85 strong events out of 64 winters in 30 CMIP6 models. We note that the leading EOF pattern encompasses the variability from all zonal wave numbers and does not align perfectly with the climatological wave-1 pattern (Figure 4.A.1), hence a weak wave event may still produce a polar vortex stretching (Figure 4.7.1). Additionally, the third and fourth EOF patterns feature a wave-2 structure (Figure 4.A.2), which may also have important implications as previous studies have found an important role of wave-2 anomalies in split SSWs (Charlton & Polvani, 2007; Nakagawa & Yamazaki, 2006). However, since their explained variances (11.6% and 9.4%) are much smaller than that of the leading EOF (37.6%), we focus on the leading EOF in this study.

4.2.3 ARs and Precipitation in Observations

To quantify the stratospheric impact on hydrological extremes, we analyze the composites of ARs and precipitation for stratospheric wave events. We use the AR detection algorithm based on column integrated water vapor transport (IVT) developed by (B. Guan & Waliser, 2015). IVT is calculated by vertically integrating the moisture fluxes at 1,000, 850, 700, and 500 hPa. AR conditions are identified when IVT exceeds the seasonally and regionally dependent 85th percentile of IVT magnitude, with additional criteria on their spatial coherence, IVT direction, length, and length-to-width ratio. ARs are detected in 6-hourly data, but only 12:00 UTC AR data is used to calculate AR frequency to maintain the same daily resolution as the rest of our analysis.

The AR frequency, defined as the percentage of days when the above AR conditions are met at a grid point, is computed for 1979–2018 in ERA5. We also employ the daily accumulated

precipitation estimate from Integrated Multi-satellitE Retrievals for GPM (IMERG; Huffman et al., 2014). The IMERG Final Run data covers the period from June 2000 to September 2021 with a spatial resolution of 1° × 1°. Because ARs and precipitation are available over shorter time spans, the AR composite is based on 52 out of 89 weak stratospheric wave events and 60 out of 93 strong wave events during 1979–2018, and the precipitation composite is based on 26 weak and 31 strong wave events during 2000–2021. As the result of fewer wave events, the composite analysis of weather extremes is averaged over a 15-day period before the wave event onset (i.e., days -15–0) or afterward (i.e., days 5–20), respectively.

4.2.4 Plumb Wave Activity Flux

The 3D Plumb wave activity flux is used to delineate planetary wave propagation. According to Plumb (1985), the Plumb flux is expressed as

$$\{F^{\lambda}, F^{\phi}, F^{z}\} = p\cos(\phi)\left\{v'^{2} - \frac{1}{fa\cos(\phi)}\frac{\partial(v'\Phi')}{\partial\lambda}, -u'v' + \frac{1}{fa\cos(\phi)}\frac{\partial(u'\Phi')}{\partial\lambda},\right.$$
$$\left.\frac{f}{\partial\tilde{T}/\partial z + \kappa\tilde{T}/H}\left[v'T' - \frac{1}{fa\cos(\phi)}\frac{\partial(T'\Phi')}{\partial\lambda}\right]\right\}$$

where λ is longitude, ϕ is latitude, z is height, and p is pressure. T is temperature, Φ is geopotential height, u is the zonal wind, and v is the meridional wind. f is the Coriolis parameter and a is Earth's radius. κ is the specific gas constant of dry air divided by the specific heat of dry air. $\tilde{T}$ is the domain-averaged temperature. H is the log-pressure scale height. Primes denote the deviations from zonal means.

4.3 Linking Extreme Stratospheric Wave Activity With Weather Extremes in Reanalysis

4.3.1 Linkage Between Stratospheric Wave Activity and Surface Extremes

We begin by characterizing the evolution of the stratospheric circulation with respect to extreme stratospheric wave events. Figure 4.7.1 shows the composites of anomalous and total geopotential heights at 10 hPa for strong and weak wave events in the ERA5 reanalysis. For weak wave events, an anomalous trough over North America and an anomalous ridge over Eurasia are developed before day 0 and persist for about 5 days before they start to decay (Figures 4.7.1a–1d). The total geopotential height field features a polar vortex being stretched toward North America from day 0 to day 5 (also see Figure 4.A.3). The height anomalies of strong wave events are largely opposite to those of weak wave events, with a NA ridge and a Eurasian trough (Figures 4.7.1e–1h). The total geopotential height field shows a polar vortex displaced toward Eurasia, as compared with the vortex stretching for weak wave events (also see Figure 4.A.3). Notably, the wave-1 component of weak wave events is out of phase with the wave-1 climatology, while the wave-1 pattern of strong wave events is in phase with the climatology (Figure 4.A.1). In other words, the climatological wave-1 pattern is weakened via destructive interference between transient and climatological wave-1 during weak wave events, in contrast to the constructive wave interference during strong wave events (K. L. Smith & Kushner, 2012).

Figure 4.7.2 examines the corresponding tropospheric circulation of extreme stratospheric wave events. Before and around the onset of weak stratospheric wave events, 500 hPa geopotential height composites indicate a strong ridge around Alaska and two troughs over eastern North America and Europe, respectively (Figures 4.7.2a and 2b). This observed precursor pattern, reminiscent of the Alaskan Ridge weather regime over the NA sector (Lee

et al., 2019; Vigaud et al., 2018), is similar to the tropospheric pattern associated with negative eddy heat flux events (see Figure 6 in Shaw & Perlwitz, 2013). It is worth noting that atmospheric blocking in this region has been recognized as a suppressor of upward wave propagation (e.g., Nishii et al., 2011). This convergence of findings highlights that these stratospheric events represent different aspects of the planetary wave-zonal flow interaction. From day 0 to day 10, this Alaskan ridge pattern evolves into a ridge over eastern North America and a trough over Siberia (Figure 4.7.2d). Note the dipole anomalies over the Atlantic from day 5 to day 10 project onto the negative phase of the NAO, which is opposite to the tropospheric pattern of negative eddy heat flux events (Shaw & Perlwitz, 2013).

The tropospheric circulation anomalies of strong stratospheric wave events are generally opposite to those of weak wave events. A trough occurs over Alaska and two ridges occur over eastern North America and Europe before and around the onset (Figures 4.7.2e and 2f). The precursor pattern of an Alaskan trough resembles the Pacific Trough weather regime over the NA sector (Lee et al., 2019; Vigaud et al., 2018). This is also consistent with the finding that a low-pressure anomaly over the North Pacific tends to enhance upward wave propagation, which serves as a precursor of SSWs (e.g., Garfinkel et al., 2010; Woollings et al., 2010). Around 10 days after the onset, a trough develops over Greenland and eastern North America, extending across the NA continent (Figure 4.7.2h). The dipole anomalies over the Atlantic strongly project onto positive NAO. The evolution of the tropospheric circulation during strong wave events resembles the transition associated with planetary wave reflection events overall, but with no Alaskan ridge anomalies at positive lags (Messori et al., 2022). While the wave reflection events (Messori et al., 2022) are defined by the 100 hPa variability that may consist of both tropospheric and stratospheric variabilities, the stratospheric wave events defined here are based on 10 hPa and thus represent stratospheric variability.

Of particular interest is the linkage of stratospheric wave events with surface circulation and extremes. Figures 4.7.3a and 3d compare the composites of SAT and sea level pressure (SLP) anomalies before and after the onset of extreme stratospheric wave events. During days -15–0 of weak wave events, an anomalous positive SLP center over Alaska favors warm anomalies around the Bering Strait and cold anomalies over North America (Figure 4.7.3a). The NA cold anomalies are similar to the surface temperature signature observed during polar vortex stretching events (Cohen et al., 2021) and negative eddy heat flux events (Shaw et al., 2014). From day 5 to day 20, warm anomalies occur over eastern Canada and cold anomalies extend across northern Eurasia, consistent with the 500 hPa circulation patterns (Figures 4.7.2a–2d) and the SLP anomalies over the Atlantic that project onto negative NAO. In contrast, strong stratospheric wave events are preceded by cold anomalies around the Bering Strait and warm anomalies over North America, which are favored by deepened Aleutian Low before and near the onset (Figure 4.7.3d). We note that a deepened Aleutian Low has been long recognized as a precursor for a weak stratospheric polar vortex via constructive interference with the climatological wave-1 (Garfinkel et al., 2010; Nishii et al., 2011). For the period afterward, strong wave events are linked to extensive cold anomalies over North America, consistent with the anomalous trough at 500 hPa (Figures 4.7.2e–2h). The dipole in SLP anomalies over the Atlantic projects onto the positive phase of the NAO. This transition from NA warm anomalies to cold anomalies during strong wave events agrees with the lag regression analysis in Ding et al. (2022) and also the rapid temperature decrease over North America associated with wave reflection events in Messori et al. (2022). Although the magnitude of cold anomalies following strong stratospheric wave events is weaker than that of cold anomalies before or near the onset of weak wave events, strong wave events are

particularly noteworthy because of the potential predictability for NA cold anomalies on subseasonal timescales.

Having illustrated the association between stratospheric wave activity and mean tropospheric conditions, we next discuss whether a similar linkage exists for daily surface temperature extremes. The impact of extreme stratospheric wave events on surface temperature extremes is quantified by the risk ratio of extreme cold and warm days. We define extreme cold/warm days when the SAT at a grid point lies at least 1.5 standard deviations (SD) below/above its climatology. The risk ratio of temperature extremes is measured as the ratio between the probability of temperature extremes associated with wave events and the probability of temperature extremes during all the winter days, with values larger than one indicating increased risks. From day −15 to day 0, weak wave events are associated with ~60% higher risk of cold extremes across North America and over 75% higher risk of warm extremes over the northeast Pacific (Figures 4.7.3b and 3c). The increased risk of warm extremes persists with a smaller magnitude over the northeast Pacific during days 5–20, but the risk of cold extremes is elevated over Europe. For strong wave events, the risk of cold extremes increases over the northeast Pacific before and near the event onset, but the risk of warm extremes is enhanced over North America (Figures 4.7.3e and 3f). From day 5 to day 20, strong wave events enhance the risk of cold extremes by ~30% across much of Canada and the Midwest United States, while the risk of warm extremes is enhanced over northern Europe. The risk ratio patterns of temperature extremes generally agree with the anomalous SAT composites (Figures 4.7.3a and 3d), suggesting that changes in temperature extremes may be explained by changes in mean temperature associated with stratospheric wave events.

We further present anomalous AR frequency and anomalous precipitation before and after the extreme wave events (Figure 4.7.4). During days -15–0, weak wave events are preceded by reduced AR frequency along the center of the Pacific AR maximum region, accompanied by increased AR frequency on the north and south sides (Figure 4.7.4b). This tripole anomalous AR pattern resembles the second mode of interannual winter AR variability over the North Pacific identified in W. Ma and Chen (2022). This pattern is also consistent with the SLP anomalies of a strong positive center over the northeast Pacific and a secondary negative center to the south (Figure 4.7.4a). Correspondingly, precipitation decreases significantly along the west coast from 40°N to 60°N (Figure 4.7.4c), although no evident positive anomalies are observed on the northside possibly due to limited data coverage in IMERG north of 60°N. From day 5 to day 20, the AR anomalies over the Pacific weaken and shift slightly southwards. ARs become much less likely across the British Isles and Scandinavia, accompanied by reduced precipitation. This frequency decrease is likely attributed to the surface cooling and positive SLP anomaly over the north Atlantic (Figure 4.7.4a). Negative anomalies in temperature reduce the atmospheric moisture as governed by the Clausius-Clapeyron relation, resulting in reduced AR frequency and precipitation. Additionally, the positive SLP anomaly generates easterly wind anomalies and weakens onshore moisture transport along the Europe west coast, which also contributes to a reduction in AR frequency and precipitation.

In comparison with weak wave events, the anomalous patterns of strong wave events are generally of the opposite sign. Strong wave events are preceded by increased AR frequency over the Pacific AR maximum region, with reduced AR frequency on the north and south sides during days -15–0 (Figure 4.7.4e), consistent with the anomalous low-pressure center over the northeast Pacific (Figure 4.7.4d). This corresponds to the increase in precipitation

along the west coast from 40°N to 60°N (Figure 4.7.4f). During days 5–20, ARs over the Atlantic are shifted poleward relative to the climatology, with increased frequency northside and decreased frequency southside of the AR maximum. Accordingly, precipitation increases over the British Isles and Scandinavia and decreases around the Iberian Peninsula (Figure 4.7.4f), consistent with a northward-shifted jet during positive NAO (Figure 4.7.4d). The anomalous AR patterns associated with the North Atlantic jet are largely consistent with the patterns of AR variability at seasonal or longer timescales (Baek et al., 2023; Lee et al., 2022; W. Ma & Chen, 2022).

4.3.2 Vertical Wave Structure During Extreme Stratospheric Wave Events

How is stratospheric wave activity connected to tropospheric variability? We examine the vertical structure of planetary wave coupling between the stratosphere and troposphere during extreme wave events in ERA5. Figure 4.7.5 displays the zonally asymmetric component of geopotential height anomalies and Plumb flux anomalies averaged over 50°–70°N during the life cycle of extreme stratospheric wave events. We note that the westward tilt of geopotential height anomalies with increasing altitude implies positive transient eddy heat fluxes that correspond to upward-propagating planetary waves, and that the Plumb fluxes include both transient eddy fluxes and the interference between transient and climatological planetary waves. For weak wave events, the westward tilt of the wave-1 phase line prevails through the life cycle, consistent with the wave-1 structure in the stratosphere around days -5–5 in Figure 4.7.1. After day 0, the tropospheric trough over North America quickly weakens and moves eastwards, leading to the termination of cold air advection and associated cold anomalies (Figure 4.7.3). Interestingly, the Plumb flux anomalies indicate

downward wave activity fluxes over the eastern hemisphere from day 0 to day 5, due to the destructive interference between transient and climatological planetary waves.

Strong wave events show significant upward and eastward Plumb flux anomalies over Siberia, leading to the intensification of an anomalous stratospheric ridge over North America from day −5 to day 5 (Figures 4.7.5e–5g). As the stratospheric ridge intensifies and persists, the initial westward tilt of geopotential height anomalies transitions to an eastward tilt after day 0, indicating anomalous downward propagation of transient waves. This change in wave phase tilt is also evident for the wave-1 component alone, displayed in thick black lines. After the onset, the anomalous tropospheric ridge retrogrades westwards from the NA continent to the Pacific, yielding an anomalous trough over eastern North America around days 5–10 (Figures 4.7.5g and 5h). This trough evolves in association with the SAT anomalies over North America (Figures 4.7.2 and 3). Moreover, the establishment of the tropospheric trough coincides with the downward Plumb flux anomalies over North America around days 0–10. These downward Plumb flux anomalies may be interpreted as local vertical wave reflection, although the zonal mean wave-1 eddy heat flux at 100 hPa remains positive throughout the strong wave events (Figure 4.A.4).

As previous studies suggest that the negative vertical zonal wind shear in the upper stratosphere may cause the vertical reflection of planetary waves (Perlwitz & Harnik, 2003), Figures 4.7.6a and 6b display the zonal wind anomalies averaged over 60°–80°N for extreme wave events in ERA5. Weak wave events show weakly positive zonal wind anomalies in the stratosphere from day 0 to day 10, which can be attributed to the weakening of the climatological wave-1 (Figures 4.7.1a–1d) and the reduced upward Plumb fluxes (Figure 4.7.5). And the negative zonal wind anomaly in the troposphere after day 0 coincides with

the negative phase of the NAO (Figures 4.7.2 and 3). The zonal wind speed averaged around the weak wave event onset (blue line) increases with altitude in the stratosphere, similar to the climatological wind profile (Figure 4.7.6c). Strong wave events, however, feature a robust downward propagation of zonal wind anomalies (Figure 4.7.6b). A strong wind deceleration is observed around day 0 in the stratosphere, followed by positive anomalies in the troposphere which is consistent with positive NAO (Figures 4.7.2 and 3). More importantly, the stratospheric zonal wind speed (red line) decreases with altitude around the strong wave event onset (Figure 4.7.6c). This negative vertical zonal wind shear may indicate a vertical reflective surface for upward planetary wave propagation (Perlwitz & Harnik, 2003). Although the zonal mean eddy heat fluxes are positive, the presence of a vertical reflective surface and regionally downward Plumb fluxes (Figure 4.7.5 and 4.A.5) might hint at the role of local planetary wave reflection during strong wave events.

To summarize, the above analysis demonstrates an observed linkage between extreme stratospheric wave events and tropospheric temperature and precipitation. The tropospheric circulation patterns before and around the onset of these wave events align closely with known precursor patterns that either suppress or enhance upward planetary wave propagation, depending on the interference between transient waves and climatological waves (Garfinkel et al., 2010; Nishii et al., 2011; Woollings et al., 2010). It is worth noting that the surface precursors of weak wave events exhibit similarities to the surface signals associated with wave reflection events (Cohen et al., 2021; Shaw et al., 2014). The strong stratospheric wave events are followed by an elevated risk of NA cold extremes and north-shifted ARs over the Atlantic, resulting in precipitation anomalies consistent with a northward-shifted jet during positive NAO. The analysis of the vertical structure corroborates the two-way coupling during these stratospheric wave events. These results

suggest that extreme stratospheric wave activity has important implications for the predictability of tropospheric weather extremes on subseasonal timescales, warranting further evaluations of extreme stratospheric events in CMIP6 models.

4.4 Coupling Between Stratospheric Wave Activity and the Troposphere in CMIP6 Models

Figure 4.7.7 compares the temporal evolution of circulation and surface conditions associated with extreme stratospheric wave events in CMIP6 models. The time series of regionally averaged 10 hPa geopotential height anomalies over northern North America (60°–90°N, 60°W–180°) is compared with that of 500 hPa geopotential height anomalies over eastern North America (40°–70°N, 30°–130°W). The regions are selected based on the dominant circulation features in the stratosphere and troposphere (Figures 4.7.1 and 2). For weak wave events, an anomalous stratospheric trough over northern North America is developed and reaches a peak around day 2 (Figure 4.7.7a). This is preceded by an anomalous tropospheric trough that matures over eastern North America during days -10–0 and subsequently evolves into an anomalous ridge during days 5–20 (Figure 4.7.7c). The evolution of strong wave events is generally opposite to that of weak wave events (Figures 4.7.7b and 7d), except that the tropospheric trough after the event onset is more persistent. The CMIP6 multi-model ensemble (MME) mean (red lines) agrees very well with ERA5 (black lines), implying that CMIP6 models can largely capture the physical processes at play for stratosphere-troposphere coupling of extreme stratospheric wave activity.

We next show the evolution of SAT anomalies associated with extreme wave events. We define NA SAT as the regional average of SAT over land regions within 40°–70°N, 70°–130°W, corresponding to the area of large SAT signals (Figures 4.7.3a and 3d). The evolution of NA

SAT is very consistent with the regional circulation evolution (Figures 4.7.7c–7f), indicating that these NA SAT anomalies are likely caused by anomalous circulation. Weak wave events exhibit strong cold anomalies over North America before day 0, but these signals weaken rapidly after day 0 (Figure 4.7.7e). Strong wave events, in contrast, show a swing from warm anomalies around day −5 to cold anomalies around day 10 (Figure 4.7.7f), consistent with the temperature composite patterns in Figure 4.7.3d. The CMIP6 model results, albeit the large spread across models, agree with ERA5 on the swing from warm anomalies to cold anomalies in association with strong wave events, supporting the potential predictability for cold spells from strong stratospheric wave activity. In addition, we note that the inter-member spread within a single model (the 9-member CESM2 ensemble) (green shading) is smaller compared to the intermodel spread across CMIP6 models (gray lines), indicating that while internal atmospheric variability plays a role, systematic intermodel differences are an important contributor to the observed spread of the stratosphere-troposphere coupling of extreme stratospheric wave events.

We will hereafter focus on strong stratospheric wave events because they potentially benefit the subseasonal forecast of extreme cold events over North America. We notice a large uncertainty in the wave event evolution across CMIP6 models (Figure 4.7.7). Since the previous analysis has identified a linkage between the stratospheric ridge and tropospheric trough over North America during strong wave events, a question arises: can the intermodel differences in stratospheric waves help explain different tropospheric responses?

To quantify the connection between stratospheric wave representation and its tropospheric fingerprints during strong stratospheric wave events, Figure 4.7.8a presents the scatterplot of the stratospheric ridge anomaly during days -5–5 versus the tropospheric trough anomaly

during days 5–20 across CMIP6 models. These time periods are selected based on the timing of the largest signals in Figure 4.7.7. There is a significant linear correlation ($r = -0.52$) between the stratospheric ridge and the tropospheric trough. This intermodel relation supports the proposed mechanism that the model representation of the stratospheric ridge over northern North America influences the tropospheric responses to strong wave events. The ERA5 result (black dot) lies within the intermodel spread, indicating that the modeled stratosphere-troposphere coupling during strong wave events is comparable to the reanalysis. The intermodel relation identified here suggests that the stratospheric wave structure can serve as a performance metric for assessing the stratosphere-troposphere coupling of strong wave events in models. Moreover, Figure 4.7.8b shows the scatterplot of the tropospheric trough anomaly versus NA SAT. The strong linear correlation ($r = 0.68$) between them confirms that the trough over North America is closely linked to the surface cold anomalies. It is thus tempting to ask whether a linear relation may also exist between the stratospheric ridge and NA SAT. However, Figure 4.7.8c suggests otherwise. The weak correlation between the stratospheric ridge and NA SAT indicates that the intermodel spreads of their correlations with the tropospheric trough largely cancel each other and result in a very small net effect.

It is worth noting that internal variability (red error bars) accounts for less than half of the intermodel spread for the stratospheric ridge and tropospheric trough associated with strong wave events, while the internal variability in the NA SAT may be comparable to the intermodel spread. More quantitatively, the variance of the stratospheric ridge in the CESM2 ensemble is 17.4% of the entire CMIP6 ensemble variance. And the variance of the tropospheric trough in the CESM2 ensemble accounts for 32.8% of the entire ensemble

variance, while that ratio for NA SAT is 134.1%. The different fractions of internal variability may also help explain the small correlation between the stratospheric ridge and NA SAT.

4.5 Comparison With Eddy Heat Flux Events and Planetary Wave Reflection Events

In light of the similarity between the wave events discussed here and other extreme stratospheric events in the literature, we have analyzed whether the strong or weak stratospheric wave events overlap with eddy heat flux events (Dunn-Sigouin & Shaw, 2015) or planetary wave reflection events (Messori et al., 2022) in ERA5 (Figures 4.7.9a and 9b). According to Dunn-Sigouin and Shaw (2015), positive/negative eddy heat flux events are identified when the 50 hPa wave-1 eddy heat flux (60°–90°N) crosses the 95th/5th percentile from January to March. Day 0 is defined as the day of maximum or minimum heat flux. And events must be separated by at least 15 days. For the planetary wave reflection events, we use those dates from Messori et al. (2022).

Using a 15-day window centered at the onset of wave events defined in this study, we find that negative eddy heat flux events only occur in proximity to 13 of the 58 weak wave events during 1950–2021 (Figure 4.7.9a), and that positive heat flux events occur around 28 of the 67 strong wave events (Figure 4.7.9b). Note the numbers of stratospheric wave events are different from those in the previous sections because of the different time periods considered (November to March vs. January to March), which ensures a fair comparison across different stratospheric event types. And the planetary wave reflection events occur around 13 of the 45 strong wave events within 15 days around their onset during 1980–2021 based on the available dates of reflection events (Figure 4.7.9b). While all these stratospheric events feature significant NA temperature anomalies (Figures 4.A.6 and 4.A.7), weak wave events exhibit a stronger cold anomaly than negative eddy heat flux events (Figure 4.7.9c). Strong

wave events show an overall similar NA SAT fingerprint as positive eddy heat flux events and planetary wave reflection events, with a transition from warm anomalies to cold anomalies (Figure 4.7.9d). Notably, strong wave events feature the most persistent cold anomalies that persist over 25 days after the event onset.

Additionally, in comparison to the dates of SSWs from the SSW Compendium data set (Butler et al., 2017), while some strong stratospheric wave events are followed by SSWs, many do not (Figure 4.A.8), suggesting strong stratospheric wave activity does not necessarily lead to SSWs. These findings align with previous studies which have found that strong wave flux may not be sufficient on its own to trigger an SSW (Cámara et al., 2017; Reichler & Jucker, 2022).

4.6 Conclusion

In this paper, we investigate the vertical coupling of extreme stratospheric wave activity in ERA5 and CMIP6 models. Extreme stratospheric wave events are identified based on the EOF of the zonally asymmetric component of 10 hPa geopotential height. Weak wave events feature a horizontally stretched polar vortex in the stratosphere associated with the weakening of planetary wave-1, while strong wave events are characterized by a polar vortex displaced toward Eurasia accompanied by the amplification of wave-1 (Figure 4.7.1). In the troposphere, weak wave events are preceded by an anomalous NA trough and an Alaskan ridge, inducing intense surface cold anomalies over North America (Figures 4.7.2 and 3). Strong wave events, in contrast, are preceded by intensified Aleutian low with NA warming, transitioning into an anomalous NA trough with NA cooling and positive NAO around 10 days later. Here we highlight the lagged relation between strong stratospheric wave activity and NA surface cooling, with implications for subseasonal prediction of the NA cold events.

W. Guan et al. (2020) suggest a similar role of stratosphere-troposphere coupling in a subseasonal NA temperature variability mode. The subseasonal swing in temperature also resembles the surface fingerprints of the stratosphere-troposphere oscillation identified by Shen et al. (2022). These are also in line with other recent studies that suggest a stratospheric source of subseasonal predictability for NA surface temperature variability (e.g., Ding et al., 2022, Ding, Chen, Zhang, et al., 2023; Messori et al., 2022).

We have also documented the tropospheric extremes associated with stratospheric wave activity (Figures 4.7.3 and 4). During days -15–0 of weak wave events, we find ~60% higher cold extreme risk over North America and over 75% higher warm extreme risk over the northeast Pacific, with reduced AR frequency and less precipitation over the west coast of the United States. Following the onset of weak wave events, increased cold extreme risk and decreased AR frequency are observed over Europe. On the other hand, strong wave events exhibit higher warm extreme risks over North America and higher cold extreme risks over the northeast Pacific during days -15–0, with more frequent AR events and increased precipitation observed along the west coast of the United States. These are in contrast to days 5–20 after the onset, during which strong wave events are associated with a significantly higher risk of cold extremes over North America and a northward shift of AR frequency and precipitation over the Atlantic. Similar rainfall anomalies over the west coast of the United States are reported when the stratospheric polar vortex over Eurasia is intensified and weakened, respectively (Liang et al., 2022). These analyses demonstrate a robust linkage of stratospheric wave activity to temperature and hydrological extremes in the troposphere.

We refer to the vertical structure of planetary waves to understand the linkage between stratospheric wave activity and tropospheric conditions (Figure 4.7.5). Weak wave events feature the development and decay of a Pacific ridge and a NA trough extending from the troposphere to the stratosphere. This wave-1 structure tilts westwards with altitude, indicating upward-propagating transient waves that interfere destructively with the climatological planetary wave in the stratosphere. Strong wave events, on the other hand, feature a persistent stratospheric ridge over North America. As the vertical wave phase shifts from a westward tilt before the event onset to an eastward tilt afterward, an anomalous trough develops over eastern North America in the troposphere. We also observe a reversal in the vertical shear of stratospheric zonal winds around the onset of strong wave events (Figure 4.7.6), suggesting a possible vertical reflective surface that may cause such a vertical phase shift (Perlwitz & Harnik, 2003). The shift in vertical wave phase tilt and the reflective surface may combine to indicate that planetary waves are regionally reflected during strong wave events, but additional analysis is required due to the observed positive zonal mean eddy heat flux.

The stratosphere-troposphere coupling of extreme stratospheric wave events is further assessed in CMIP6 models. We explore the linkage between the stratospheric representation and tropospheric signals across individual models, finding a linear relationship between the strength of the stratospheric ridge and the strength of the following tropospheric trough over North America during strong stratospheric wave events (Figure 4.7.8a). This result suggests that the representation of stratospheric wave structure can serve as a metric to measure the vertical wave coupling of strong wave events. Future studies may wish to connect the representation of extreme wave events to certain aspects of model configurations, and if these configurations were to be refined, a better simulation of stratospheric or tropospheric

variability may be expected from the improved vertical wave coupling. Finally, predictability studies may also investigate to what extent strong stratospheric wave events would improve weather forecasts on subseasonal timescales.

Acknowledgments. We thank three anonymous reviewers for their constructive comments that greatly improved the manuscript. We acknowledge the WCRP Working Group on Coupled Modeling which is responsible for the CMIP. We also acknowledge high-performance computing support from Cheyenne (https://doi.org/10.5065/ D6RX99HX) provided by NCAR's Computational and Information Systems Laboratory, sponsored by the National Science Foundation. G.C. is supported by the U.S. NSF grant AGS-1832842 and AGS-2232581 and NASA Grant 80NSSC21K1522. W.M. acknowledges support by the U.S. Department of Energy (DOE), Office of Science, Office of Biological and Environmental Research, Regional and Global Model Analysis program area. The Pacific Northwest National Laboratory (PNNL) is operated for DOE by Battelle Memorial Institute under contract DE-AC05-76RLO1830.

4.7 Figures

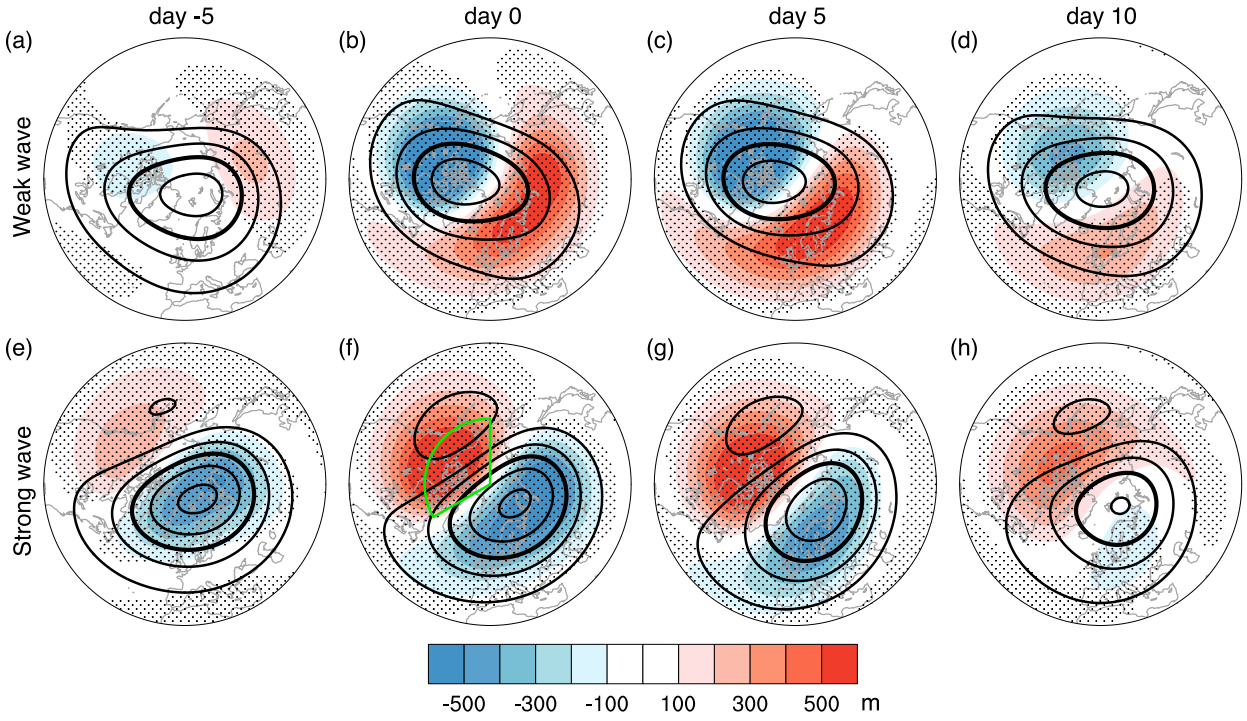

Figure 4.7.1: Composites of geopotential height at 10 hPa for weak (top) and strong (bottom) stratospheric wave events in the ERA5 reanalysis. (a and e) day -5, (b and f) day 0, (c and g) day 5, and (d and h) day 10. Shading denotes anomalies, and contours denote absolute values (contour intervals: 500 m) with 29000 m contour emboldened. The time evolution is smoothed by a 5-day running average. Stippling represents the regions where the anomalies are significant at the 95% confidence level based on the Student's *t*-test. The green box (60°–90°N, 60°W–180°) in (f) indicates the region where stratospheric ridge anomalies are calculated.

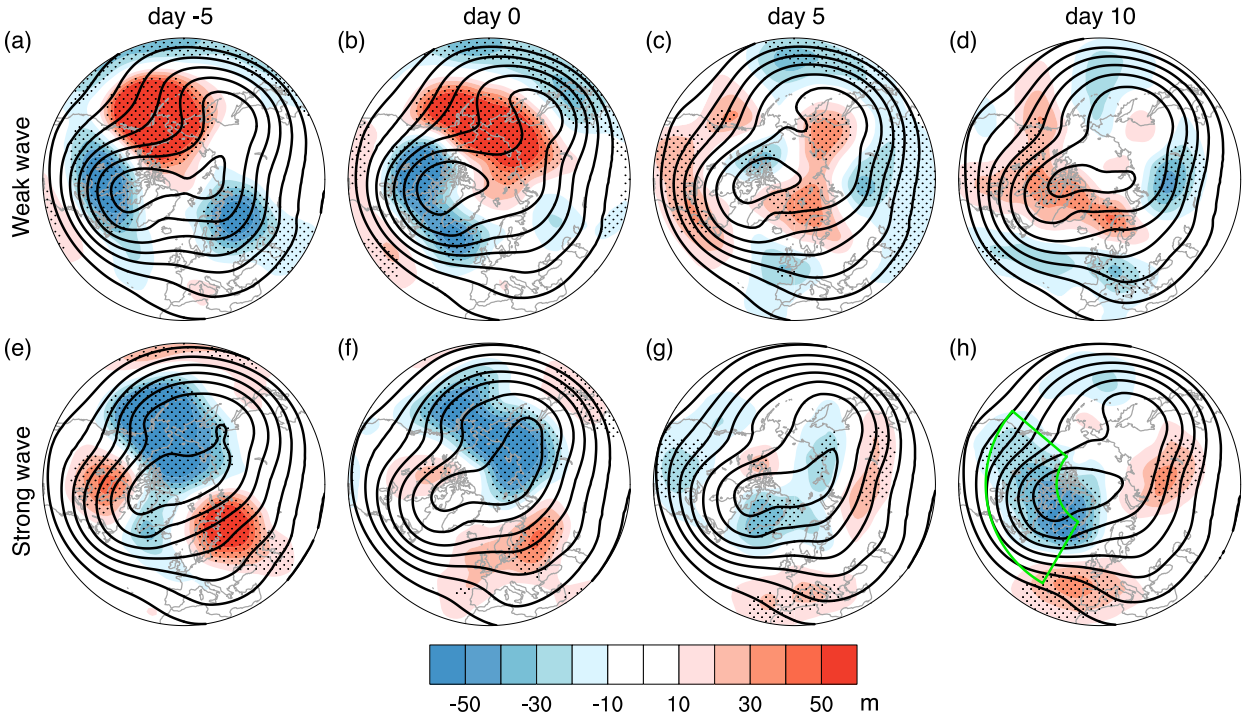

Figure 4.7.2: Composites of geopotential height at 500 hPa for weak (top) and strong (bottom) stratospheric wave events in ERA5 reanalysis. As in Figure 4.7.1, but for 500 hPa geopotential height. Shading denotes anomalies, and contours denote absolute values (contour intervals: 100 m). The green box (40°–70°N, 30°–130°W) in (h) indicates the region where tropospheric trough anomalies are calculated.

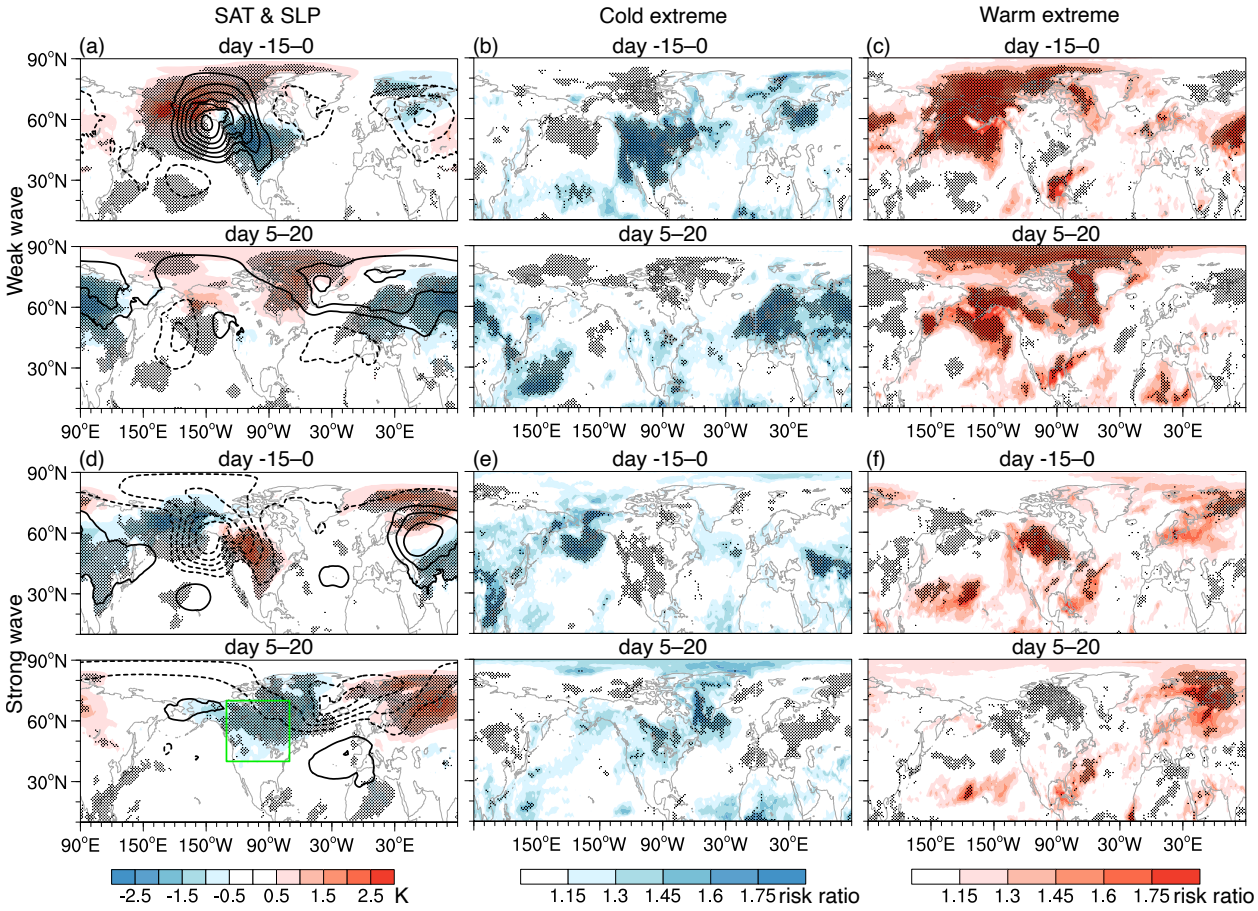

Figure 4.7.3: Composites of surface anomalies and SAT extremes for weak (top) and strong (bottom) stratospheric wave events in ERA5. (a and d) SAT anomalies in shading and SLP anomalies in contours (contour intervals: 1 hPa) during days -15–0 and during days 5–20. (b and e) the risk ratio of cold extremes during days -15–0 and during days 5–20. (c and f) the risk ratio of warm extremes during days -15–0 and during days 5–20. The risk ratio of cold (warm) extremes is defined as the probability of cold (warm) extreme days (SAT anomalies exceed 1.5 SD) during the period of interest divided by the probability of cold (warm) extreme days in all the winter days. Stippling represents the regions significant at the 95% confidence level based on the Student's *t*-test. The green box (40°–70°N, 70°–130°W) in (d) indicates the region where NA SAT anomalies are calculated.

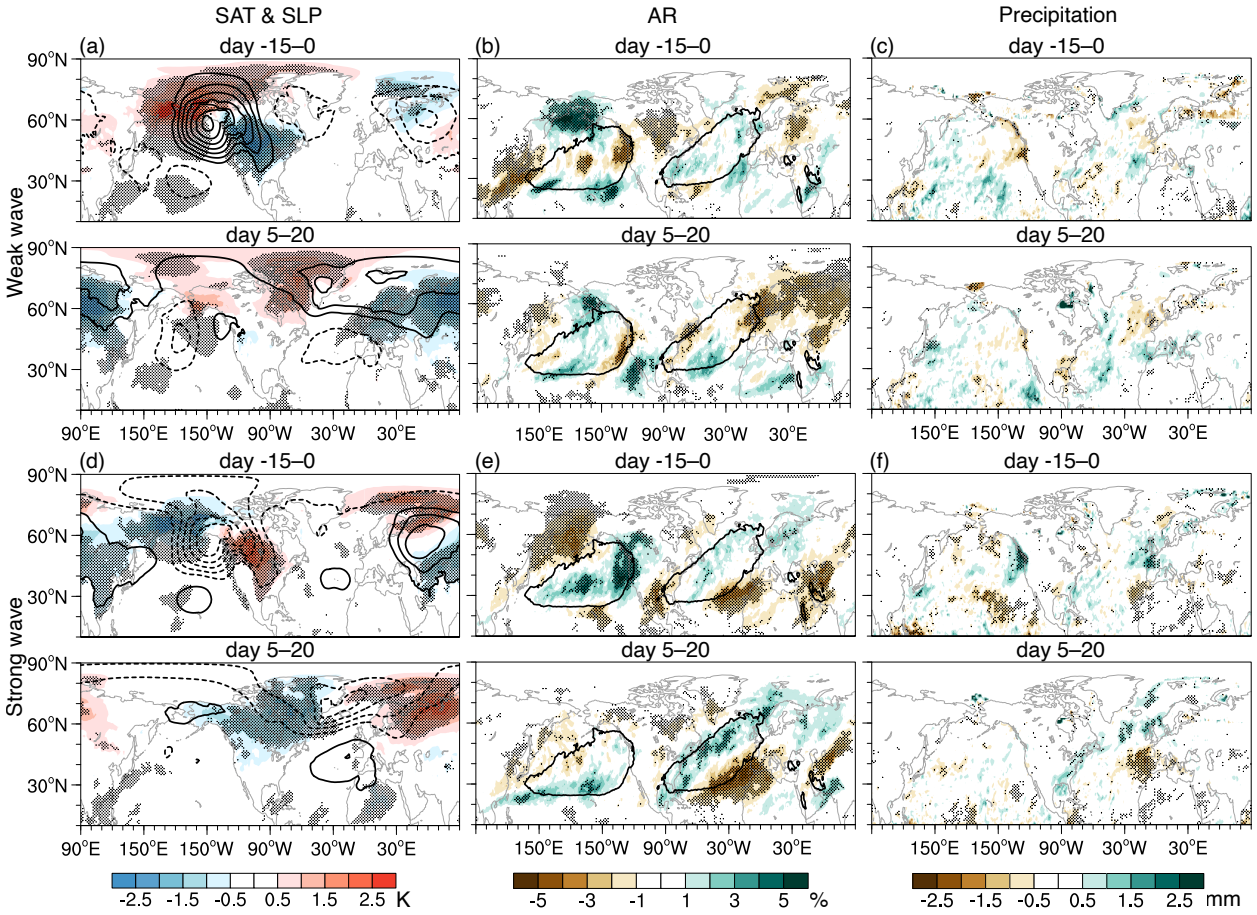

Figure 4.7.4: Composites of AR and precipitation anomalies for weak (top) and strong (bottom) stratospheric wave events in ERA5. (a and d) same as Figures 4.7.3a and 3d. (b and e) AR frequency anomalies during days -15–0 and during days 5–20. (c and f) precipitation anomalies during days -15–0 and during days 5–20. Contours in (b and e) denote regions where the climatological AR frequency exceeds 10%. Stippling represents the regions significant at the 95% confidence level based on the Student's *t*-test.

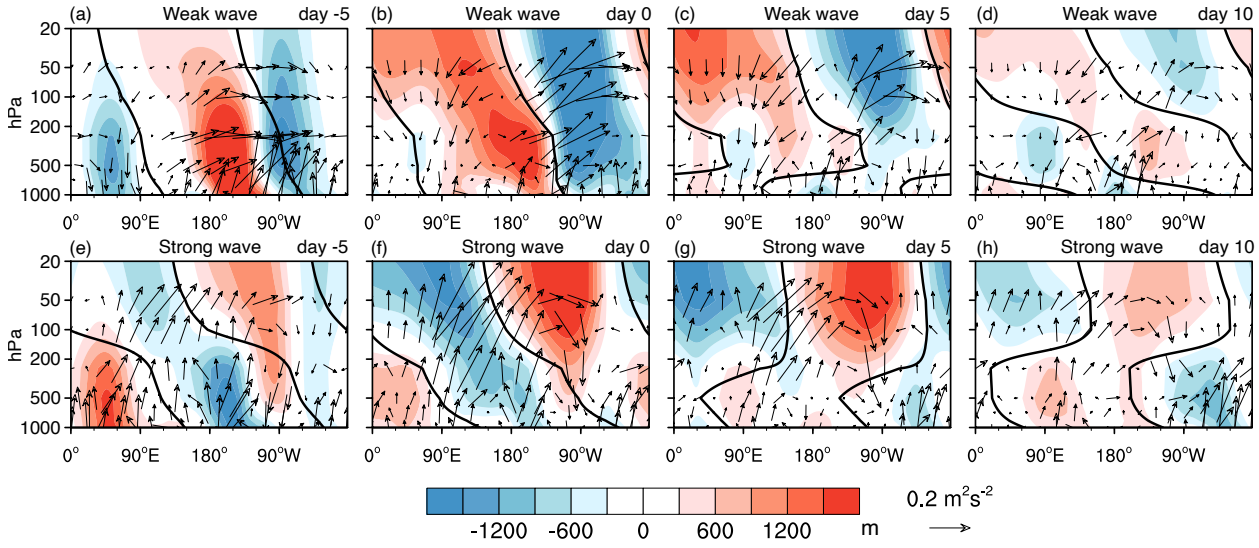

Figure 4.7.5: Vertical wave coupling during weak (top) and strong (bottom) wave events in ERA5. (a–d) composites of the zonally asymmetric component of anomalous geopotential height (shading) and the vertical and zonal components of anomalous Plumb wave activity flux (vector) averaged over 50°–70°N as a function of longitude and pressure on day -5, 0, 5 and 10 for weak wave events. (e–h) as in (a–d), but for strong wave events. Black lines are zero contours of the wave-1 component of anomalous geopotential height, indicating the phase tilt of wave-1. The time evolution is smoothed by a 5-day running average. To account for the smaller air density with decreasing pressure, the magnitude of the Plumb flux is scaled by $(1000/p)^{1/2}$, and geopotential height is scaled by $(p/1000)^{1/2}$, where p is pressure. The vertical component of the Plumb flux is also scaled by a factor of 200. See Figure 4.A.5 for the total (zonally asymmetric + zonal mean) field of anomalous geopotential height and absolute (anomalous + climatological) Plumb flux.

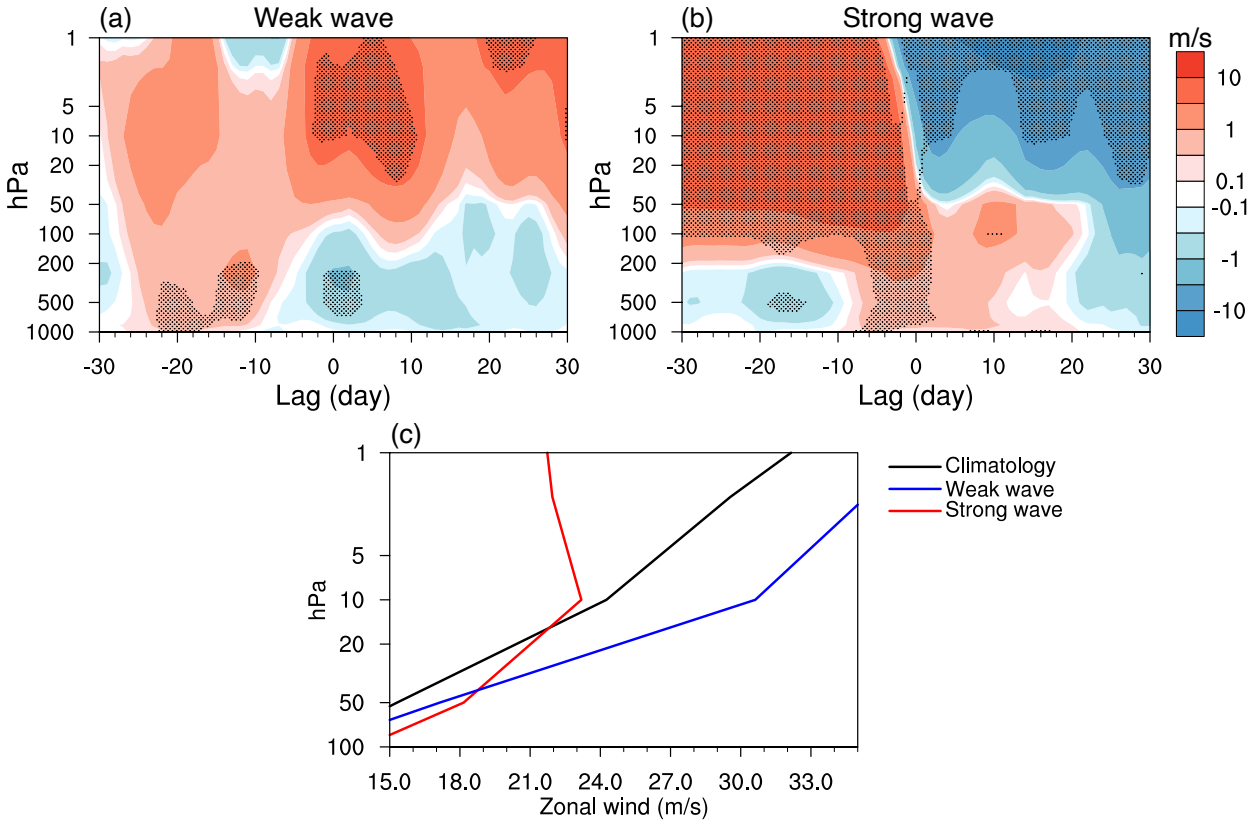

Figure 4.7.6: Zonally averaged high-latitude zonal wind for weak and strong wave events in ERA5. (a) zonal wind anomalies averaged over 60°–80°N during weak wave events. (b) zonal wind anomalies during strong wave events. A 5-day running average is applied. Stippling represents the regions where the anomalies are significant at the 95% confidence level based on the Student's *t*-test. (c) absolute (anomalous + climatological) zonal wind profiles in the stratosphere averaged from day -2 to day 2.

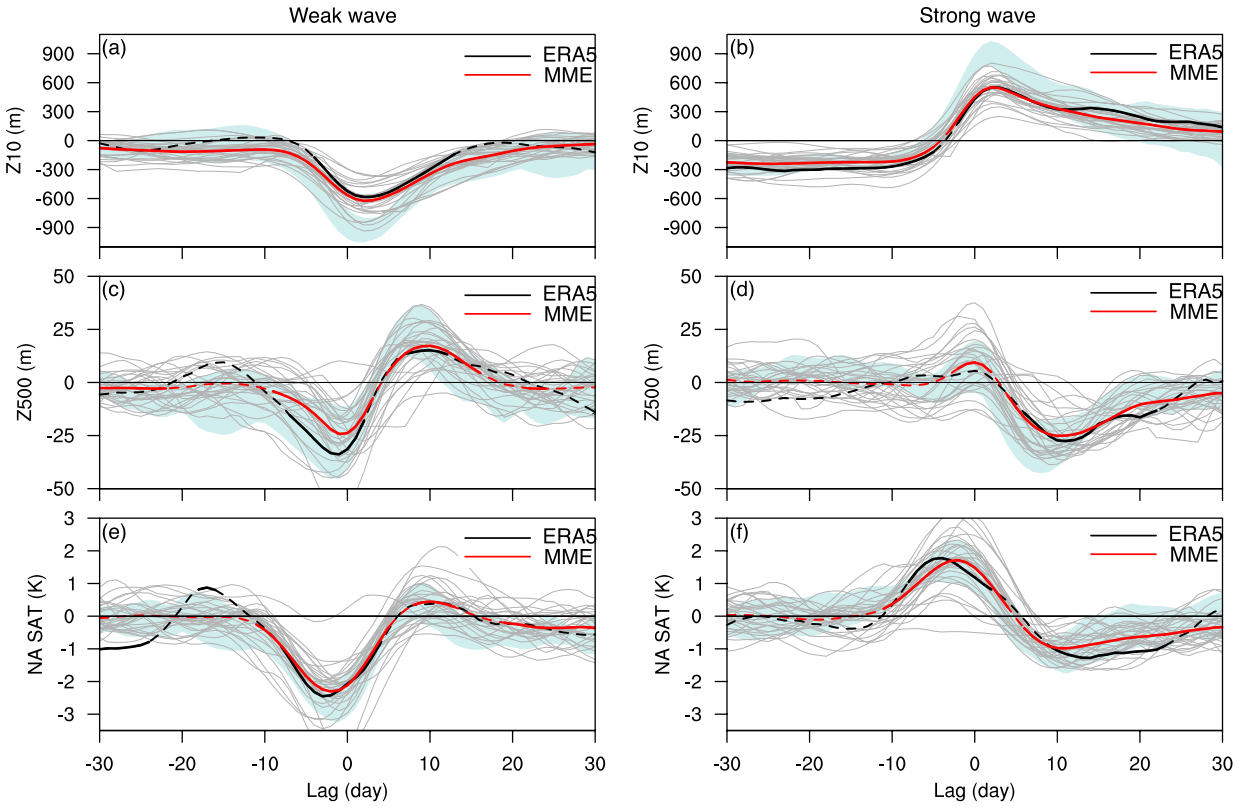

Figure 4.7.7: Evolution of circulation and NA SAT anomalies associated with weak (left) and strong (right) wave events in CMIP6 models. (a–b) 10 hPa geopotential height anomalies averaged over northern North America (60°–90°N, 60°W–180°). (c–d) 500 hPa geopotential height anomalies averaged over eastern North America (40°–70°N, 30°–130°W). (e–f) NA SAT anomalies averaged over land regions (40°–70°N, 70°–130°W). ERA5 is denoted by black lines, the CMIP6 multi-model ensemble (MME) mean is in red, and individual models are in light gray. Green shadings show the range across the 9-member CESM2 ensemble. The time evolution is smoothed by a 5-day running average. Solid parts of the lines for ERA5 and CMIP6 MME represent the anomalies significant at the 95% confidence level based on the Student's *t*-test.

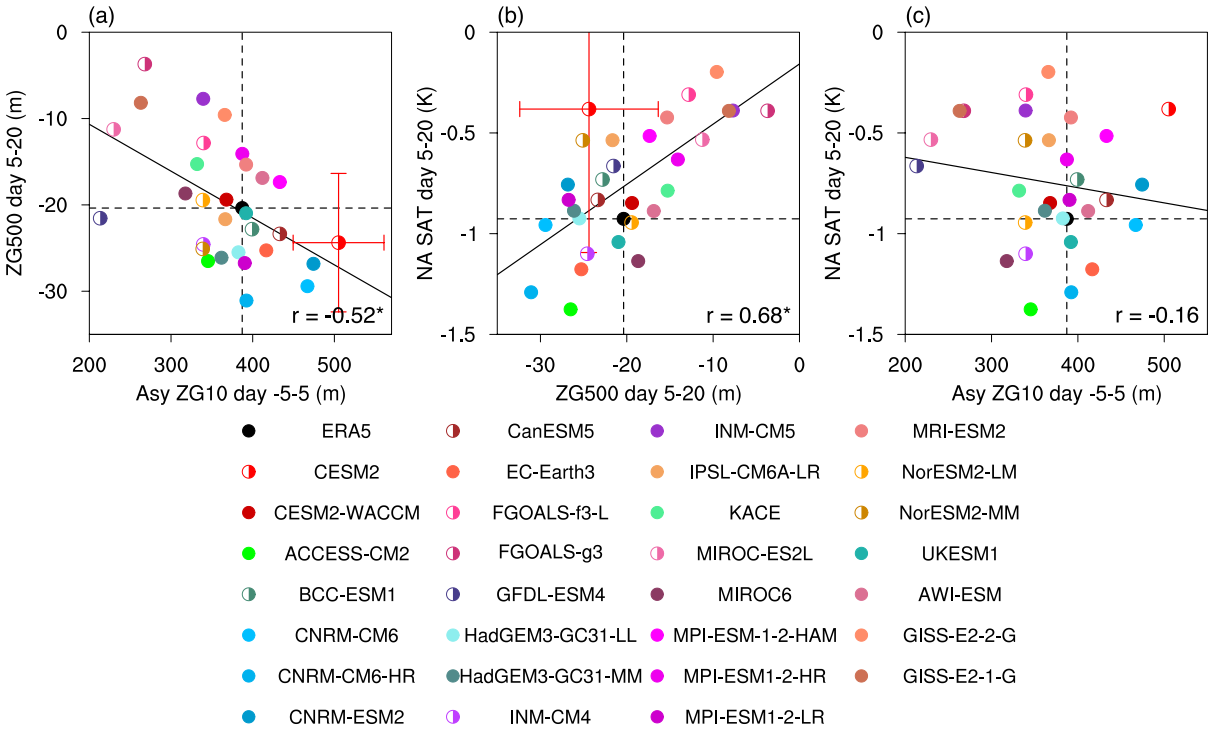

Figure 4.7.8: Intermodel spread of the relationship between stratospheric and tropospheric indices during strong wave events in CMIP6 models. (a) 10 hPa NA ridge during days -5–5 versus 500 hPa NA trough during days 5–20. (b) 500 hPa NA trough versus NA SAT during days 5–20. (c) 10 hPa NA ridge during days -5–5 versus NA SAT during days 5–20. 10 hPa NA ridge is defined by the asymmetric component of 10 hPa geopotential height anomalies over the northern NA region of 60°–90°N, 60°W–180°. 500 hPa NA trough is defined by 500 hPa geopotential height anomalies over the eastern NA region of 40°–70°N, 30°–130°W. Filled dots denote high-top models and half-filled dots indicate low-top models. The black lines show linear regressions for CMIP6 models, with correlation coefficients given in the legend. The red error bars show the ±2 SD in the 9-member CESM2 ensemble. Asterisks denote coefficients significant at the 95% confidence level based on the Student's *t*-test.

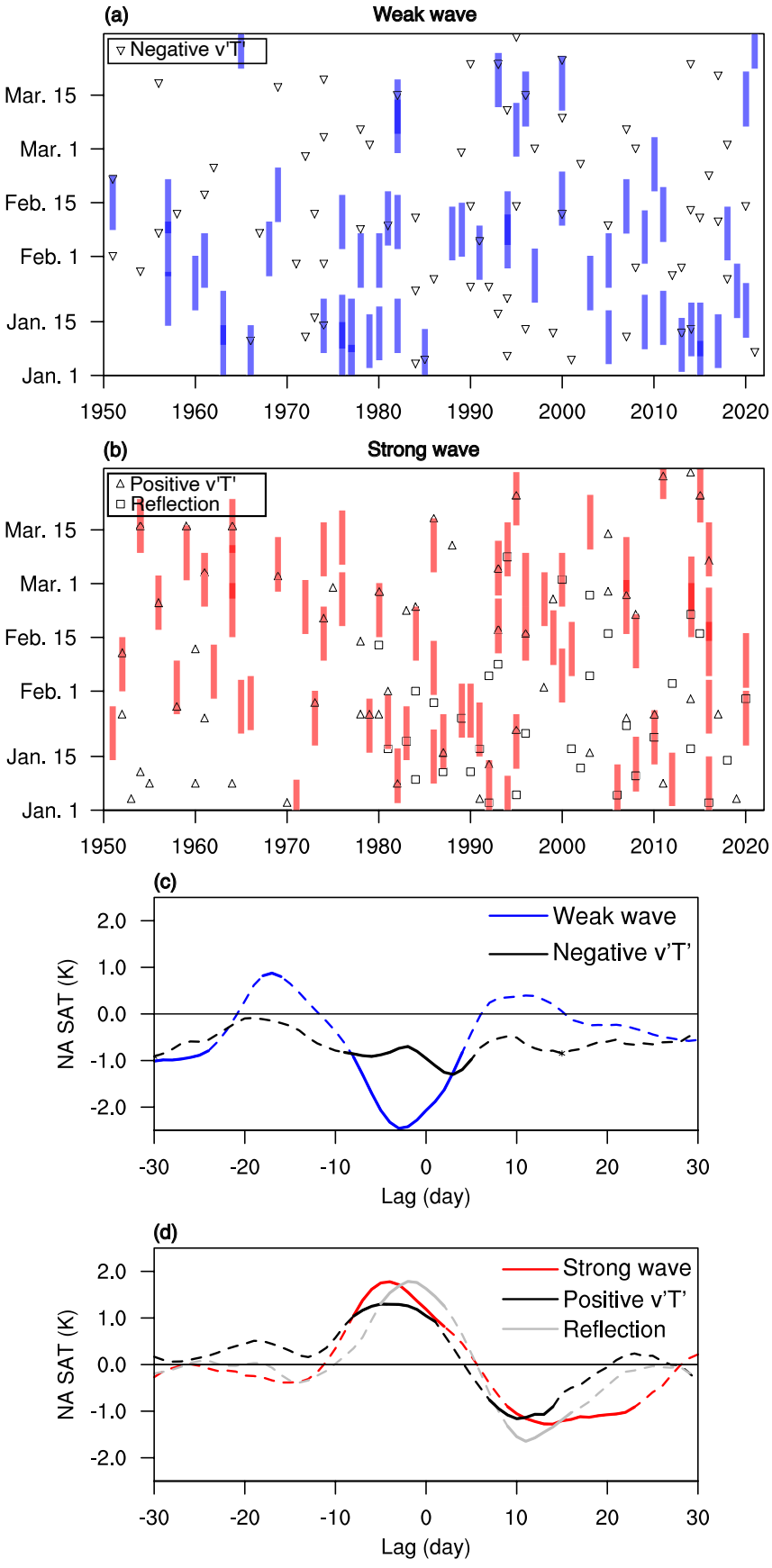
(a)
Weak wave
Negative v'T'
Mar. 15
Mar. 1
Feb. 15
Feb. 1
Jan. 15
Jan. 1
1950
1960
1970
1980
1990
2000
2010
2020
(b)
Strong wave
Positive v'T'
Reflection
(c)
Weak wave
Negative v'T'
NA SAT (K)
2.0
1.0
0.0
-1.0
-2.0
-30
-20
-10
0
10
20
30
Lag (day)
(d)
Strong wave
Positive v'T'
Reflection
NA SAT (K)
Lag (day)

Figure 4.7.9: Dates of different stratospheric events and their composites of NA SAT in ERA5. (a) 15 days around the onset of weak wave events in shading. (b) as in (a), but for strong wave events. The dates of eddy heat flux events and planetary wave reflection events are denoted in the legend in (a–b). (c) composites of NA SAT for weak wave events (blue) and negative eddy heat flux events (black). (d) composites of NA SAT for strong wave events (red), positive heat flux events (black), and reflection events (gray). The time evolution in (c–d) is smoothed by a 5-day running average. Solid parts of the lines in (c–d) represent the anomalies significant at the 95% confidence level based on the Student's *t*-test.

4.A Appendices

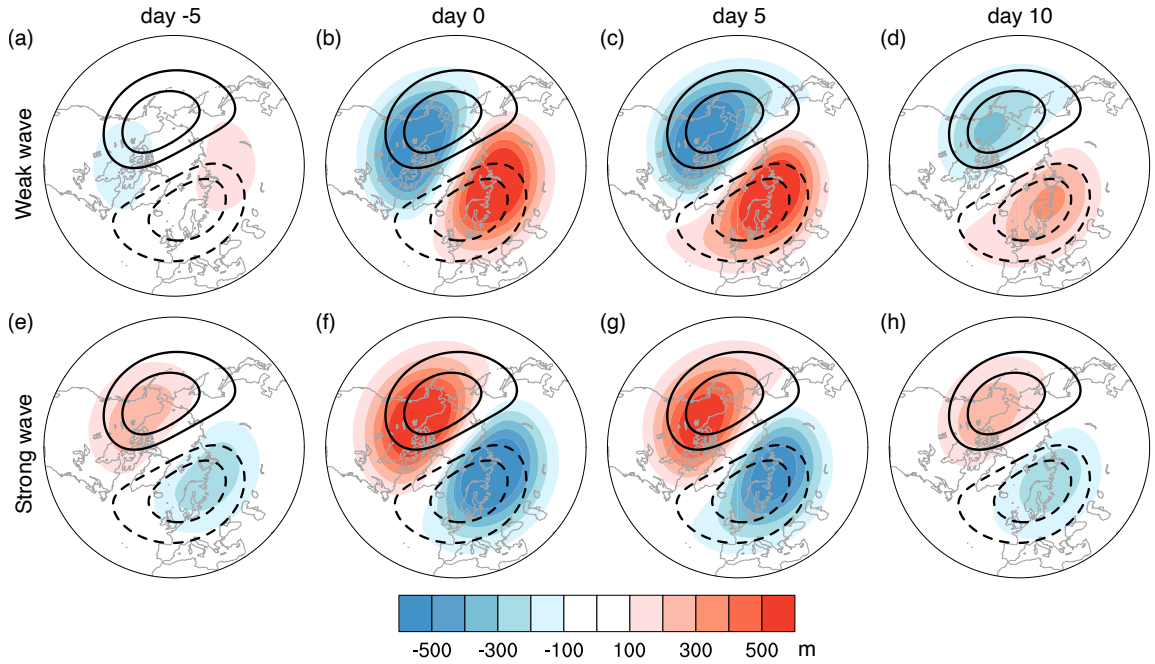

Figure 4.A.1: Composites of wave-1 component of geopotential height at 10 hPa for weak (top) and strong (bottom) stratospheric wave events in ERA5. (a and e) day -5, (b and f) day 0, (c and g) day 5, and (d and h) day 10. Contours denote 10-hPa wave-1 climatology (contour intervals: 200 m). The time evolution is smoothed by a 5-day running average.

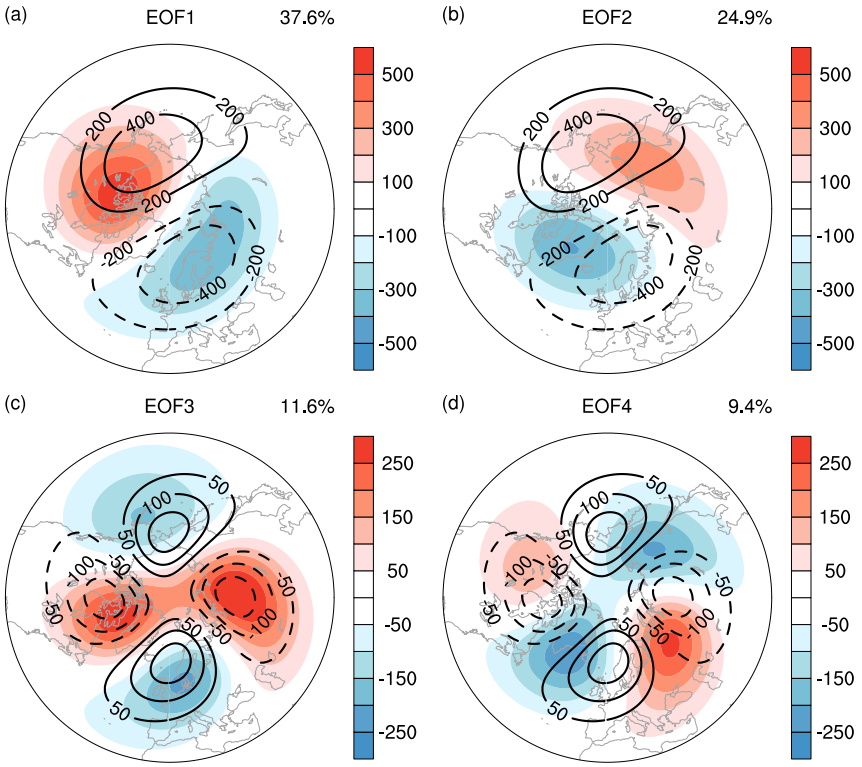

Figure 4.A.2: The first four EOF modes of the stratosphere in ERA5. (a) Regression pattern of the first EOF (EOF1). (b) Regression pattern of the second EOF (EOF2). (c) Regression pattern of the third EOF (EOF3). (d) Regression pattern of the fourth EOF (EOF4). The black contours in (a and b) indicate the climatology of 10 hPa wave-1 (contour intervals: 200m), and the black contours in (c and d) indicate the climatology of wave-2 (contour intervals: 50m.

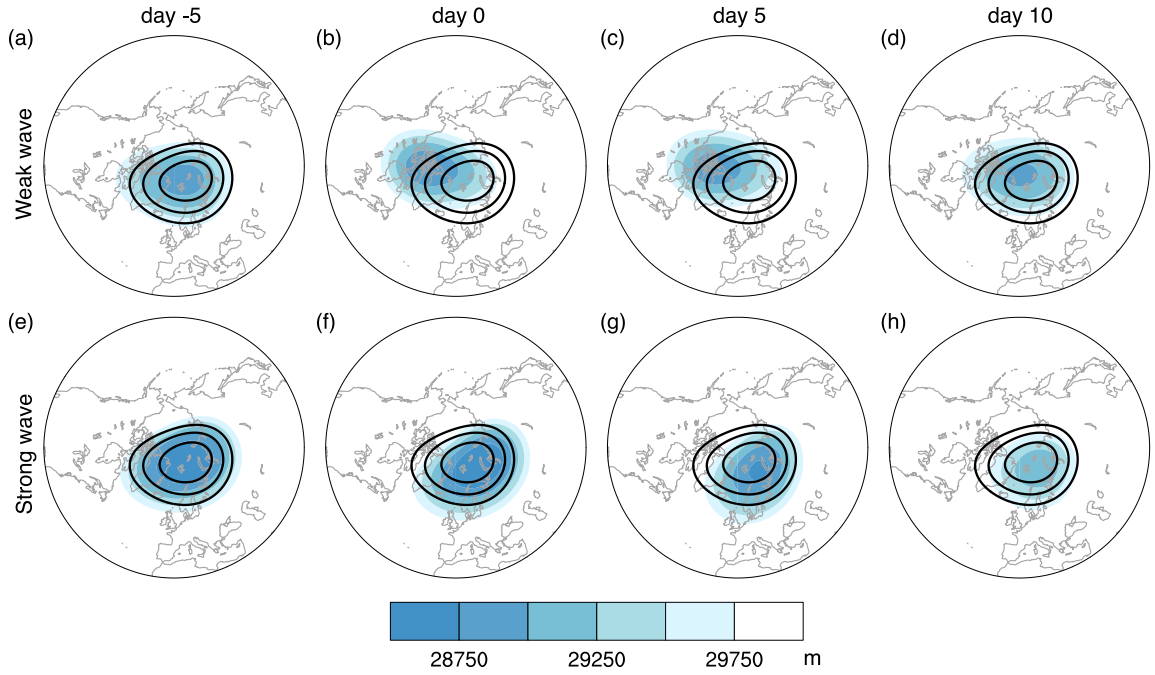

Figure 4.A.3: Composites of absolute geopotential height at 10 hPa for weak (top) and strong (bottom) stratospheric wave events in ERA5. (a and e) day -5, (b and f) day 0, (c and g) day 5, and (d and h) day 10. Contours denote 10 hPa geopotential height climatology (contour intervals: 250 m). The time evolution is smoothed by a 5-day running average.

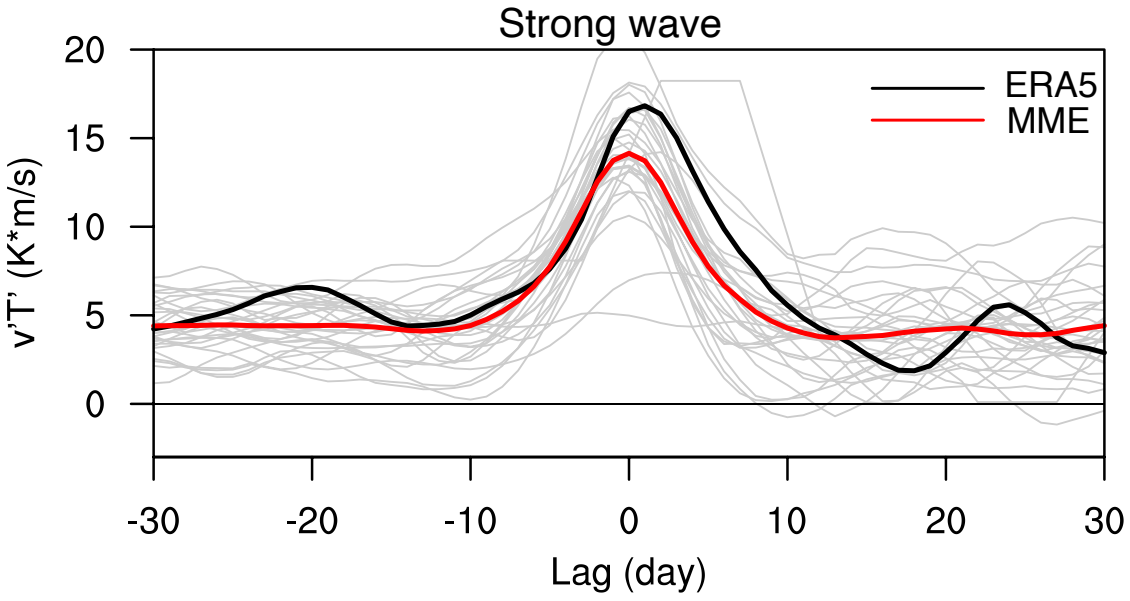

Figure 4.A.4: Zonally averaged (60°–90°N) wave-1 eddy heat flux at 100 hPa during strong stratospheric wave events in CMIP6 models. ERA5 is red lines, the CMIP6 multi-model ensemble (MME) mean is black lines, and individual models are light gray lines. The time evolution is smoothed by a 5-day running average.

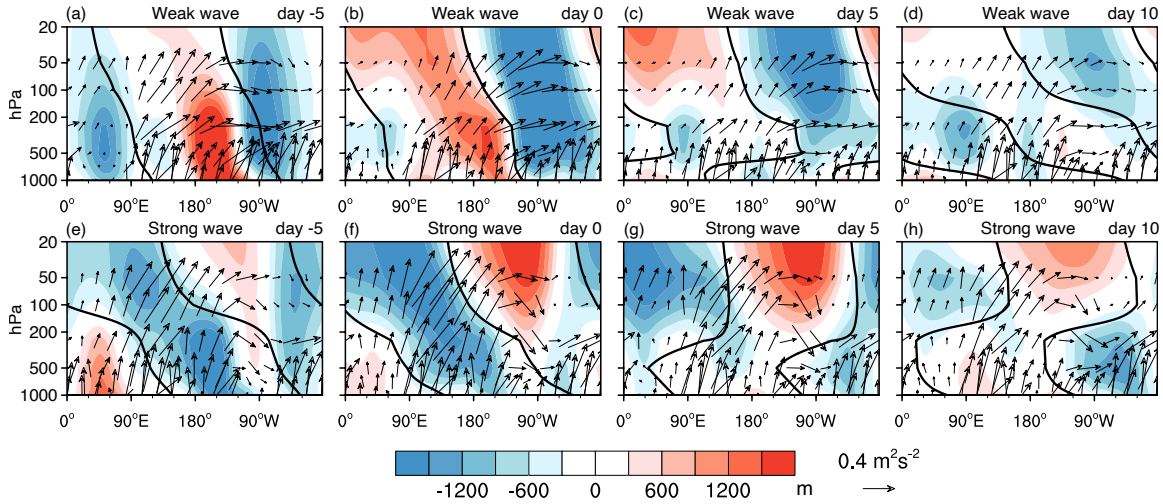

Figure 4.A.5: Vertical wave coupling during weak (top) and strong (bottom) stratospheric wave events in ERA5. As in Figure 4.7.7, but for composites of the total field of anomalous geopotential height (zonal mean + zonal asymmetry, shading) and the vertical and zonal components of absolute Plumb flux (climatology + anomalies, vector).

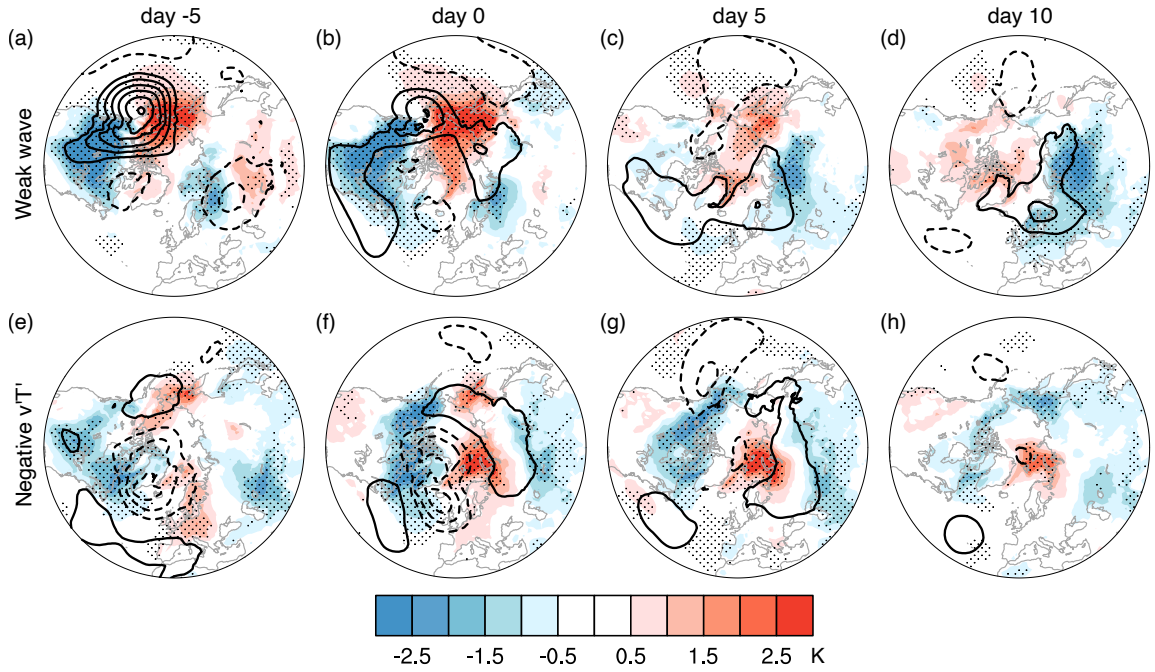

Figure 4.A.6: Composites of SAT anomalies for weak stratospheric wave events (top) and negative eddy heat flux events (bottom) in ERA5. (a and e) day -5, (b and f) day 0, (c and g) day 5, and (d and h) day 10. Contours denote SLP anomalies (contour intervals: 2 hPa). The time evolution is smoothed by a 5-day running average.

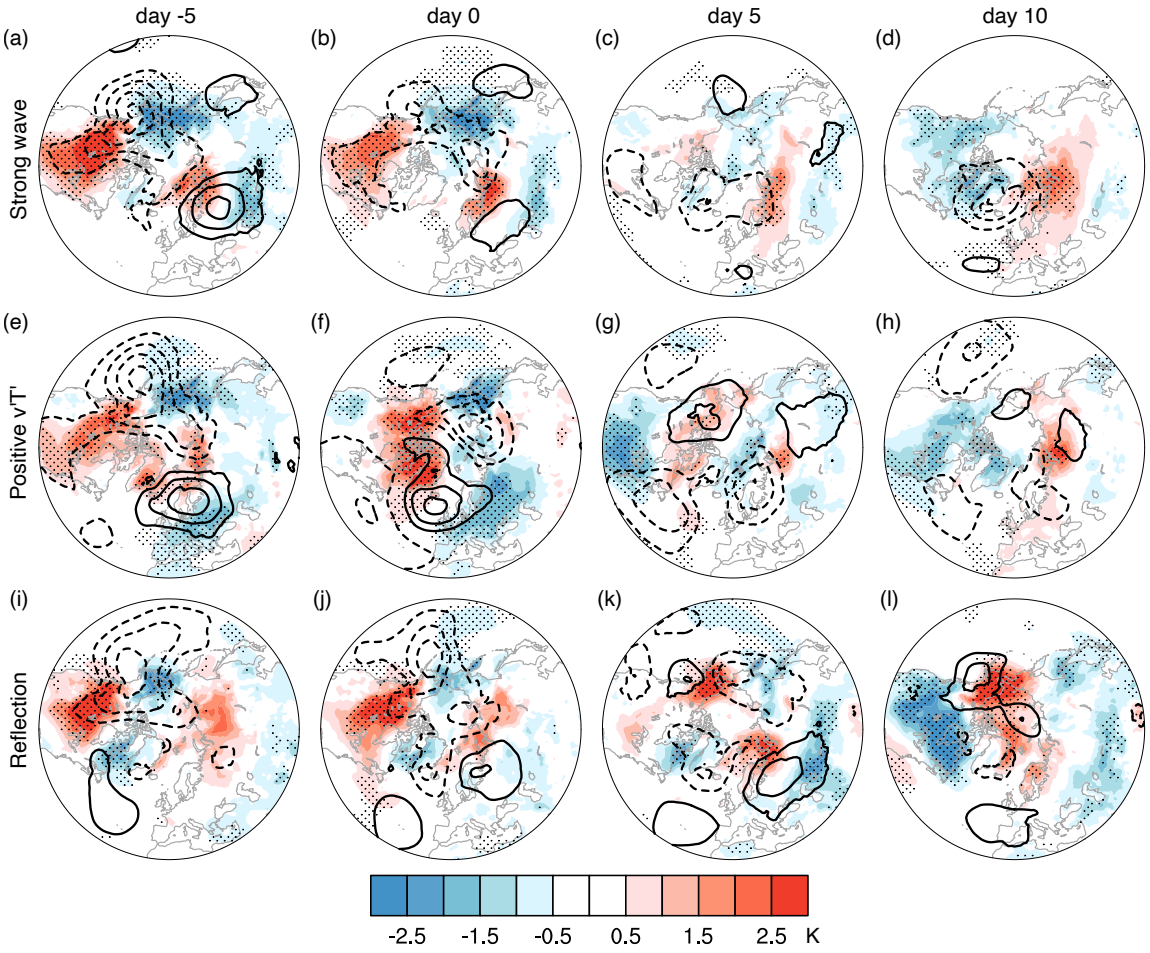

Figure 4.A.7: Composites of SAT anomalies for strong stratospheric wave events (top), positive eddy heat flux events (middle), and planetary wave reflection events (bottom) in ERA5. (a, e and i) day -5, (b, f and j) day 0, (c, g and k) day 5, and (d, h and l) day 10. Contours denote SLP anomalies (contour intervals: 2 hPa). The time evolution is smoothed by a 5-day running average.

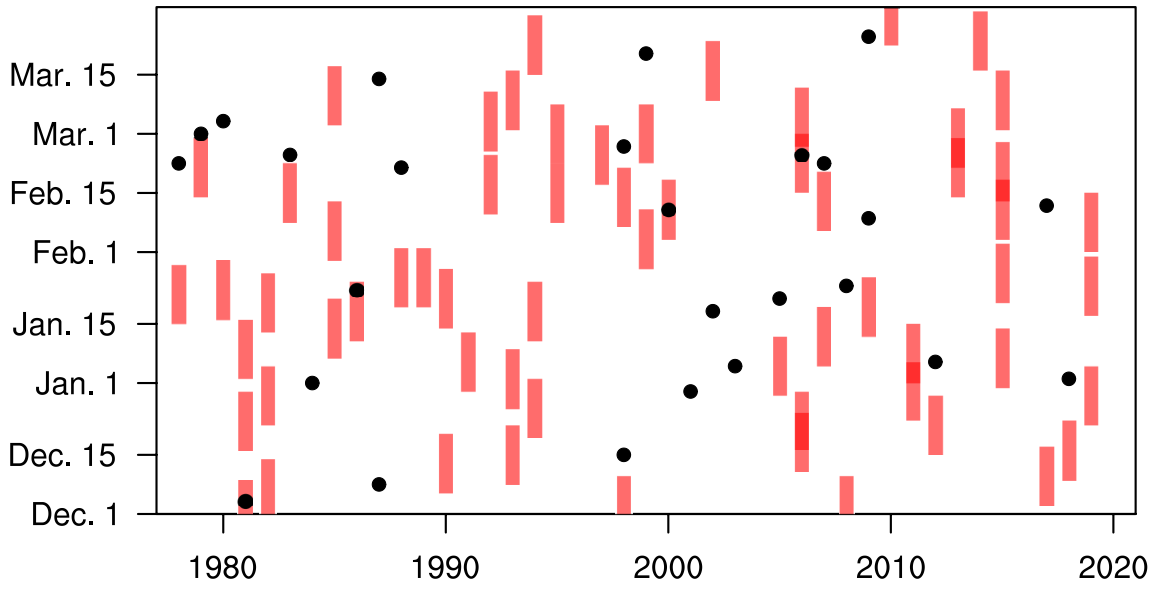

Figure 4.A.8: Dates of strong stratospheric wave events and SSWs in reanalysis. 15 days around the onset of strong wave events are shaded. The dates of SSWs are denoted with black dots.

Table 4.A.1: List of the CMIP6 models used in this study.

Model	No. of Vertical Levels	Lid Height (hPa)	Ensemble Member
ACCESS-CM2	85	0.0054	r1i1p1f1
AWI-ESM-1-1-LR	47	0.011	r1i1p1f1
BCC-ESM1	26	2.19	r1i1p1f1
CESM2	32	2.25	r1i1p1f1
CESM2-WACCM	70	4.5e-6	r1i1p1f1
CNRM-CM6-1	91	0.014	r1i1p1f2
CNRM-CM6-1-HR	91	0.014	r1i1p1f2
CNRM-ESM2-1	91	0.014	r1i1p1f2
CanESM5	49	1	r1i1p1f1
EC-Earth3	91	0.01	r1i1p1f1
FGOALS-f3-L	32	2.16	r1i1p1f1
FGOALS-g3	26	2.19	r1i1p1f1
GFDL-ESM4	49	1	r1i1p1f1
GISS-E2-1-G	40	1	r1i1p1f2
GISS-E2-2-G	102	0.002	r1i1p1f1
HadGEM3-GC31-LL	85	0.0054	r1i1p1f3
HadGEM3-GC31-MM	85	0.0054	r1i1p1f3
INM-CM4-8	21	10	r1i1p1f1
INM-CM5-0	73	0.2	r1i1p1f1
IPSL-CM6A-LR	79	0.011	r1i1p1f1
KACE-1-0-G	85	0.0054	r1i1p1f1
MIROC-ES2L	40	3	r1i1p1f2
MIROC6	81	0.004	r1i1p1f1
MPI-ESM-1-2-HAM	47	0.01	r1i1p1f1
MPI-ESM1-2-HR	95	0.01	r1i1p1f1
MPI-ESM1-2-LR	47	0.01	r1i1p1f1
MRI-ESM2-0	80	0.01	r1i1p1f1
NorESM2-LM	32	3	r1i1p1f1
NorESM2-MM	32	3	r1i1p1f1
UKESM1-0-LL	85	0.0054	r1i1p1f2

CHAPTER 5

North American Cooling Signature of Strong Stratospheric Wave Events Depends on the QBO Phase

[**Ding, X.,** Chen, G., & Magnusdottir, G., North American Cooling Signature of Strong Stratospheric Wave Events Depends on the QBO Phase, in preparation.]

Abstract

Extreme stratospheric wave activity has been linked to surface cold extremes over North America, but little is known whether the Quasi-biennial Oscillation (QBO) plays a role in this linkage. Here, by comparing strong stratospheric wave events during the westerly phase (wQBO) with those during the easterly phase (eQBO), we show that the cooling signature following strong wave events depends on the QBO phase in observations. During wQBO, strong wave events are followed by an increased risk of North American cold extremes and a vertical structure shift from a westward phase tilt to an eastward tilt. However, strong wave events under eQBO do not change the cold risk nor alter the vertical tilt. We further examine this dependence on QBO in QBO-resolving climate models, finding that the cooling signature of strong wave events in models is largely insensitive to QBO phases. This insensitivity is suggested to be linked to model biases in the stratospheric wave representation.

5.1 Introduction

Anthropogenic global warming is anticipated to reduce wintertime cold extremes (Lorenz et al., 2019; Oldenborgh et al., 2019), yet recent years have witnessed extreme cold events driven by atmospheric dynamics (Cohen et al., 2021, 2023; Johnson et al., 2018; S. Ma & Zhu,

2019). These observations have heated the ongoing debate on the drivers of cold spells (Albers et al., 2022; Harnik et al., 2016; Hartmann, 2015; Blackport et al., 2019; P. Zhang et al., 2018; R. Zhang et al., 2022). Of particular interest is the role of the stratosphere (Cohen et al., 2021; Davis et al., 2022; Huang et al., 2021; Kolstad et al., 2010; Yu et al., 2015). There is increasing evidence that extreme stratospheric wave variability contributes to surface cold waves through planetary wave reflection (Cohen et al., 2021; Kretschmer et al., 2018; Liang et al., 2022; Messori et al., 2022; Millin et al., 2022; Shaw & Perlwitz, 2013; Shen et al., 2022; Reichler & Jucker, 2022; Zou et al., 2023; Zou & Zhang, 2024). Using observations and climate models, Ding, Chen, Zhang, et al. (2023) demonstrate that strong stratospheric wave activity is followed by changes in the vertical coupling of planetary waves, with an increased risk of cold extremes over North America.

Considering the dominant role of the Quasi-biennial Oscillation (QBO) in the tropical stratosphere, it becomes pertinent to investigate whether the QBO modulates the coupling of stratospheric wave variability with the surface. The QBO has been extensively studied for its influence on the stratospheric polar vortex and associated teleconnections (Anstey, Osprey, et al., 2022; Baldwin et al., 2001; Labe et al., 2019; Rao et al., 2020). With roughly 28-month periodic variations in equatorial stratospheric zonal wind, the QBO's high predictability holds great implications for surface predictions (Anstey, Osprey, et al., 2022; Pohlmann et al., 2013; Scaife et al., 2014; Stockdale et al., 2022; Thompson et al., 2002). As first hypothesized by Holton and Tan (1980), the QBO can affect the strength of the stratospheric polar vortex by altering planetary wave propagation. In general, the polar vortex weakens when the QBO is in its easterly phase (e.g., Andrews et al., 2019; Elsbury et al., 2021b; J. Zhang et al., 2019). A weakened polar vortex often leads to the downward propagation of the negative Northern

Annular Mode (NAM) and persistent mid-latitude cold anomalies at the surface (Baldwin et al., 2021; Baldwin & Dunkerton, 2001; Domeisen, Butler et al., 2020b; Sigmond et al., 2013).

However, to our knowledge, the role of the QBO phase in the surface signature of strong stratospheric wave activity or wave reflection events remains unexplored. Ding, Chen, & Ma, (2023) emphasize the crucial role of the planetary wave pattern in the stratosphere-troposphere coupling during strong wave events, suggesting that altering the planetary wave propagating environment could affect these events and their surface linkages. Messori et al. (2022) notice that wave reflection events preferentially occur during the westerly phase of the QBO in observations. Sensitivity experiments with CESM1 indicate that the surface signal of downward wave reflection is stronger in the absence of the QBO (Lubis et al., 2016).

In this paper, we subsample strong stratospheric wave events according to QBO phases and show that strong wave events during the westerly QBO (wQBO) increase the risk of North American (NA) cold extremes while those during the easterly QBO (eQBO) do not. This suggests that the QBO may provide predictability for cold air outbreaks on sub-seasonal timescales by modulating the coupling of strong wave events. However, we find that climate models struggle to replicate this dependence on QBO phases. We further attribute the discrepancy between models and reanalysis to the different evolutions of stratospheric circulation following strong stratospheric wave events.

5.2 Data and Methods

5.2.1 Reanalysis and Climate Models

We analyze the daily data from the fifth generation of atmospheric reanalysis from the European Center for Medium-Range Weather Forecasts (ERA5; Hersbach et al., 2020). The

data we examined have a horizontal resolution of 1.5°×1.5° and cover the period of 1950–2021. We focus on the boreal winter from December to February. After detrending, the anomalies are obtained by removing the seasonal cycle, which is defined as the time mean and first two harmonics of the full-year climatology.

We also examine climate models from the Coupled Model Intercomparison Project Phase 6 (CMIP6). We select 16 models that are shown to realistically simulate the QBO (Rao et al., 2023; Richter et al., 2020; Zuo et al., 2022). The historical simulations we examined cover the period of 1950–2014. All model data are bilinearly interpolated to a 1.5°×1.5° common grid. Only one member from each model is used. The list of CMIP6 models and the ensemble members used are shown in Table 5.A.1.

Since the QBO in climate models has a weak amplitude at 50 hPa compared to reanalysis, here the QBO is indexed using the standardized seasonal 10 hPa zonal wind that is averaged between 5°S and 5°N (Elsbury et al., 2021a). This works because of the anticorrelation between 10 hPa and 50 hPa QBO winds (Anstey, Simpson, et al., 2022; Richter et al., 2020). We define a wQBO year when the QBO index is smaller than -0.5 and an eQBO year when the index is larger than 0.5. According to this definition, there are 28 eQBO and 31 wQBO years in ERA5. The numbers of QBO years in each model are listed in Table 5.A.1. The main conclusions are not sensitive to the chosen QBO indexing scheme.

5.2.2 Definition of Strong Stratospheric Wave Events

We identify strong stratospheric wave events based on the empirical orthogonal function (EOF) analysis of the 10 hPa geopotential height, for ERA5 and each model individually (Ding, Chen, Zhang, et al., 2023; Ding, Chen, & Ma, 2023). While the lower stratosphere is

more strongly related to tropospheric variability, using the 10 hPa field makes it more straightforward to identify the contribution of stratospheric variability to tropospheric weather. EOF analysis is applied to the zonally asymmetric geopotential height (removing the zonal mean) north of 20°N, weighted by the square root of the cosine of latitude. We note that the leading EOF pattern encompasses the variability from all zonal wave numbers. The standardized principal component of the leading EOF mode is taken as the stratospheric planetary wave index, largely describing the strength of the planetary wave-1 in the stratosphere. While wave-2 patterns from other EOFs may also have important implications (e.g., Charlton & Polvani, 2007), we focus on the wave-1 pattern from the leading EOF due to its predominant explained variance (Ding, Chen, & Ma, 2023). A strong stratospheric wave event is identified as the consecutive days when the planetary wave index is above its 95th percentile. No minimum duration is required. Day 0 refers to the first day meeting the threshold.

The strong stratospheric wave events are subsampled based on the QBO phase of the winter in which the event occurs. In ERA5, this results in a frequency of 1.23 strong wave events per year during wQBO years (38 events in total) and 0.75 events per year during eQBO years (21 events in total). The CMIP6 ensemble produces, on average, 1.07 strong wave events per wQBO year (451 events in total) and 0.98 events per eQBO year (414 events in total). The numbers of strong wave events in each model are listed in Table 5.A.1.

5.2.3 Plumb Wave Activity Flux

We calculate the Plumb wave activity flux to describe the 3D propagation of planetary waves (Plumb, 1985)

$$\{F^{\lambda}, F^{\phi}, F^{z}\} = p\cos(\phi)\left\{v'^{2} - \frac{1}{fa\cos(\phi)}\frac{\partial(v'\Phi')}{\partial\lambda}, -u'v' + \frac{1}{fa\cos(\phi)}\frac{\partial(u'\Phi')}{\partial\lambda},\right.$$

$$\left.\frac{f}{\partial\tilde{T}/\partial z + \kappa\tilde{T}/H}\left[v'T' - \frac{1}{fa\cos(\phi)}\frac{\partial(T'\Phi')}{\partial\lambda}\right]\right\}$$

where λ is longitude, ϕ is latitude, z is height, and p is pressure. T is temperature, Φ is geopotential height, u is the zonal wind, and v is the meridional wind. f is the Coriolis parameter and a is Earth's radius. κ is the specific gas constant of dry air divided by the specific heat of dry air. $\tilde{T}$ is the domain-averaged temperature. H is the log-pressure scale height. Primes denote the deviations from zonal means.

It is noteworthy that the upward propagation of planetary waves can also be inferred from the westward tilt of geopotential height anomalies with increasing altitude. While the direction of the wave tilt for the composite of height anomalies implies the sign of transient eddy fluxes, Plumb fluxes include both transient eddy fluxes and the interference between transient and climatological planetary waves.

5.3 Results

5.3.1 QBO Modulates the Surface Signal of Strong Stratospheric Wave Events in Reanalysis

We first compare the evolution of circulation patterns during strong stratospheric wave events for the two QBO phases in ERA5 (Figure 5.5.1). The 10 hPa geopotential height anomalies linked to strong stratospheric wave events during wQBO and eQBO years share similar patterns, featuring an NA ridge and a Eurasian trough (Figures 5.5.1a–1b). This wave-1 pattern is largely in phase with the wave-1 climatology and reinforces the climatological wave-1 via constructive wave interference (Ding et al., 2022; K. L. Smith &

Kushner, 2012). We note that on day 10, the ridge anomaly under eQBO is slightly stronger compared to that under wQBO, implying a more persistent NA ridge associated with eQBO strong wave events. The zonal mean component of their differences corresponds to a positive NAM (Figure 5.5.1c), which is attributable to the QBO effect on the seasonal mean polar vortex and diminishes after removing winter means (Figure 5.A.1). However, removing this QBO modulation on winter means does not affect the tropospheric signals to be described below (Figures 5.A.1 and 5.A.2), suggesting that the impact of QBO on strong wave events acts on a shorter timescale than its influence on the polar vortex. For 500 hPa composites, strong stratospheric wave events under different QBO phases are similar before and around the event onset (days -5–0), showing a strong Alaskan trough and two ridges over eastern North America and Europe (Figures 5.5.1a–1b). These observed precursor patterns match the ones associated with strong wave events during all the winters regardless of QBO phases and also resemble the pattern during negative eddy heat flux events (Ding, Chen, & Ma, 2023; Shaw & Perlwitz, 2013). However, on day 10, wQBO strong wave events show a northern North Pacific ridge and an NA trough while eQBO events display a northern North Pacific trough. This is more clearly shown in the differences between wQBO and eQBO (Figure 5.5.1c). The opposite signs of the northern North Pacific anomalies may explain the negligible tropospheric signal over the North Pacific when considering all the winters (see Figure 2 in Ding, Chen, & Ma, 2023). In other words, the tropospheric precursor transitions into an opposite pattern during wQBO strong wave events while the precursor is maintained through the lifecycle of eQBO events.

The related surface signals during wQBO and eQBO are consistent with the mid-tropospheric circulation anomalies. The composite of wQBO strong wave events features a transition from warm anomalies over North America before the event onset to cold anomalies on day 10

(Figure 5.5.2a). This temperature swing coincides with a shift from a cyclonic anomaly in sea level pressure (SLP) over Alaska to an anticyclonic anomaly 5 to 10 days later. These surface signatures during wQBO are largely in line with those during all the winters, except for the Alaskan anticyclonic anomaly (Ding, Chen, Zhang, et al., 2023). On the other hand, the surface composite of eQBO strong wave events is characterized by a persistent cyclonic anomaly over Alaska (Figure 5.5.2b). This induces warm anomalies over North America and mitigates the temperature drop. We note that the warm signal on day 10 is insignificant, accompanied by some cooling around Davis Strait and the west coast of the United States. Interestingly, the SLP anomalies over the Atlantic project onto the positive North Atlantic Oscillation (NAO) regardless of the QBO phase, consistent with the results during all the winters. It is worth noting that these surface signals following strong wave events are distinct from those related to anomalous polar vortex events (Ding et al., 2022; Ding, Chen, & Ma 2023; Messori et al., 2022). This result also aligns with the finding that the weather regime most sensitive to the polar vortex strength is not the most important for NA cold extremes (Lee et al., 2019). While the temperature drop over North America has been connected to the stratosphere through wave coupling (Ding, Chen, Zhang, et al., 2023; Guan et al., 2020; Messori et al., 2022; Shen et al., 2022), Figure 5.5.2 suggests a more nuanced picture of this connection that depends on the QBO phase.

Vertical wave structures associated with strong stratospheric wave events under different QBO phases are compared by using zonally asymmetric geopotential height anomalies and Plumb flux anomalies averaged over 50°–70°N (Figure 5.5.3). Before and around the onset, strong wave events under wQBO and eQBO both show upward and eastward Plumb flux anomalies over Siberia, reinforcing the stratospheric ridge over North America (Figures 5.5.3a–3b). Accordingly, the geopotential height anomalies and their wave-1 components

(black lines in Figure 5.5.3) are characterized by a westward phase tilt with altitude. Around day 5 to day 10, wQBO strong wave events feature a shift to an eastward tilt, coinciding with the downward Plumb flux anomalies over North America (Figure 5.5.3a). This wave phase alteration is consistent with the results using all the winters, which may be thought of as an indication of local wave reflection (Ding, Chen, & Ma, 2023; Holton & Mass, 1976; Perlwitz & Harnik, 2003). However, a westward tilt of geopotential height anomalies persists throughout strong wave events during eQBO (Figure 5.5.3b).

From a perspective of weather systems, wQBO strong wave events are followed by a weakening of the stratospheric NA ridge, which descends and forms an anomalous ridge over the northern North Pacific in the troposphere (Figure 5.5.3a), reminiscent of the evolution during planetary wave reflection (Kodera et al., 2013). This also leads to the development of an NA trough downstream that favors cold air advection (Figure 5.5.1). In contrast, the NA ridge is largely confined in the stratosphere following eQBO strong wave events while the northern North Pacific is occupied by a tropospheric trough (Figure 5.5.3b).

We also examine zonally averaged zonal winds during strong wave events under wQBO and eQBO (Figure 5.A.3). While they both show zonal wind deceleration in the extratropical region, only strong wave events under wQBO are associated with a vertical dipole structure around day 0, marked by significant negative anomalies in the upper stratosphere and positive anomalies below (Figure 5.A.3a). This dipole pattern implies a potential reflective surface of planetary waves (Perlwitz & Harnik, 2003). Besides, despite the increased upward wave propagation, wQBO strong wave events do not show negative zonal wind anomalies in high latitudes like eQBO strong wave events (Figure 5.A.3), suggesting that the waves are not absorbed in the stratosphere. Figure 5.A.4 shows that the stratospheric zonal wind speed

decreases with altitude around the onset of strong wave events during wQBO (blue line), further indicating the formation of a vertical reflective surface (Perlwitz & Harnik, 2003). These results imply that wQBO induces a favorable condition for vertical wave reflection, leading to the vertical structure shift and subsequent cold advection over North America following strong wave events (Figures 5.5.2 and 5.5.3).

In summary, reanalysis indicates that the QBO phase modulates the surface signal of strong stratospheric wave events, with an increased risk of cold extremes over North America during westerly QBO but a muted risk during easterly QBO.

5.3.2 CMIP6 Models Lack the Sensitivity of Strong Stratospheric Wave Events to the QBO

It is then interesting to ask whether climate models can capture the dependence of the vertical wave coupling on the QBO phase. To this end, we compare the time series of stratospheric and tropospheric indices under different QBO phases in ERA5 and CMIP6 (Figure 5.5.4). The regionally averaged 10 hPa geopotential height anomalies over northern North America (50°–90°N, 80°W–180°) are compared with 500 hPa anomalies over the northern North Pacific (50°–70°N, 150°E–130°W). We select these regions due to the contrast between wQBO and eQBO events and linkages to NA cold anomalies (Figures 5.5.1 and 5.5.2). Following strong wave events under wQBO, the CMIP6 multi-model ensemble (MME) mean (red lines in Figure 5.5.4) shows a slightly more persistent stratospheric NA ridge compared to ERA5 (Figure 5.5.4a). As for the troposphere, the CMIP6 MME presents virtually no anomalies over the northern North Pacific in contrast to an attenuated Aleutian Low in ERA5 during days 5–20 noted by the weakly positive anomalies (Figure 5.5.4c). The difference between CMIP6 and ERA5 under eQBO is generally the opposite but with larger amplitudes:

the stratospheric NA ridge weakens during days 5–20 in CMIP6 while it sustains in ERA5 (Figure 5.5.4b). In the troposphere, CMIP6 shows negligible anomalies though ERA5 exhibits a significantly strengthened Aleutian Low (Figure 5.5.4d). A similar comparison between CMIP6 and ERA5 can be drawn from circulation patterns (cf. Figure 5.5.1 vs. Figure 5.A.6). These results suggest that the evolution of the stratospheric northern NA ridge after the onset is connected to strong wave events' tropospheric signals over the northern North Pacific. Moreover, CMIP6 models seem to lack the sensitivity of this connection to QBO phases which is observed in ERA5.

Of particular interest is the linkage between strong stratospheric wave events and cold extremes over North America. Figures 5.5.4e and 4f present the Probability Density Function (PDF) of NA surface air temperature (SAT) (40°–70°N, 70°W–130°W) anomalies during days 5–20 after strong wave events under wQBO and eQBO. In ERA5, wQBO strong wave events feature a general shift towards colder temperatures that is 95% significant based on the two-tailed two-sample Kolmogorov-Smirnov (KS) test, whereas eQBO events show little change (Figure 5.5.4e). The extreme cold risk is further quantified by the risk ratio for the exceedance frequency below a certain standard deviation (SD) of the PDF. Compared to all the winter days, wQBO strong wave events increase the risk of exceeding -1, -1.5, and -2 SD below climatology by 50%, 80%, and 110%, which is higher than those of strong wave events during all the winters (Ding, Chen, Zhang, et al., 2023). Strong wave events during eQBO, on the contrary, decrease the cold extreme risk of exceeding -1.5 and -2 SD by 10% and 60%. These divergent cold risks under wQBO and eQBO match the observed patterns (Figure 5.5.2). However, the CMIP6 PDFs during wQBO and eQBO both indicate a statistically significant shift toward colder anomalies based on the KS test (Figure 5.5.4f). Consistent results are found in the risk ratios for exceedance frequency, showing virtually no differences between

wQBO and eQBO (1.3, 1.3, 1.1 vs. 1.3, 1.2, 1.0). These results suggest that CMIP6 models simulate a biased surface signature following strong stratospheric wave events under eQBO, with the NA cold signals being too strong compared to ERA5. These findings are also confirmed by the temporal evolution of NA SAT (Figure 5.A.7). In Figure 5.A.7, we also note that strong wave events under eQBO are followed by significant NA cold anomalies with a 20-day lag. However, the associated SLP pattern is different from that on day 10 after wQBO strong wave events, which features positive NAO over the Atlantic (Figure 5.A.8). In addition, the anomalies on day 20 are isolated and confined to the troposphere (Figure 5.A.9b). These results suggest that the NA cold anomalies following eQBO strong wave events with a 20-day lag are not directly related to the surface response to strong wave events analyzed in this study.

An outstanding question is whether the biased cooling signature of strong stratospheric wave events can be linked to the stratospheric representation. Ding, Chen, and Ma (2023) demonstrated that models with a degraded representation of stratospheric wave structure tend to exhibit biases in the surface signals of strong wave events. Our analysis reveals that, following the onset of eQBO strong wave events, the CMIP6 MME simulates a stratospheric wave pattern that diverges from the ERA5 results (Figure 5.5.4b). This discrepancy prompts us to consider if differences in the stratospheric ridge evolution are linked to the varied tropospheric signals across models. To investigate this potential connection, Figure 5.5.5 presents a scatterplot for the changes in the stratospheric northern NA ridge (between days 5–20 and days -5–5) versus tropospheric anomalies over the northern North Pacific during days 5–20 across CMIP6 models. There is a statistically significant linear correlation for both strong wave events during wQBO ($r = -0.51$) and events during eQBO ($r = -0.54$), consistent with the finding that a cyclonic anomaly over the northern North Pacific tends to enhance

upward wave propagation (e.g., Garfinkel et al., 2010; Woollings et al., 2010). We caution that the correlations for the vertical wave coupling may involve interactions with changes in the stratospheric polar vortex (Domeisen, Butler, et al., 2020b; Huang et al., 2021; Kolstad et al., 2010; Lawrence et al., 2020) or the Madden-Julian oscillation (MJO; Johnson et al., 2014) during different QBO phases, but isolating all the factors of climate variability is beyond the scope of the present study.

This intermodel relation supports that a more pronounced weakening of the stratospheric ridge after strong wave events correlates with tropospheric anticyclonic anomalies over the North Pacific, inducing NA cold anomalies (Figure 5.5.4). The CMIP6 MME (green squares in Figure 5.5.5) shows negligible differences between wQBO and eQBO. Interestingly, ERA5 strong wave events during eQBO approach the uncertainty limit (2 SD) of CMIP6, whereas ERA5 events during wQBO align closely with the CMIP6 MME. This suggests that the discrepancy between CMIP6 and ERA5 cannot be fully explained by internal variability which is part of model uncertainties. The stratospheric and tropospheric signals following strong wave events in climate models are systematically biased for eQBO, leading to models' insensitivity to QBO phases after strong stratospheric wave events. We also note that the stratospheric zonal wind in ERA5 strongly decelerates after eQBO strong wave events, while it remains relatively unchanged in the CMIP6 MME (Figure 5.A.10). This is consistent with models' known tendency to underpredict the weakening of the polar vortex associated with eQBO (e.g., Elsbury et al., 2021a).

5.4 Conclusions

In this paper, we have investigated how the surface conditions following extreme stratospheric events may depend on the QBO phase, by comparing strong stratospheric wave

events during wQBO and eQBO years. In contrast to most previous studies on the QBO that were focused on the role of SSWs in modulating the risk of cold extremes at the surface (e.g., Rao et al., 2020), this study sheds light on an alternative stratospheric pathway through vertical wave coupling. During wQBO, strong wave events are followed by a northern North Pacific ridge in the troposphere, increasing cold risks over North America. Conversely, strong wave events under eQBO show a persistent tropospheric trough throughout the lifecycle, resulting in muted NA cold risks. Accordingly, the vertical structure shifts from a westward phase tilt to an eastward tilt during wQBO events while remaining at a westward tilt during eQBO events. This dynamic insight may prove beneficial for subseasonal predictions of cold extremes when integrated with other factors such as the El Nino-Southern Oscillation (ENSO; Albers et al., 2022; Kenyon & Hegerl, 2008; Xiang et al., 2019), the stratospheric polar vortex (Domeisen, Butler, et al., 2020b; Huang et al., 2021; Kolstad et al., 2010; Lawrence et al., 2020; Scaife et al., 2022), and the MJO (Johnson et al., 2014). We also note that this pathway differs from the established connection between the QBO and the NA coldness through SSWs, as strong stratospheric wave events are distinct from SSWs in terms of surface impacts and mechanisms (Ding et al., 2022; Ding, Chen, & Ma 2023; Messori et al., 2022). Therefore, a comprehensive comparison of different pathways of QBO's influences on surface weather warrants future research.

Although eQBO tends to induce a weak polar vortex, there are more strong stratospheric wave events during wQBO (38 events) than during eQBO (21 events). This discrepancy may be reconciled by different timescales of these events. The stratosphere-troposphere coupling of strong wave events acts on a shorter timescale compared with an anomalous polar vortex (Ding et al., 2022). In addition, strong wave events are preceded by a stronger-than-normal polar vortex, which may be related to the stratospheric preconditioning for upward wave

activity (Ding et al., 2022; McIntyre, 1982). Thus, the seasonally stronger polar vortex during wQBO may provide a favorable condition for strong wave events. We have also examined the sea surface temperature (SST) anomalies associated with strong wave events (Figure 5.A.11), consistent with the SST patterns linked to the QBO (Randall et al., 2023). The implications of these SST anomalies on planetary waves require further investigation.

The QBO impact on strong stratospheric wave events is further examined in QBO-resolving CMIP6 models. We found that models do not replicate the distinct surface signatures under different QBO phases observed in reanalysis, suggesting a lack of sensitivity to QBO phases in climate models. Instead, the models consistently show an increased risk in NA cold following strong wave events during both wQBO and eQBO years. The lack of QBO dependence is linked to the absence of tropospheric anomalies over the northern North Pacific. This may be attributed to biases in the evolution of the stratospheric ridge following eQBO strong wave events. Similarly, the persistence of stratospheric anomalies following SSWs has been suggested to strongly influence their tropospheric impact (Maycock & Hitchcock, 2015). In addition, many models exhibit an unrealistic reduction in upward wave fluxes in the lower stratosphere (Wu & Reichler, 2020). Our results imply that models have biases of excessive downward coupling under eQBO, which may contribute to this issue. The root cause behind the model's insensitivity of strong wave events to the QBO phase warrants future investigation, potentially including considerations of the QBO structure (H. Kim et al., 2020), model climatology (Karpechko et al., 2021), and lid height and vertical resolution (Shaw et al., 2014; Wu & Reichler, 2020).

Our results add to the growing body of research on the QBO's global impacts. Previous literature has documented that the stratosphere's downward influence is sensitive to various

factors modulating planetary waves, such as ENSO (Butler & Polvani, 2011; Domeisen et al., 2019), topography (Garfinkel et al., 2020; Gerber & Polvani, 2009; Wang et al., 2023), and sea ice (B.-M. Kim et al., 2014; Sun et al., 2015). Our analysis has demonstrated that the surface signature of strong stratospheric wave events and the associated cold extreme risk over North America depends on the phase of the QBO. In this regard, while a few studies have shown that downward wave reflection is susceptible to SST, solar activity, and sea ice (Lu et al., 2017; Lubis et al., 2016, Zou & Zhang, 2024), much work is needed to understand the sensitivity of extreme stratospheric wave activity to various factors of climate variability. Findings from our paper could potentially enhance forecasting of severe winter cold in the U.S. and Canada, benefiting transportation, energy management, and public health by enabling better preparedness and resource allocation (Charlton-Perez et al., 2019; Perera et al., 2020; Vajda et al., 2014).

Acknowledgments. We acknowledge the WCRP Working Group on Coupled Modeling which is responsible for the CMIP. We also acknowledge high-performance computing support from Cheyenne (https://doi.org/10.5065/D6RX99HX) provided by NCAR's Computational and Information Systems Laboratory, sponsored by the National Science Foundation. G.C. is supported by the U.S. NSF grant AGS-2232581 and NASA grant 80NSSC21K1522. The authors declare that they have no competing interests.

5.5 Figures

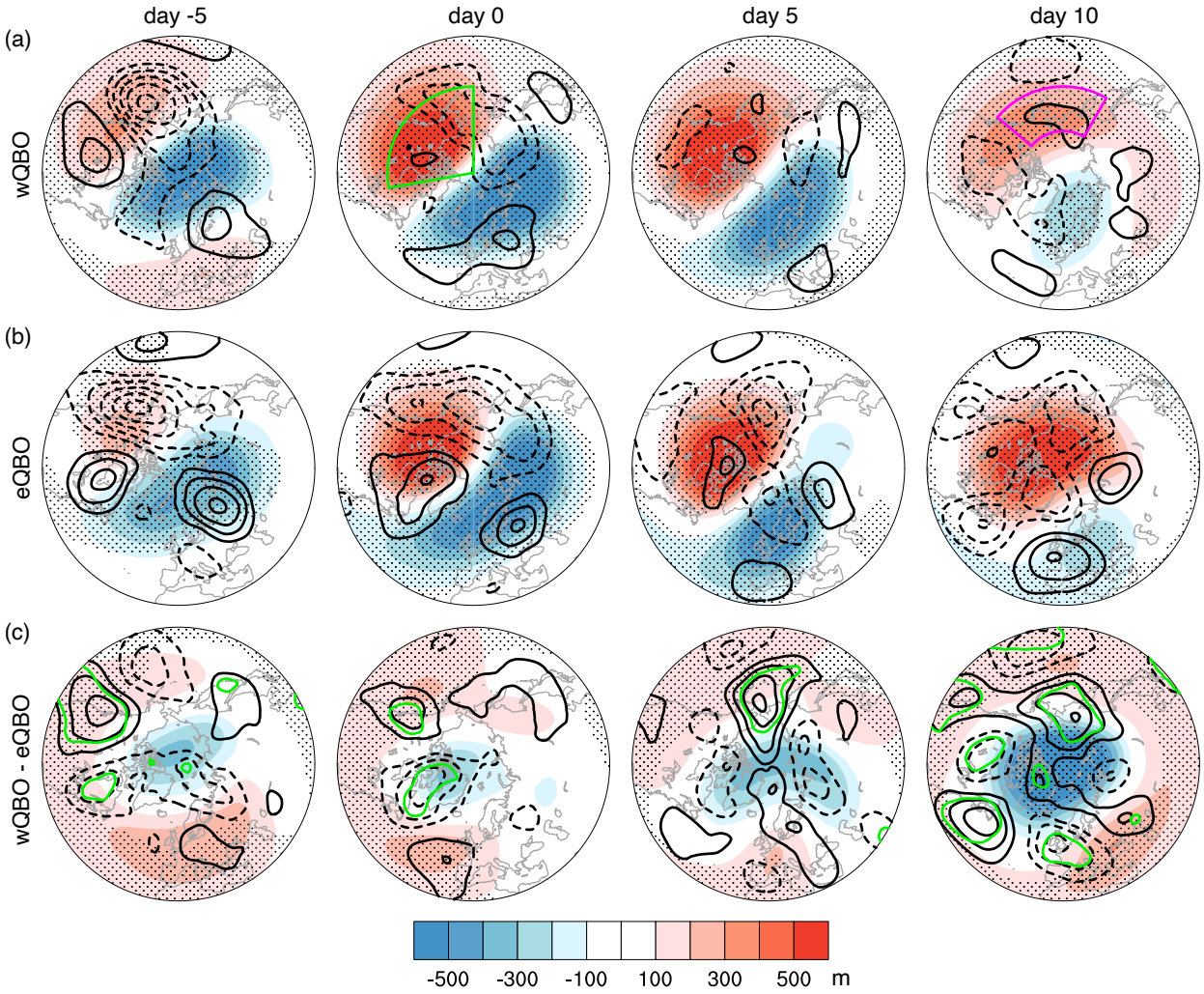

Figure 5.5.1: Composites of geopotential height anomalies at 10 hPa (Z10, shading) and 500 hPa (Z500, contours, 25 m interval) on day -5, 0, 5, and 10 for strong stratospheric wave events in ERA5 under wQBO (a) and eQBO (b). (c) differences between (a) and (b). Stippling in (a, b) denotes the regions where the shaded anomalies are significant at the 95% confidence level based on the two-sided Student's *t*-test. Stippling in (c) denotes 95% significant differences based on two-sided Welch's unequal variances *t*-test. The time evolution is smoothed by a 5-day running average. Day -5 represents the average between day -7 and day -3. The green box in (a) (50°–90°N, 80°W–180°) indicates the region where stratospheric ridge anomalies are calculated, and the magenta box (50°–70°N, 150°E–130°W) indicates the region of tropospheric northern North Pacific anomalies.

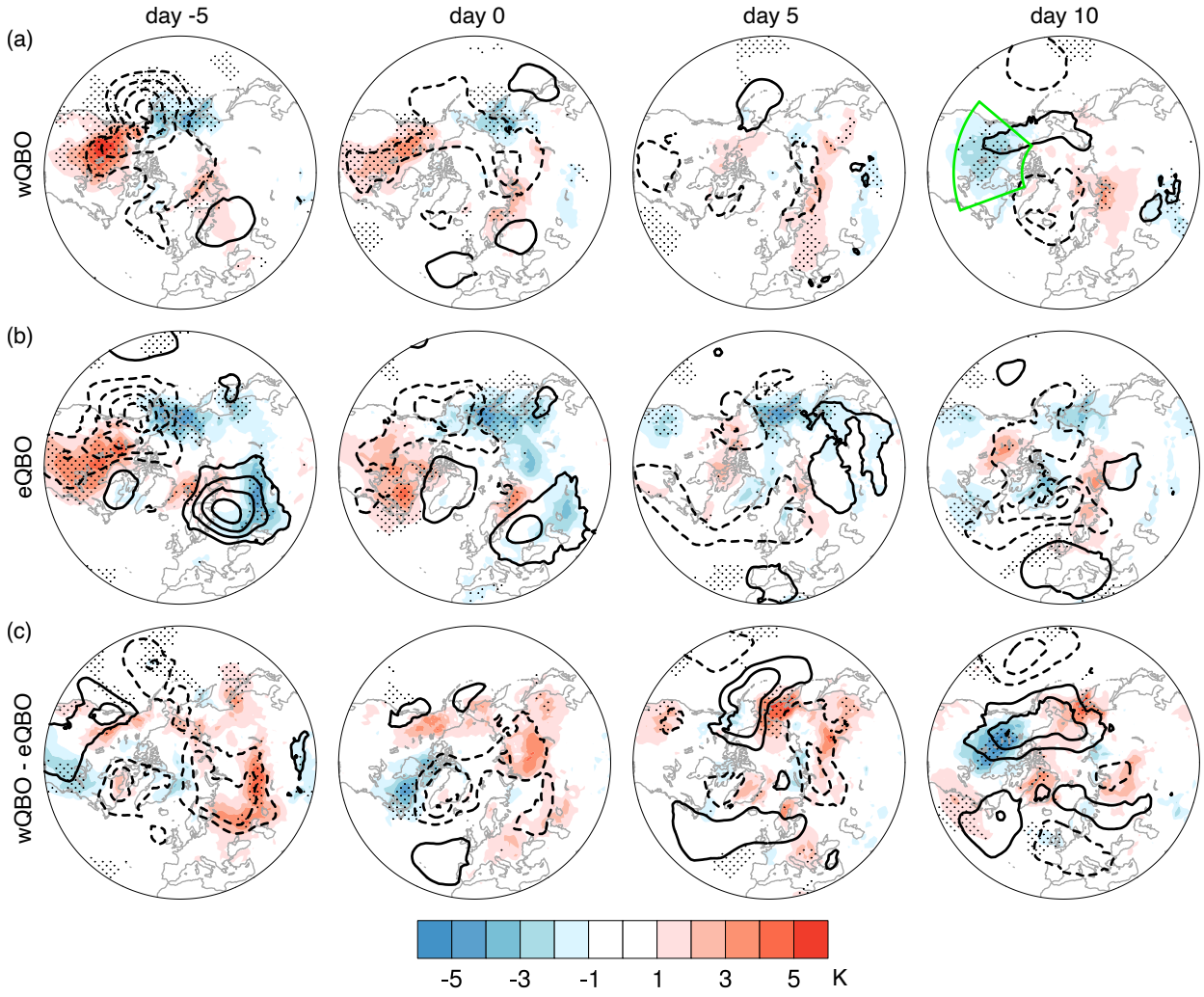

Figure 5.5.2: Composites of surface air temperature (SAT, shading) and SLP (contours, 2.5 hPa interval) on day -5, 0, 5, and 10 for strong stratospheric wave events in ERA5 under wQBO (a) and eQBO (b). (c) differences between (a) and (b). Stippling in (a, b) denotes the regions where the shaded anomalies are significant at the 95% confidence level based on the two-sided Student's *t*-test. Stippling in (c) denotes 95% significant differences based on two-sided Welch's unequal variances *t*-test. The time evolution is smoothed by a 5-day running average. Day -5 represents the average between day -7 and day -3. The green box in (a) (40°–70°N, 70°W–130°W) indicates the region of NA SAT anomalies.

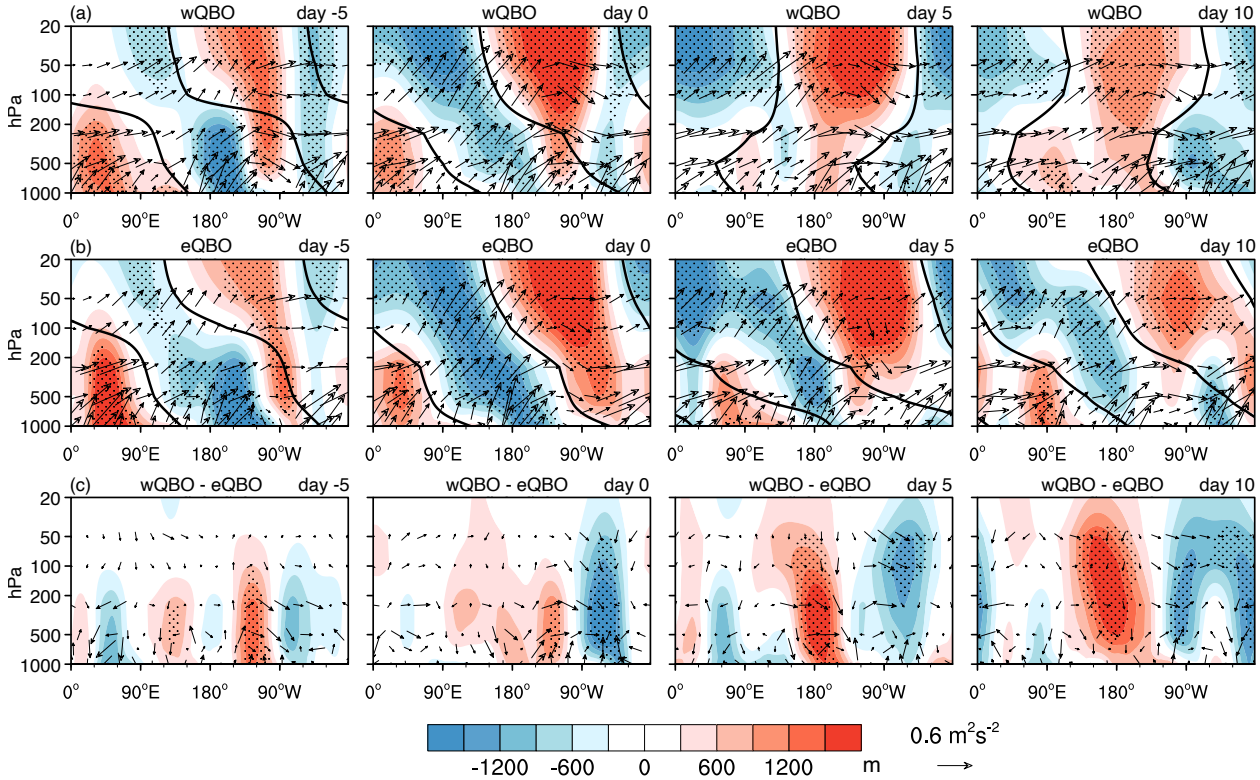

Figure 5.5.3: Vertical wave coupling associated with strong stratospheric wave events during wQBO and eQBO in ERA5. (a) Composites of the zonally asymmetric component of anomalous geopotential height (shading) and vertical and zonal components of anomalous Plumb wave activity flux (vector) averaged over 50°–70°N on day -5, 0, 5, and 10 for strong wave events under wQBO. (b) As in (a), but for strong wave events under eQBO. (c) differences between (a) and (b). Black lines are zero contours of the wave-1 component of anomalous geopotential height, indicating the vertical phase tilt of wave-1. Stippling in (a, b) denotes the regions where the shaded anomalies are significant at the 95% confidence level based on the two-sided Student's *t*-test. Stippling in (c) denotes 95% significant differences based on two-sided Welch's unequal variances *t*-test. The time evolution is smoothed by a 5-day running average. Day -5 represents the average between day -7 and day -3. To account for the smaller air density with decreasing pressure, the magnitude of the Plumb flux is scaled by $(1000/p)^{1/2}$, and geopotential height is scaled by $(p/1000)^{1/2}$, where p is pressure. The vertical component of the Plumb flux is also scaled by a factor of 200. See Figure 5.A.5 for the total (zonally asymmetric + zonal mean) field of anomalous geopotential height and absolute (anomalous + climatological) Plumb flux.

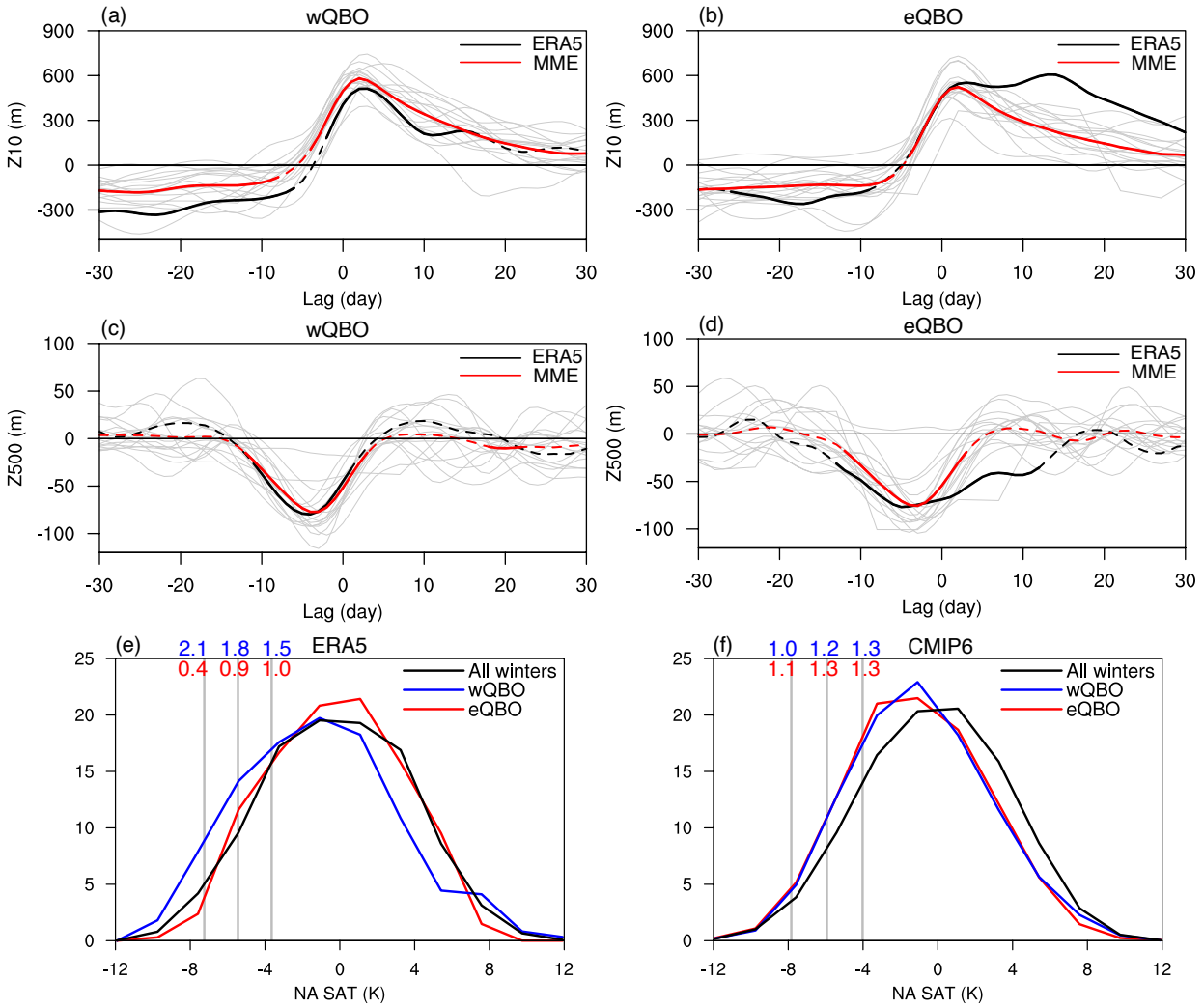

Figure 5.5.4: Evolution of circulation anomalies and risks of NA cold extremes linked to strong stratospheric wave events. (a–b) Composites of 10 hPa geopotential height anomalies averaged over northern North America (50°–90°N, 80°W–180°) for strong wave events under wQBO (a) and eQBO (b). (c–d) As in (a–b), but for 500 hPa geopotential height anomalies averaged over the northern North Pacific (50°–70°N, 150°E–130°W). ERA5 is denoted by black lines, the CMIP6 multi-model ensemble (MME) is in red, and individual models are in gray. Solid parts of the lines for ERA5 and CMIP6 MME indicate the anomalies significant at the 95% confidence level based on the two-sided Student's *t*-test. (e–f) Probability density function (PDF) of NA SAT (40°–70°N, 70°W–130°W) anomalies during days 5–20 following strong wave events under wQBO (blue lines) and eQBO (red lines) in ERA5 (e) and CMIP6 (f). The vertical gray lines denote -1, -1.5, and -2 SD of NA SAT anomalies in all the winter days, and the values in blue (red) depict the risk ratios of the exceedance frequency following strong wave events under wQBO (eQBO).

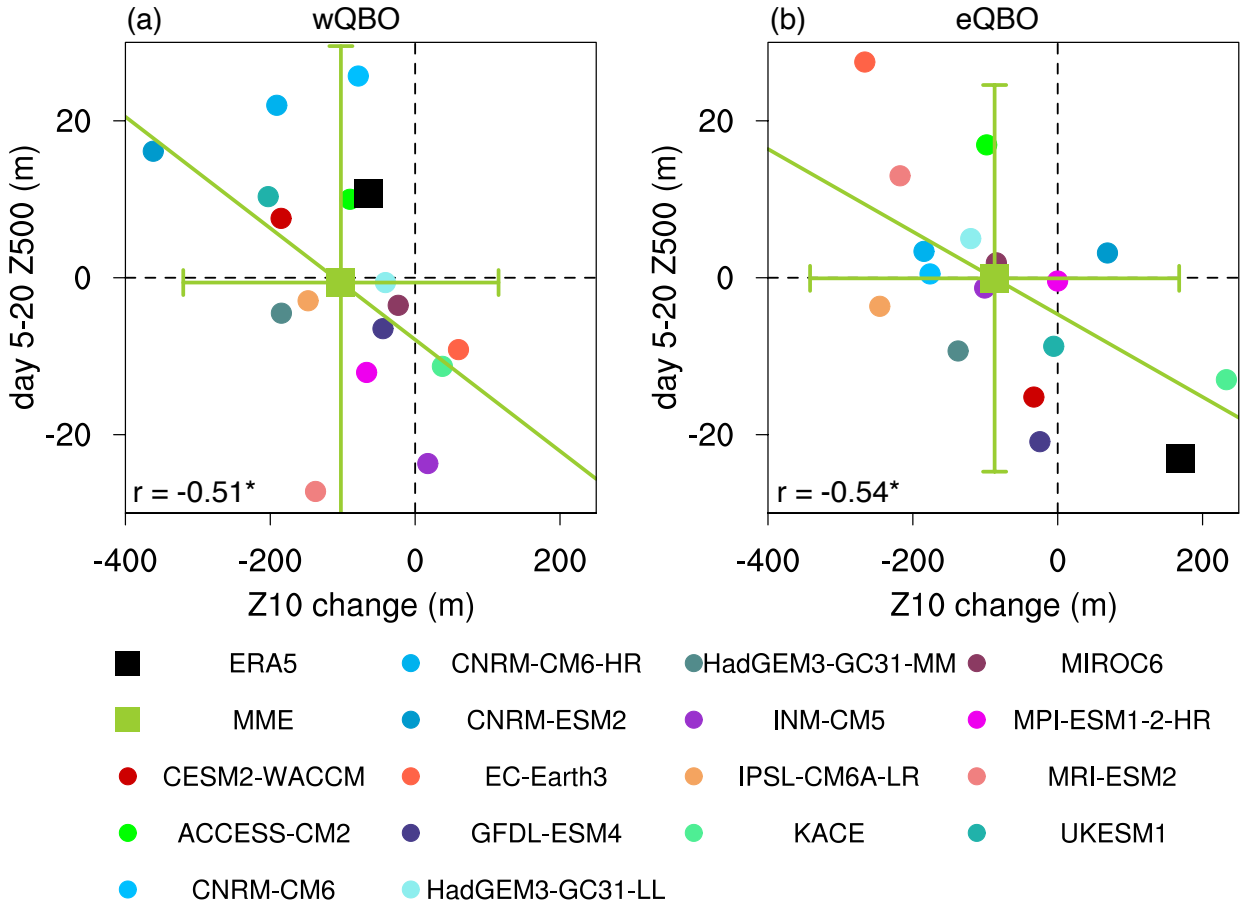

Figure 5.5.5: Intermodel scattering between stratospheric and tropospheric indices associated with strong stratospheric wave events. (a) 500 hPa northern North Pacific anomalies during days 5–20 versus the change of 10 hPa northern NA geopotential height anomalies between days 5–20 and days -5–5 under wQBO. (b) As in (a), but for eQBO. ERA5 is denoted as black squares, the CMIP6 MME means in green, and individual models noted in the legend. The colored lines show linear regressions for CMIP6, with correlation coefficients (r) given in the legend. The error bars show the ±2 SD of CMIP6. Asterisks denote coefficients significant at the 95% confidence level based on the two-sided Student's *t*-test.

5.A Appendices

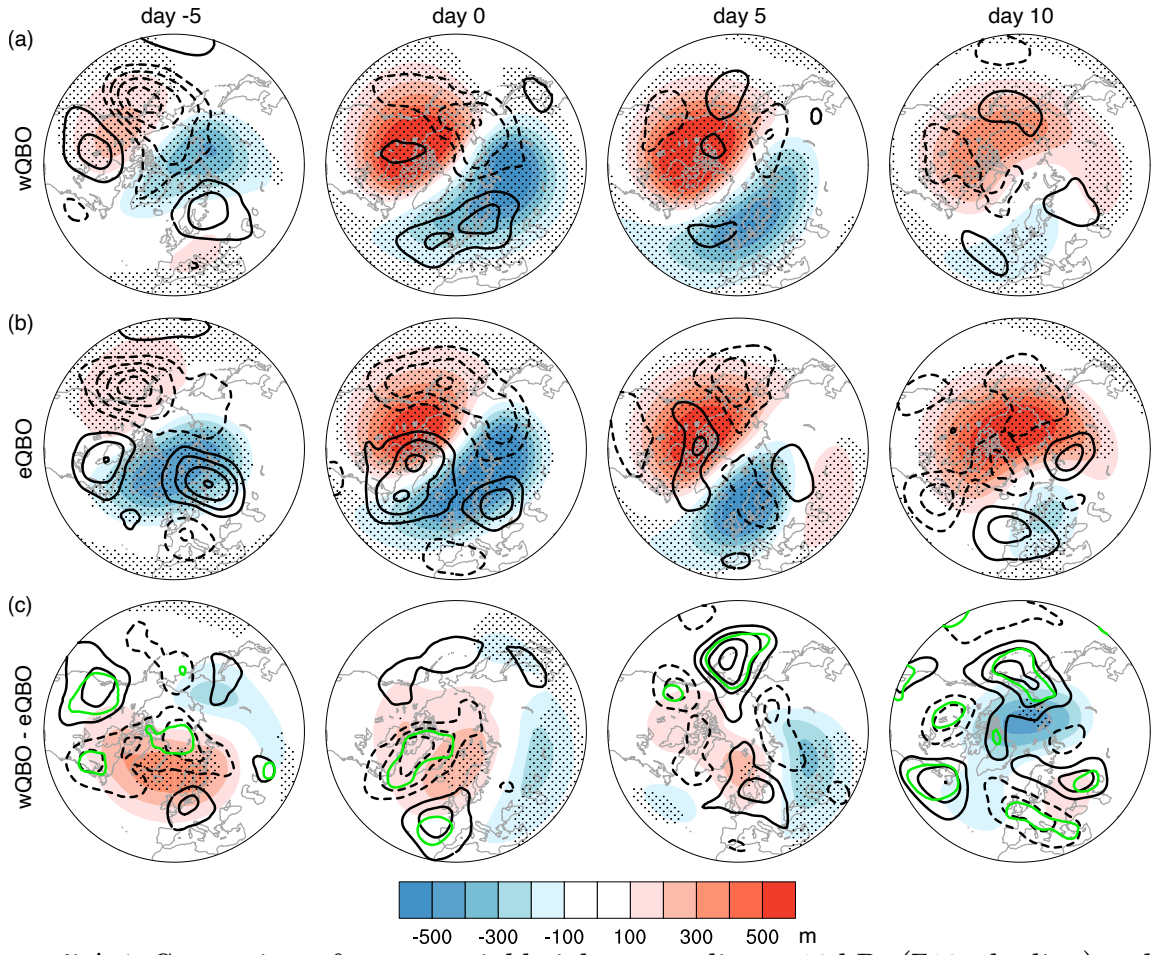

Figure 5.A.1: Composites of geopotential height anomalies at 10 hPa (Z10, shading) and 500 hPa (Z500, contours, 25 m interval) on day -5, 0, 5, and 10 for strong stratospheric wave events in ERA5 under wQBO (a) and eQBO (b). (c) differences between (a) and (b). Seasonal means have been removed before the composite. Stippling in (a, b) denotes the regions where the shaded anomalies are significant at the 95% confidence level based on the two-sided Student's *t*-test. Stippling and green contours in (c) denote 95% significant Z10 and Z500 differences based on two-sided Welch's unequal variances *t*-test. The time evolution is smoothed by a 5-day running average. Day -5 represents the average between day -7 and day -3.

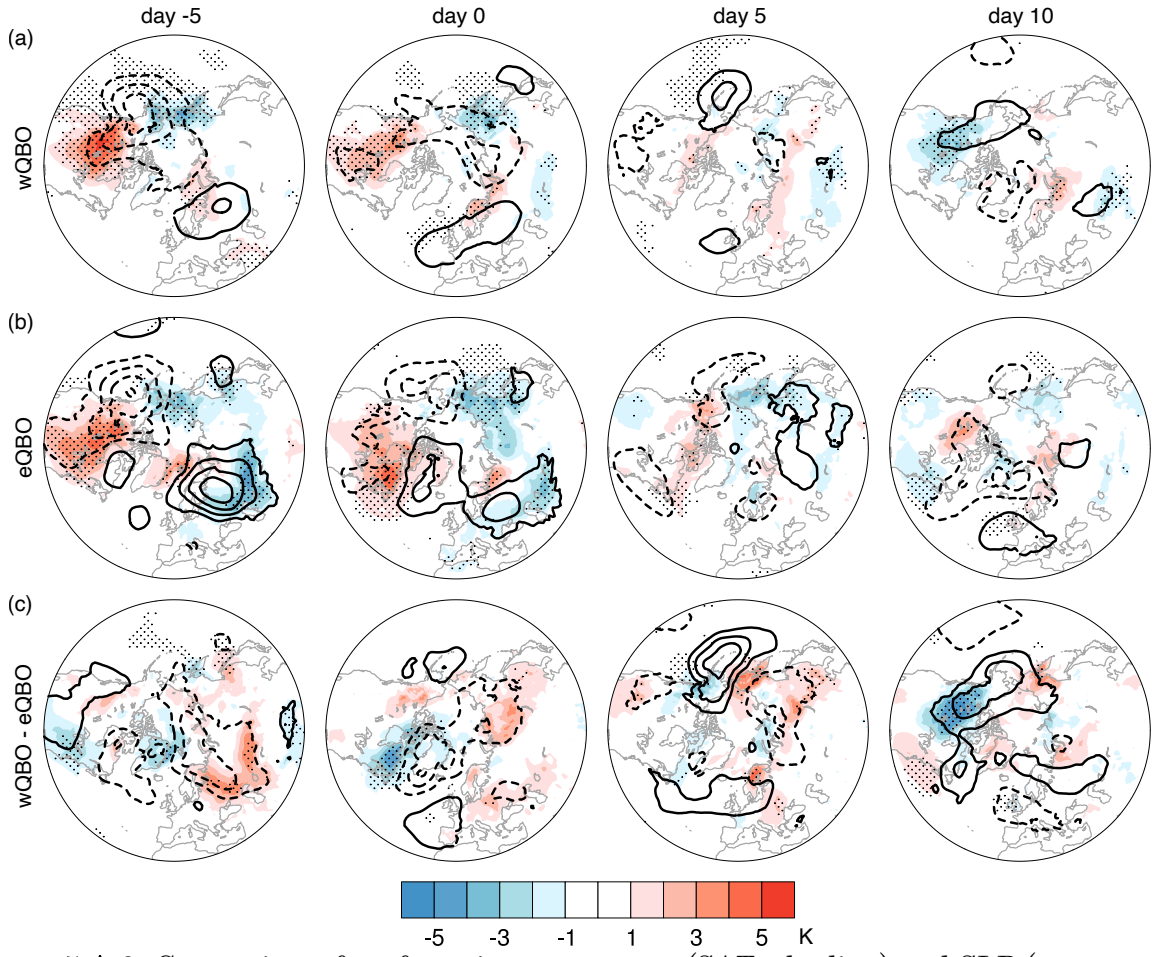

Figure 5.A.2: Composites of surface air temperature (SAT, shading) and SLP (contours, 2.5 hPa interval) on day -5, 0, 5, and 10 for strong stratospheric wave events in ERA5 under wQBO (a) and eQBO (b). (c) differences between (a) and (b). Seasonal means have been removed before the composite. Stippling in (a, b) denotes the regions where the shaded anomalies are significant at the 95% confidence level based on the two-sided Student's *t*-test. Stippling in (c) denotes 95% significant differences based on two-sided Welch's unequal variances *t*-test. The time evolution is smoothed by a 5-day running average. Day -5 represents the average between day -7 and day -3.

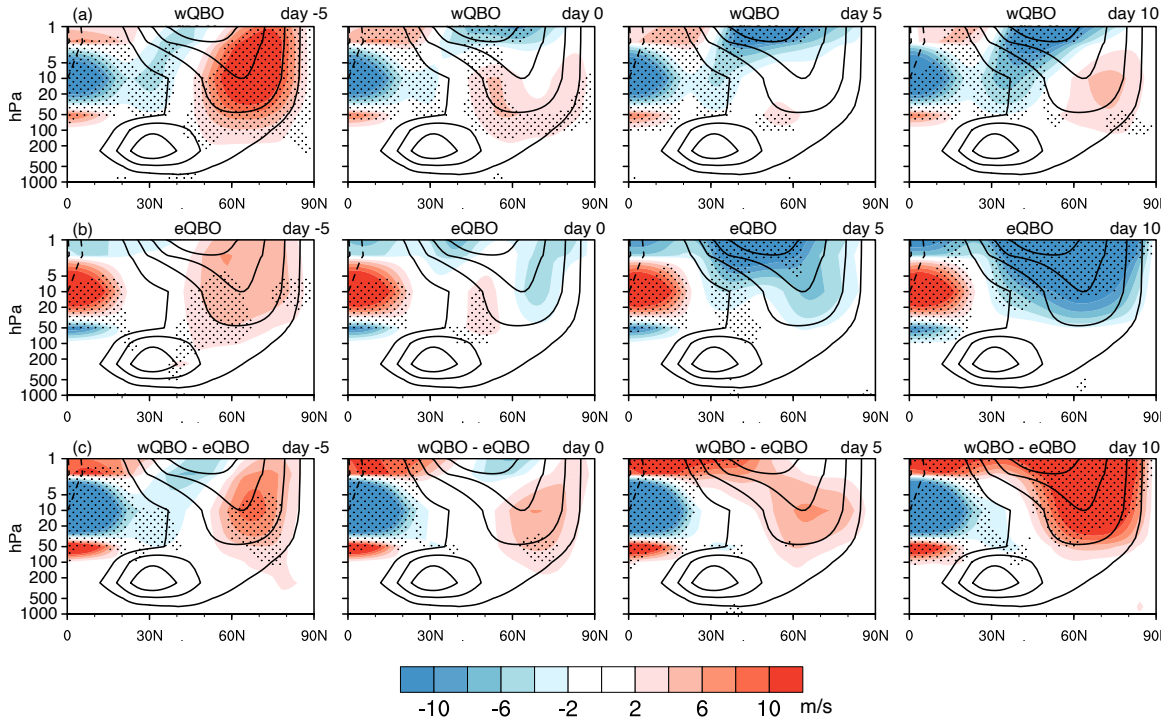

Figure 5.A.3: Composites of zonally averaged zonal wind (shading) on day -5, 0, 5, and 10 for strong stratospheric wave events in ERA5 under wQBO (a) and eQBO (b). (c) differences between (a) and (b). Black contours represent the climatology (CI: 10 m/s). Stippling in (a, b) denotes the regions where the shaded anomalies are significant at the 95% confidence level based on the two-sided Student's *t*-test. Stippling in (c) denotes 95% significant differences based on two-sided Welch's unequal variances *t*-test. The time evolution is smoothed by a 5-day running average. Day -5 represents the average between day -7 and day -3.

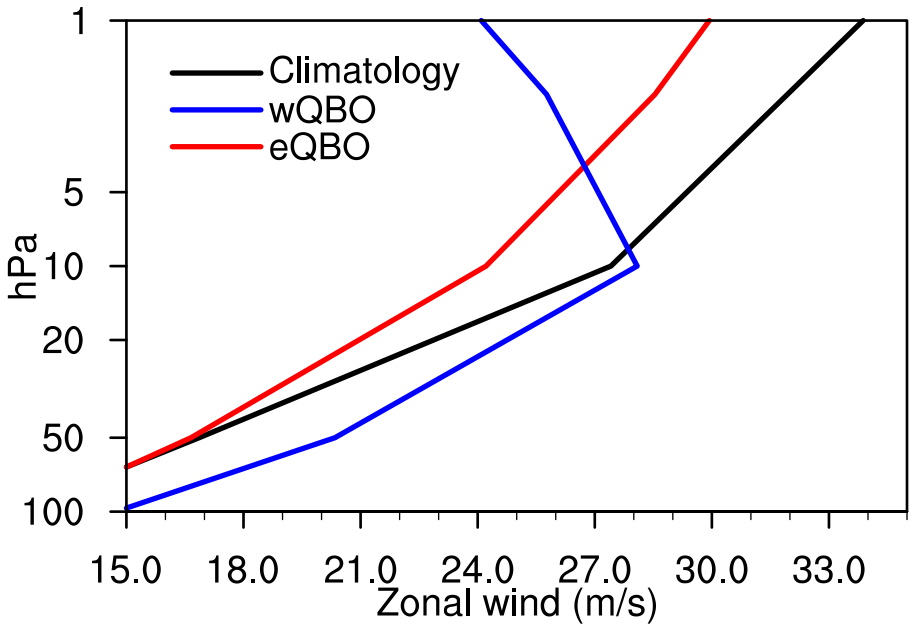

Figure 5.A.4: Absolute (anomalous + climatological) zonal wind profiles in the stratosphere averaged from day −2 to day 2.

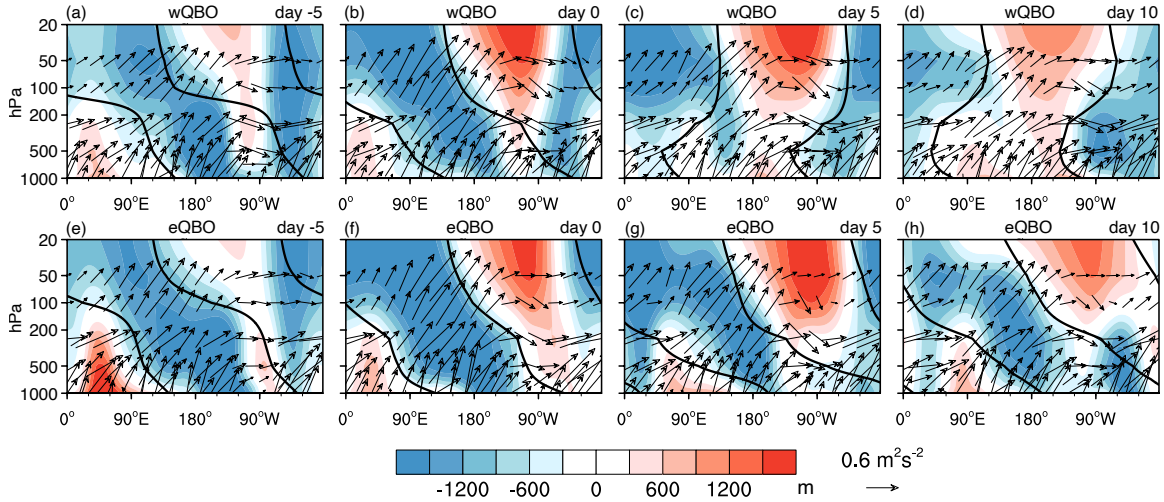

Figure 5.A.5: Vertical wave coupling associated with strong stratospheric wave events during wQBO (a–d) and eQBO (e–h) years in ERA5. As in Figures 5.5.3a–3b, but for composites of the total field of anomalous geopotential height (zonal mean + zonal asymmetry, shading) and the vertical and zonal components of absolute Plumb flux (climatology + anomalies, vector).

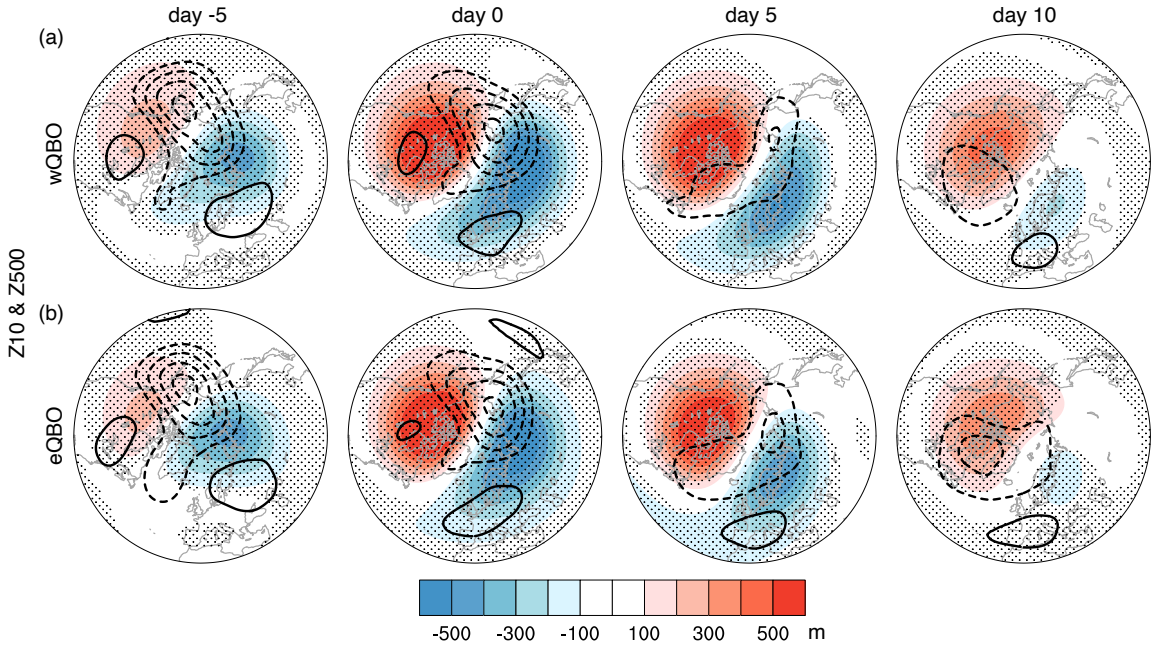

Figure 5.A.6: Strong stratospheric wave events during wQBO and eQBO years in CMIP6. As in Figures 5.5.1a–1b, but for composites in CMIP6 models.

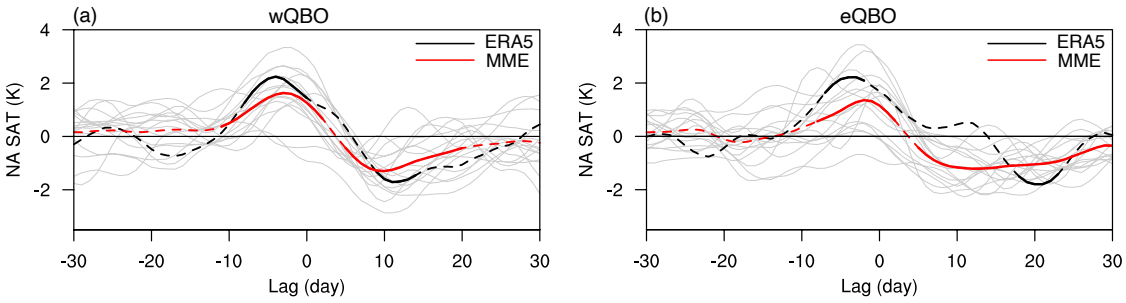

Figure 5.A.7: Evolution of NA SAT anomalies linked to strong stratospheric wave events during wQBO and eQBO years. As in Figures 5.5.4a–4b, but for NA SAT anomalies.

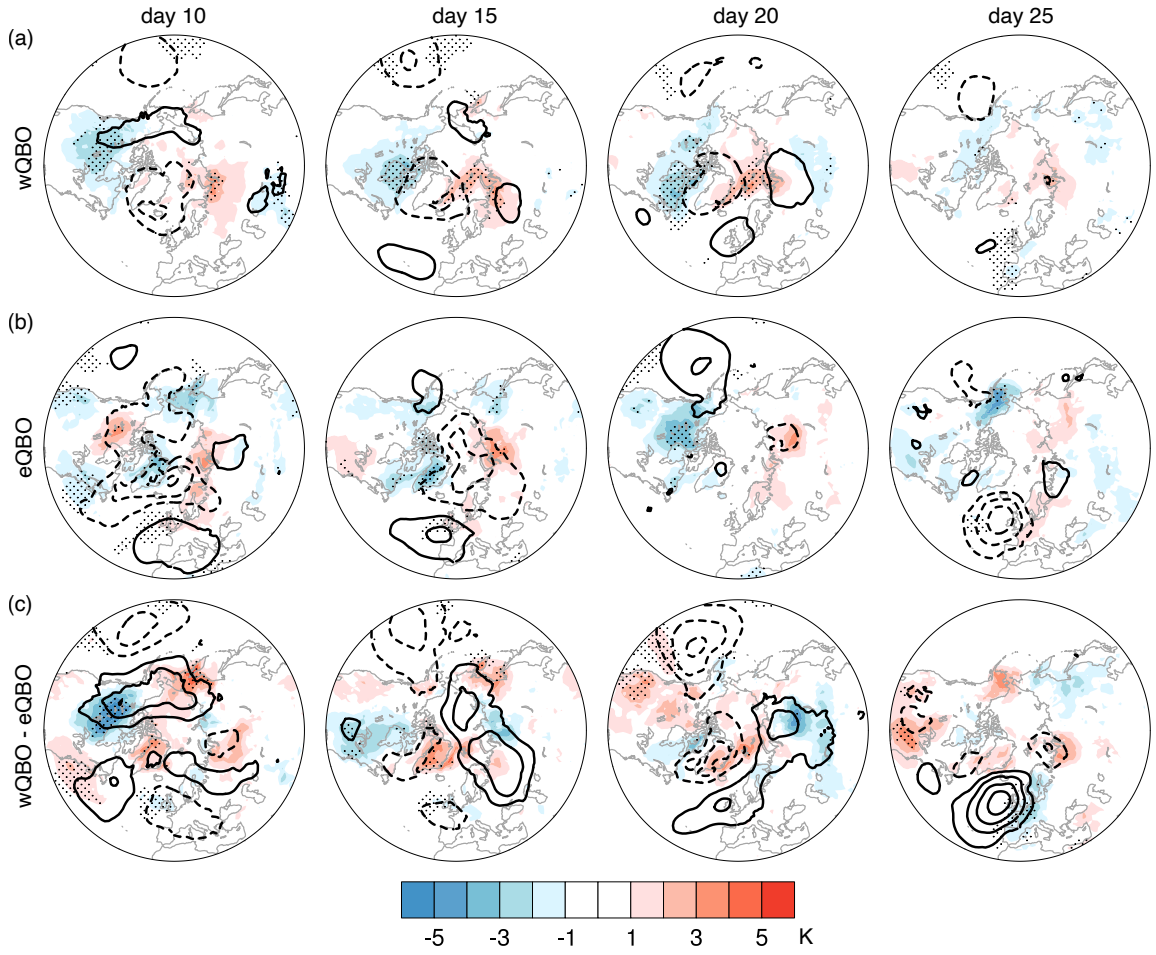

Figure 5.A.8: Composites of SAT (shading) and SLP (contours, 2.5 hPa interval) on day 10, 15, 20, and 25 for strong stratospheric wave events in ERA5 under wQBO (a) and eQBO (b). (c) differences between (a) and (b). Stippling in (a, b) denotes the regions where the shaded anomalies are significant at the 95% confidence level based on the two-sided Student's *t*-test. Stippling in (c) denotes 95% significant differences based on two-sided Welch's unequal variances *t*-test. The time evolution is smoothed by a 5-day running average.

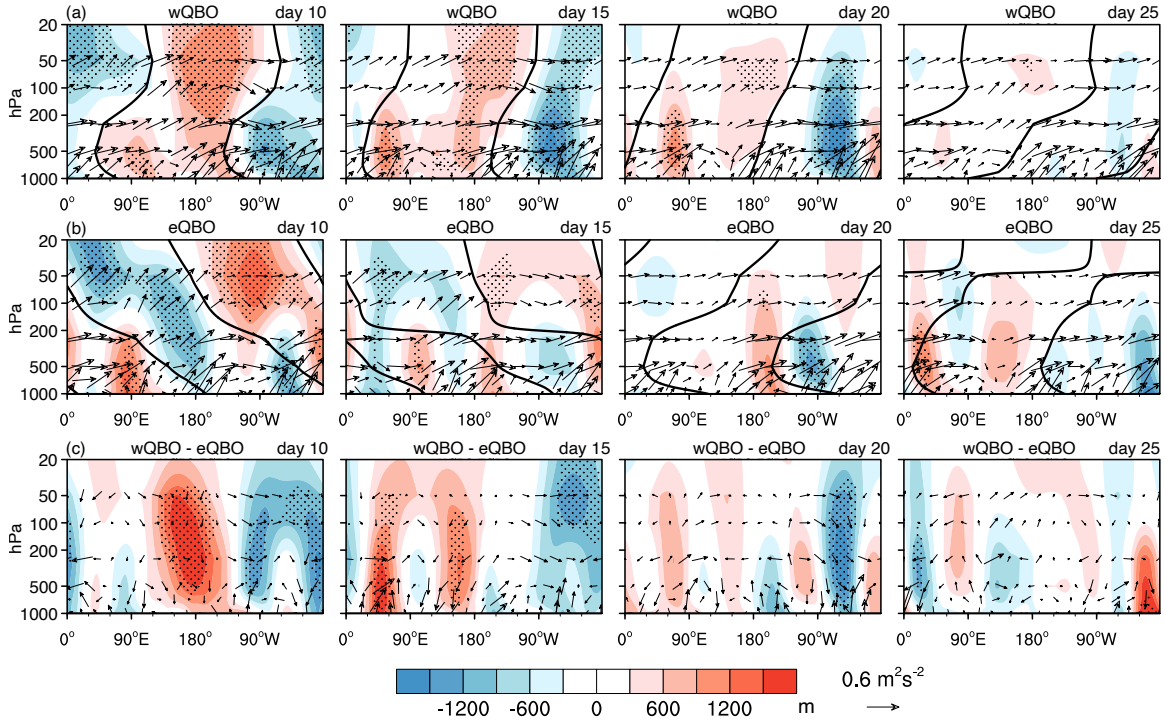

Figure 5.A.9: Vertical wave coupling associated with strong stratospheric wave events during wQBO and eQBO years in ERA5. As in Figure 5.5.3, but on day 10, 15, 20, and 25.

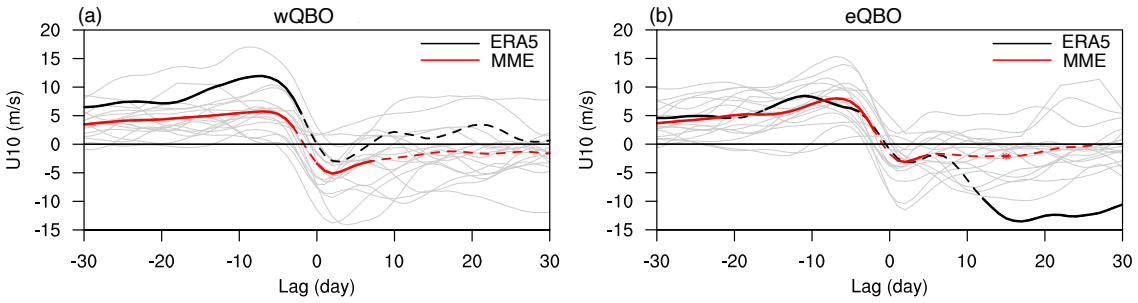

Figure 5.A.10: Evolution of 10 hPa zonal wind anomalies averaged over 60°–80°N linked to strong stratospheric wave events during wQBO and eQBO years. As in Figure 5.A.7, but for 10 hPa zonal wind anomalies.

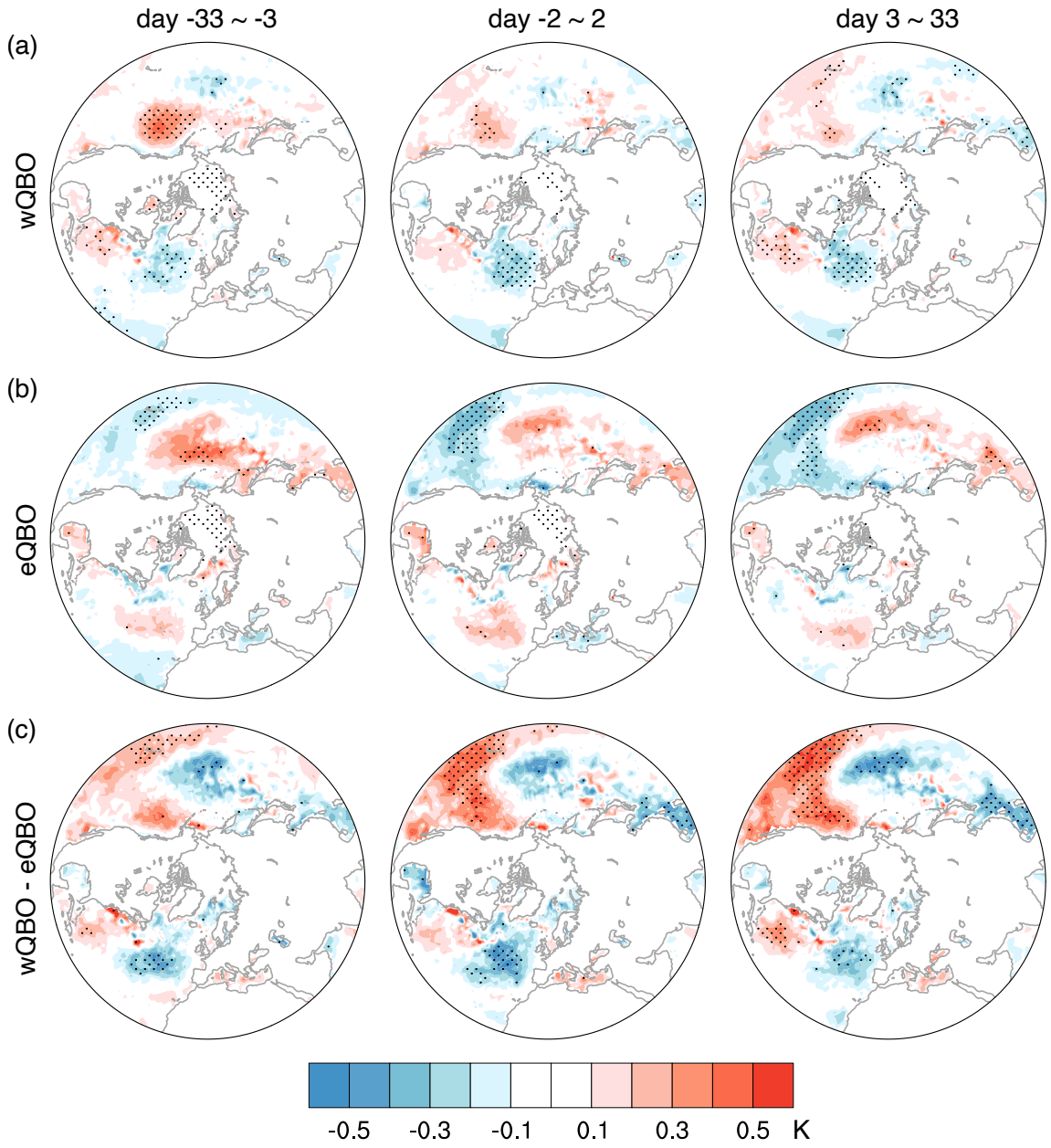

Figure 5.A.11: Composites of sea surface temperature (SST) anomalies (shading) during day -33– -3, day -2–2, and day 3–33 for strong stratospheric wave events in ERA5 under wQBO (a) and eQBO (b). (c) differences between (a) and (b). Stippling in (a, b) denotes the regions where the shaded anomalies are significant at the 95% confidence level based on the two-sided Student's *t*-test. Stippling in (c) denotes 95% significant differences based on two-sided Welch's unequal variances *t*-test.

Table 5.A.1: List of the QBO-resolving CMIP6 models used in this study and the frequency of eQBO and wQBO winters and strong stratospheric wave events.

Model	Ensemble Member	eQBO (events)	wQBO (events)
ACCESS-CM2	r1i1p1f1	29 (35)	31 (36)
CESM2-WACCM	r1i1p1f1	29 (29)	23 (23)
CNRM-CM6-1	r1i1p1f2	28 (29)	20 (14)
CNRM-CM6-1-HR	r1i1p1f2	28 (26)	21 (24)
CNRM-ESM2-1	r1i1p1f2	23 (20)	23 (22)
EC-Earth3	r1i1p1f1	29 (32)	26 (22)
GFDL-ESM4	r1i1p1f1	19 (22)	25 (23)
HadGEM3-GC31-LL	r1i1p1f3	27 (24)	33 (43)
HadGEM3-GC31-MM	r1i1p1f3	25 (32)	30 (41)
INM-CM5-0	r1i1p1f1	29 (31)	25 (20)
IPSL-CM6A-LR	r1i1p1f1	26 (20)	21 (19)
KACE-1-0-G	r1i1p1f1	27 (11)	31 (19)
MIROC6	r1i1p1f1	27 (36)	23 (26)
MPI-ESM1-2-HR	r1i1p1f1	24 (21)	22 (26)
MRI-ESM2-0	r1i1p1f1	26 (22)	34 (47)
UKESM1-0-LL	r1i1p1f2	25 (24)	34 (46)

CHAPTER 6

Conclusions and future work

6.1 Conclusions

In this dissertation, we study the linkage between stratospheric variability and North American (NA) surface air temperatures in boreal winter. Our discussions focus on the zonally asymmetric component of stratospheric circulation, namely the stratospheric planetary wave variability. Using reanalyses and a hierarchy of climate models, we show that extreme stratospheric wave activity is accompanied by subseasonal fluctuations between warm and cold spells over North America. Our study identifies strong stratospheric wave activity as a robust precursor for NA cold extremes on subseasonal timescales. Our findings shed light on the dynamical processes underlying extreme stratospheric wave variability, highlighting the role of vertical wave structure in stratosphere-troposphere coupling.

We start by introducing a simple measure to characterize stratospheric wave variability at 10 hPa using empirical orthogonal function (EOF) analysis in Chapter 2. We demonstrate that strong stratospheric wave activity is linked with positive NAO-like cold anomalies over North America in about 10 days through a deep planetary wave-1 structure, distinct from a weak polar vortex in terms of surface patterns and mechanisms. We further examine this linkage between stratospheric waves and NA temperature in models with different configurations, consistently finding more robust NA cooling following strong stratospheric wave activity than a weak polar vortex. These results suggest strong stratospheric wave activity acts as a better predictor for cold spells in the northern U.S. and Canada compared with a weak polar vortex on subseasonal timescales.

Chapter 2 highlights the importance of stratospheric wave variability in influencing tropospheric weather by comparing the zonally symmetric and asymmetric modes of winter stratospheric variability. This aspect of stratospheric variability has been overlooked as the previous literature mainly focused on the downward influence of the zonal mean circulation, namely the stratospheric polar vortex. Planetary waves are considered the driver of stratospheric zonal mean circulation but are seldom investigated for their downward influences. Our results show that extreme stratospheric wave activity is associated with a wave-1-like surface temperature pattern, distinct from the surface signals of an anomalous polar vortex. The analysis of vertical structure further illustrates that the coupling of extreme stratospheric wave activity with the troposphere acts on a shorter timescale than that of an anomalous polar vortex.

In Chapter 3, we first investigate the surface fingerprints of extreme stratospheric wave activity in observations and the historical simulations from 30 models in the Coupled Model Intercomparison Project Phase 6 (CMIP6). We find that both weak and strong wave activity is associated with cold anomalies over North America. However, only during strong stratospheric wave events do the stratospheric signals precede the surface coldness. Using nudging experiments, we attribute the observed NA coldness to the strong stratospheric wave activity since the nudging helps to isolate the contribution of the stratosphere. We further demonstrate in observations and nudging simulations that the vertical wave coupling between stratospheric and tropospheric waves is key to the observed transition from warm to cold weather during strong stratospheric wave events.

In Chapter 4, we systematically investigate the stratosphere-troposphere coupling of extreme stratospheric wave events and evaluate their representations in CMIP6 models. Aside from

quantifying the risk of cold and warm extremes associated with stratospheric wave events, we demonstrate the hydroclimate influences by showing the anomalous frequency of atmospheric river (AR) events during the life cycle of these events. We further examine the CMIP6 models and find that models with a degraded representation of stratospheric wave structure exhibit biases in the troposphere during strong stratospheric wave events. We also compare extreme stratospheric wave events with other extreme stratospheric events in the literature, demonstrating that extreme stratospheric wave events are distinct from other stratospheric events. This work suggests that the vertical coupling of extreme stratospheric wave activity should be evaluated in the model representation of stratosphere-troposphere coupling.

Lastly, in Chapter 5, we explore the potential role of the Quasi-biennial Oscillation (QBO) in the linkage between extreme stratospheric wave activity and NA temperature. By comparing strong wave events during the westerly phase (wQBO) with those during the easterly phase (eQBO), we find that the NA cooling signature following strong wave events depends on the QBO phase in the observation. In contrast to strong stratospheric wave events under wQBO, we show that strong wave events under eQBO do not change the cold risk over North America nor alter the vertical wave structure. We further examine this QBO modulation in QBO-resolving CMIP6 models, finding that the strong stratospheric wave events in models are largely insensitive to QBO phases, a possible bias in numerical models. These findings add to the growing body of research on the QBO's global impacts and reveal potential model deficits in representing stratospheric planetary waves.

Strong stratospheric wave events potentially act as a bridge connecting the QBO and NA cold extremes. The QBO is one of the most predictable modes of large-scale internal atmospheric

variability. Its influence has been investigated in many atmospheric phenomena for its potential to enhance their predictability, with the modulation of the polar vortex being one of the most well-known effects. However, as we have shown in Chapter 2, discussions centered around the polar vortex overlook the role of the zonally asymmetric component of the stratosphere. Our analysis shows an alternative pathway through strong stratospheric wave events that the QBO can influence cold extremes over North America.

The results of this dissertation robustly demonstrate the influence of extreme stratospheric wave activity on surface air temperature over North America, contributing to the discussion on the role of stratospheric variability in surface weather. Our measure of stratospheric wave activity is simple and readily applicable to reanalyses and numerical model outputs, which makes it appealing to model intercomparison and evaluation. The simplicity of the extreme stratospheric wave event definition also enables our consistent analysis across a wide range of datasets, providing compelling evidence for the proposed mechanism that strong stratospheric wave events contribute to NA surface cold extremes through vertical wave coupling.

6.2 Future work

This dissertation raises some interesting questions for future research on the role of stratospheric variability in surface air temperature. In Chapter 2, we demonstrate that extreme stratospheric wave events are distinct from anomalous polar vortex events regarding surface signals and mechanisms. However, the definitions of our wave events and polar vortex events are based on separate EOF analyses, which would inevitably introduce some uncertainty into the comparison. Future studies should employ a more holistic definition and approach to further investigate the linkages and differences between extreme wave events

and polar vortex events. A better understanding of these events may help to address the fundamental question of wave-mean-flow interaction in the stratosphere.

The findings in Chapter 3 shed light on the dynamical mechanism underlying the tropospheric influence of stratospheric waves and lend support to considering stratospheric wave activity in subseasonal predictions. Strong wave events potentially represent a window of opportunity during which North America gains additional predictability from strong stratospheric wave variability. However, despite all the statistical and dynamical evidence we have shown, the results are based on reanalysis and climate models without directly examining prediction systems. Additional work is warranted to investigate the predictability of extreme stratospheric wave events and their surface influences in subseasonal prediction models and Subseasonal to Seasonal Prediction (S2S) dataset (Domeisen, Butler, et al., 2020b; Domeisen, Grams, et al., 2020).

Chapter 4 shows that strong stratospheric wave events are associated with upper-level wind reversal and regionally negative eddy heat flux, indicating planetary waves are regionally reflected. However, the zonal mean eddy heat flux remains positive during the lifecycle of strong wave events, which does not meet the criteria of planetary wave reflection (e.g., Shaw et al., 2014). The dynamics of regional wave reflection remain unclear due to the limitation of the planetary wave theory that assumes a spatial separation between the wave structure and background flow (Plumb, 1985). Further analysis is required to understand the implication of regional signals of eddy heat flux.

Finally, future work should address the potential change in stratosphere-troposphere coupling under climate change. While the projections of the polar vortex strength diverge widely across climate models, most models project a robust eastward shift of the vortex

(Karpechko et al., 2022), suggesting a future change in the stratospheric wave structure. Given the importance of wave structure in the vertical coupling, extreme stratospheric wave events and their surface linkages would also likely change under global warming. These potential future stratospheric changes would have profound implications for regional climate projections.

Bibliography

Afargan-Gerstman, H., & Domeisen, D. I. V. (2020). Pacific Modulation of the North Atlantic Storm Track Response to Sudden Stratospheric Warming Events. *Geophysical Research Letters*, *47*(2), e2019GL085007. https://doi.org/10.1029/2019GL085007

Afargan-Gerstman, H., Jiménez-Esteve, B., & Domeisen, D. I. V. (2022). On the Relative Importance of Stratospheric and Tropospheric Drivers for the North Atlantic Jet Response to Sudden Stratospheric Warming Events. *Journal of Climate*, *35*(19), 2851–2865. https://doi.org/10.1175/JCLI-D-21-0680.1

Albers, J. R., Newman, M., Hoell, A., Breeden, M. L., Wang, Y., & Lou, J. (2022). The February 2021 Cold Air Outbreak in the United States: A Subseasonal Forecast of Opportunity. *Bulletin of the American Meteorological Society*, *103*(12), E2887–E2904. https://doi.org/10.1175/BAMS-D-21-0266.1

Andrews, M. B., Knight, J. R., Scaife, A. A., Lu, Y., Wu, T., Gray, L. J., & Schenzinger, V. (2019). Observed and Simulated Teleconnections Between the Stratospheric Quasi-Biennial Oscillation and Northern Hemisphere Winter Atmospheric Circulation. *Journal of Geophysical Research: Atmospheres*, *124*(3), 1219–1232. https://doi.org/10.1029/2018JD029368

Anstey, J. A., Osprey, S. M., Alexander, J., Baldwin, M. P., Butchart, N., Gray, L., et al. (2022). Impacts, processes and projections of the quasi-biennial oscillation. *Nature Reviews Earth & Environment*, *3*(9), 588–603. https://doi.org/10.1038/s43017-022-00323-7

Anstey, J. A., Simpson, I. R., Richter, J. H., Naoe, H., Taguchi, M., Serva, F., et al. (2022). Teleconnections of the Quasi-Biennial Oscillation in a multi-model ensemble of QBO-resolving models. *Quarterly Journal of the Royal Meteorological Society*, *148*(744), 1568–1592. https://doi.org/10.1002/qj.4048

Baek, S. H., Battalio, J. M., & Lora, J. M. (2023). Atmospheric River Variability Over the Last Millennium Driven by Annular Modes. *AGU Advances*, *4*(1), e2022AV000834. https://doi.org/10.1029/2022AV000834

Baldwin, M. P., & Dunkerton, T. J. (2001). Stratospheric Harbingers of Anomalous Weather Regimes. *Science*, *294*(5542), 581–584. https://doi.org/10.1126/science.1063315

Baldwin, M. P., & Thompson, D. W. J. (2009). A critical comparison of stratosphere-troposphere coupling indices. *Quarterly Journal of the Royal Meteorological Society*, *135*(644), 1661–1672. https://doi.org/10.1002/qj.479

Baldwin, M. P., Stephenson, D. B., David W. J. Thompson, Dunkerton, T. J., Charlton, A. J., & O'Neill, A. (2003). Stratospheric Memory and Skill of Extended-Range Weather Forecasts. *Science*, *301*(5633), 636–640. https://doi.org/10.1126/science.1087143

Baldwin, M. P., Ayarzagüena, B., Birner, T., Butchart, N., Butler, A. H., Charlton-Perez, A. J., et al. (2021). Sudden Stratospheric Warmings. *Reviews of Geophysics*, *59*(1). https://doi.org/10.1029/2020RG000708

Blackport, R., Screen, J. A., van der Wiel, K., & Bintanja, R. (2019). Minimal influence of reduced Arctic sea ice on coincident cold winters in mid-latitudes. *Nature Climate Change*, *9*(9), 697–704. https://doi.org/10.1038/s41558-019-0551-4

Bolinger, R. A., Brown, V. M., Fuhrmann, C. M., Gleason, K. L., Joyner, T. A., Keim, B. D., et al. (2022). An assessment of the extremes and impacts of the February 2021 South-Central U.S. Arctic outbreak, and how climate services can help. *Weather and Climate Extremes*, *36*, 100461. https://doi.org/10.1016/j.wace.2022.100461

Bretherton, C. S., Widmann, M., Dymnikov, V. P., Wallace, J. M., & Bladé, I. (1999). The Effective Number of Spatial Degrees of Freedom of a Time-Varying Field. *Journal of Climate*, *12*(7), 1990–2009. https://doi.org/10.1175/1520-0442(1999)012<1990:TENOSD>2.0.CO;2

Butler, A. H., & Polvani, L. M. (2011). El Niño, La Niña, and stratospheric sudden warmings: A reevaluation in light of the observational record. *Geophysical Research Letters*, *38*(13). https://doi.org/10.1029/2011GL048084

Butler, A. H., Polvani, L. M., & Deser, C. (2014). Separating the stratospheric and tropospheric pathways of El Niño–Southern Oscillation teleconnections. *Environmental Research Letters*, *9*(2), 024014. https://doi.org/10.1088/1748-9326/9/2/024014

Butler, A. H., Arribas, A., Athanassiadou, M., Baehr, J., Calvo, N., Charlton-Perez, A., et al. (2016). The Climate-system Historical Forecast Project: do stratosphere-resolving models make better seasonal climate predictions in boreal winter? *Quarterly Journal of the Royal Meteorological Society*, *142*(696), 1413–1427. https://doi.org/10.1002/qj.2743

Butler, A. H., Sjoberg, J. P., Seidel, D. J., & Rosenlof, K. H. (2017). A sudden stratospheric warming compendium. *Earth System Science Data*, *9*(1), 63–76. https://doi.org/10.5194/essd-9-63-2017

Cámara, A. de la, Albers, J. R., Birner, T., Garcia, R. R., Hitchcock, P., Kinnison, D. E., & Smith, A. K. (2017). Sensitivity of Sudden Stratospheric Warmings to Previous Stratospheric Conditions. *Journal of the Atmospheric Sciences*, *74*(9), 2857–2877. https://doi.org/10.1175/JAS-D-17-0136.1

Charlton, A. J., & Polvani, L. M. (2007). A New Look at Stratospheric Sudden Warmings. Part I: Climatology and Modeling Benchmarks. *Journal of Climate*, *20*(3), 449–469. https://doi.org/10.1175/JCLI3996.1

Charlton, A. J., Polvani, L. M., Perlwitz, J., Sassi, F., Manzini, E., Shibata, K., et al. (2007). A New Look at Stratospheric Sudden Warmings. Part II: Evaluation of Numerical

Model Simulations. *Journal of Climate*, *20*(3), 470–488. https://doi.org/10.1175/JCLI3994.1

Charlton-Perez, A. J., Baldwin, M. P., Birner, T., Black, R. X., Butler, A. H., Calvo, N., et al. (2013). On the lack of stratospheric dynamical variability in low-top versions of the CMIP5 models. *Journal of Geophysical Research: Atmospheres*, *118*(6), 2494–2505. https://doi.org/10.1002/jgrd.50125

Charlton-Perez, A. J., Ferranti, L., & Lee, R. W. (2018). The influence of the stratospheric state on North Atlantic weather regimes. *Quarterly Journal of the Royal Meteorological Society*, *144*(713), 1140–1151. https://doi.org/10.1002/qj.3280

Charlton-Perez, A. J., Aldridge, R. W., Grams, C. M., & Lee, R. (2019). Winter pressures on the UK health system dominated by the Greenland Blocking weather regime. *Weather and Climate Extremes*, *25*, 100218. https://doi.org/10.1016/j.wace.2019.100218

Charney, J. G., & Drazin, P. G. (1961). Propagation of planetary-scale disturbances from the lower into the upper atmosphere. *Journal of Geophysical Research (1896-1977)*, *66*(1), 83–109. https://doi.org/10.1029/JZ066i001p00083

Cohen, J., Agel, L., Barlow, M., Garfinkel, C. I., & White, I. (2021). Linking Arctic variability and change with extreme winter weather in the United States. *Science*, *373*(6559), 1116–1121. https://doi.org/10.1126/science.abi9167

Cohen, J., Agel, L., Barlow, M., & Entekhabi, D. (2023). No detectable trend in mid-latitude cold extremes during the recent period of Arctic amplification. *Communications Earth & Environment*, *4*(1), 1–9. https://doi.org/10.1038/s43247-023-01008-9

Collimore, C. C., Martin, D. W., Hitchman, M. H., Huesmann, A., & Waliser, D. E. (2003). On The Relationship between the QBO and Tropical Deep Convection. *Journal of Climate*, *16*(15), 2552–2568. https://doi.org/10.1175/1520-0442(2003)016<2552:OTRBTQ>2.0.CO;2

Danabasoglu, G., Lamarque, J.-F., Bacmeister, J., Bailey, D. A., DuVivier, A. K., Edwards, J., et al. (2020). The Community Earth System Model Version 2 (CESM2). *Journal of Advances in Modeling Earth Systems*, *12*(2), e2019MS001916. https://doi.org/10.1029/2019MS001916

Davies, H. C. (1981). An Interpretation of Sudden Warmings In Terms of Potential vorticity. *Journal of the Atmospheric Sciences*, *38*(2), 427–445. https://doi.org/10.1175/1520-0469(1981)038<0427:AIOSWI>2.0.CO;2

Davis, N. A., Richter, J. H., Glanville, A. A., Edwards, J., & LaJoie, E. (2022). Limited surface impacts of the January 2021 sudden stratospheric warming. *Nature Communications*, *13*(1), 1136. https://doi.org/10.1038/s41467-022-28836-1

Dee, D. P., Uppala, S. M., Simmons, A. J., Berrisford, P., Poli, P., Kobayashi, S., et al. (2011). The ERA-Interim reanalysis: configuration and performance of the data assimilation

system. *Quarterly Journal of the Royal Meteorological Society*, *137*(656), 553–597. https://doi.org/10.1002/qj.828

Ding, X., Chen, G., Sun, L., & Zhang, P. (2022). Distinct North American Cooling Signatures Following the Zonally Symmetric and Asymmetric Modes of Winter Stratospheric Variability. *Geophysical Research Letters*, *49*(6), e2021GL096076. https://doi.org/10.1029/2021GL096076

Ding, X., Chen, G., Zhang, P., Domeisen, D. I. V., & Orbe, C. (2023). Extreme stratospheric wave activity as harbingers of cold events over North America. *Communications Earth & Environment*, *4*(1), 187. https://doi.org/10.1038/s43247-023-00845-y

Ding, X., Chen, G., & Ma, W. (2023). Stratosphere-Troposphere Coupling of Extreme Stratospheric Wave Activity in CMIP6 Models. *Journal of Geophysical Research: Atmospheres*, *128*(16), e2023JD038811. https://doi.org/10.1029/2023JD038811

Domeisen, D. I. V. (2019). Estimating the Frequency of Sudden Stratospheric Warming Events From Surface Observations of the North Atlantic Oscillation. *Journal of Geophysical Research: Atmospheres*, *124*(6), 3180–3194. https://doi.org/10.1029/2018JD030077

Domeisen, D. I. V., & Butler, A. H. (2020). Stratospheric drivers of extreme events at the Earth's surface. *Communications Earth & Environment*, *1*(1), 1–8. https://doi.org/10.1038/s43247-020-00060-z

Domeisen, D. I. V., Butler, A. H., Fröhlich, K., Bittner, M., Müller, W. A., & Baehr, J. (2015). Seasonal Predictability over Europe Arising from El Niño and Stratospheric Variability in the MPI-ESM Seasonal Prediction System. *Journal of Climate*, *28*(1), 256–271. https://doi.org/10.1175/JCLI-D-14-00207.1

Domeisen, D. I. V., Garfinkel, C. I., & Butler, A. H. (2019). The Teleconnection of El Niño Southern Oscillation to the Stratosphere. *Reviews of Geophysics*, *57*(1), 5–47. https://doi.org/10.1029/2018RG000596

Domeisen, D. I. V., Grams, C. M., & Papritz, L. (2020). The role of North Atlantic–European weather regimes in the surface impact of sudden stratospheric warming events. *Weather and Climate Dynamics*, *1*(2), 373–388. https://doi.org/10.5194/wcd-1-373-2020

Domeisen, D. I. V., Butler, A. H., Charlton-Perez, A. J., Ayarzagüena, B., Baldwin, M. P., Dunn-Sigouin, E., et al. (2020a). The Role of the Stratosphere in Subseasonal to Seasonal Prediction: 1. Predictability of the Stratosphere. *Journal of Geophysical Research: Atmospheres*, *125*(2), e2019JD030920. https://doi.org/10.1029/2019JD030920

Domeisen, D. I. V., Butler, A. H., Charlton-Perez, A. J., Ayarzagüena, B., Baldwin, M. P., Dunn-Sigouin, E., et al. (2020b). The Role of the Stratosphere in Subseasonal to Seasonal Prediction: 2. Predictability Arising From Stratosphere-Troposphere

Coupling. *Journal of Geophysical Research: Atmospheres*, *125*(2), e2019JD030923. https://doi.org/10.1029/2019JD030923

Doss-Gollin, J., Farnham, D. J., Lall, U., & Modi, V. (2021). How unprecedented was the February 2021 Texas cold snap? *Environmental Research Letters*, *16*(6), 064056. https://doi.org/10.1088/1748-9326/ac0278

Dunn-Sigouin, E., & Shaw, T. A. (2015). Comparing and contrasting extreme stratospheric events, including their coupling to the tropospheric circulation. *Journal of Geophysical Research: Atmospheres*, *120*(4), 1374–1390. https://doi.org/10.1002/2014JD022116

Dunn-Sigouin, E., & Shaw, T. A. (2018). Dynamics of Extreme Stratospheric Negative Heat Flux Events in an Idealized Model. *Journal of the Atmospheric Sciences*, *75*(10), 3521–3540. https://doi.org/10.1175/JAS-D-17-0263.1

Elsbury, D., Peings, Y., & Magnusdottir, G. (2021a). CMIP6 Models Underestimate the Holton-Tan Effect. *Geophysical Research Letters*, *48*(24). https://doi.org/10.1029/2021GL094083

Elsbury, D., Peings, Y., & Magnusdottir, G. (2021b). Variation in the Holton–Tan effect by longitude. *Quarterly Journal of the Royal Meteorological Society*, *147*(736), 1767–1787. https://doi.org/10.1002/qj.3993

Garfinkel, C. I., Hartmann, D. L., & Sassi, F. (2010). Tropospheric Precursors of Anomalous Northern Hemisphere Stratospheric Polar Vortices. *Journal of Climate*, *23*(12), 3282–3299. https://doi.org/10.1175/2010JCLI3010.1

Garfinkel, C. I., Son, S.-W., Song, K., Aquila, V., & Oman, L. D. (2017). Stratospheric variability contributed to and sustained the recent hiatus in Eurasian winter warming. *Geophysical Research Letters*, *44*(1), 374–382. https://doi.org/10.1002/2016GL072035

Garfinkel, C. I., White, I., Gerber, E. P., Jucker, M., & Erez, M. (2020). The Building Blocks of Northern Hemisphere Wintertime Stationary Waves. *Journal of Climate*, *33*(13), 5611–5633. https://doi.org/10.1175/JCLI-D-19-0181.1

Gerber, E. P., & Polvani, L. M. (2009). Stratosphere–Troposphere Coupling in a Relatively Simple AGCM: The Importance of Stratospheric Variability. *Journal of Climate*, *22*(8), 1920–1933. https://doi.org/10.1175/2008JCLI2548.1

Gerber, E. P., Baldwin, M. P., Akiyoshi, H., Austin, J., Bekki, S., Braesicke, P., et al. (2010). Stratosphere-troposphere coupling and annular mode variability in chemistry-climate models. *Journal of Geophysical Research*, *115*, D00M06. https://doi.org/10.1029/2009JD013770

Gettelman, A., Mills, M. J., Kinnison, D. E., Garcia, R. R., Smith, A. K., Marsh, D. R., et al. (2019). The Whole Atmosphere Community Climate Model Version 6 (WACCM6). *Journal of Geophysical Research: Atmospheres*, *124*(23), 12380–12403. https://doi.org/10.1029/2019JD030943

Gray, L. J., Anstey, J. A., Kawatani, Y., Lu, H., Osprey, S., & Schenzinger, V. (2018). Surface impacts of the Quasi Biennial Oscillation. *Atmospheric Chemistry and Physics*, *18*(11), 8227–8247. https://doi.org/10.5194/acp-18-8227-2018

Greatbatch, R. J., Gollan, G., Jung, T., & Kunz, T. (2012). Factors influencing Northern Hemisphere winter mean atmospheric circulation anomalies during the period 1960/61 to 2001/02. *Quarterly Journal of the Royal Meteorological Society*, *138*(669), 1970–1982. https://doi.org/10.1002/qj.1947

Guan, B., & Waliser, D. E. (2015). Detection of atmospheric rivers: Evaluation and application of an algorithm for global studies. *Journal of Geophysical Research: Atmospheres*, *120*(24), 12514–12535. https://doi.org/10.1002/2015JD024257

Guan, W., Jiang, X., Ren, X., Chen, G., Lin, P., & Lin, H. (2020). The Leading Intraseasonal Variability Mode of Wintertime Surface Air Temperature over the North American Sector. *Journal of Climate*, *33*(21), 9287–9306. https://doi.org/10.1175/JCLI-D-20-0096.1

Harnik, N. (2009). Observed stratospheric downward reflection and its relation to upward pulses of wave activity. *Journal of Geophysical Research: Atmospheres*, *114*(D8), 2008JD010493. https://doi.org/10.1029/2008JD010493

Harnik, N., Messori, G., Caballero, R., & Feldstein, S. B. (2016). The Circumglobal North American wave pattern and its relation to cold events in eastern North America. *Geophysical Research Letters*, *43*(20), 11,015-11,023. https://doi.org/10.1002/2016GL070760

Hartmann, D. L. (2015). Pacific sea surface temperature and the winter of 2014. *Geophysical Research Letters*, *42*(6), 1894–1902. https://doi.org/10.1002/2015GL063083

Hersbach, H., Bell, B., Berrisford, P., Hirahara, S., Horányi, A., Muñoz-Sabater, J., et al. (2020). The ERA5 global reanalysis. *Quarterly Journal of the Royal Meteorological Society*, *146*(730), 1999–2049. https://doi.org/10.1002/qj.3803

Hitchcock, P., & Simpson, I. R. (2014). The Downward Influence of Stratospheric Sudden Warmings. *Journal of the Atmospheric Sciences*, *71*(10), 3856–3876. https://doi.org/10.1175/JAS-D-14-0012.1

Holton, J. R., & Mass, C. (1976). Stratospheric Vacillation Cycles. *Journal of the Atmospheric Sciences*, *33*(11), 2218–2225. https://doi.org/10.1175/1520-0469(1976)033<2218:SVC>2.0.CO;2

Holton, J. R., & Tan, H.-C. (1980). The Influence of the Equatorial Quasi-Biennial Oscillation on the Global Circulation at 50 mb. *Journal of the Atmospheric Sciences*, *37*(10), 2200–2208. https://doi.org/10.1175/1520-0469(1980)037<2200:TIOTEQ>2.0.CO;2

Hou, K., Zhang, L., Xu, X., Yang, F., Chen, B., & Hu, W. (2022). Ambient temperatures associated with increased risk of motor vehicle crashes in New York and Chicago.

Science of The Total Environment, *830*, 154731. https://doi.org/10.1016/j.scitotenv.2022.154731

Huang, J., Tian, W., Gray, L. J., Zhang, J., Li, Y., Luo, J., & Tian, H. (2018). Preconditioning of Arctic Stratospheric Polar Vortex Shift Events. *Journal of Climate*, *31*(14), 5417–5436. https://doi.org/10.1175/JCLI-D-17-0695.1

Huang, J., Hitchcock, P., Maycock, A. C., McKenna, C. M., & Tian, W. (2021). Northern hemisphere cold air outbreaks are more likely to be severe during weak polar vortex conditions. *Communications Earth & Environment*, *2*(1), 147. https://doi.org/10.1038/s43247-021-00215-6

Huang, W. T. K., Charlton-Perez, A., Lee, R. W., Neal, R., Sarran, C., & Sun, T. (2020). Weather regimes and patterns associated with temperature-related excess mortality in the UK: a pathway to sub-seasonal risk forecasting. *Environmental Research Letters*, *15*(12), 124052. https://doi.org/10.1088/1748-9326/abcbba

Huffman, G. J., Bolvin, D. T., Braithwaite, D., Hsu, K., Joyce, R., Kidd, C., et al. (2014). Integrated Multi-satellitE Retrievals for GPM (IMERG), version 4.4. *NASA's Precipitation Processing Center*. https://doi.org/ftp://arthurhou.pps.eosdis.nasa.gov/gpmdata/

Hurrell, J. W. (1995). Decadal Trends in the North Atlantic Oscillation: Regional Temperatures and Precipitation. *Science*. Retrieved from https://www.science.org/doi/abs/10.1126/science.269.5224.676

Johnson, N. C., Collins, D. C., Feldstein, S. B., L'Heureux, M. L., & Riddle, E. E. (2014). Skillful Wintertime North American Temperature Forecasts out to 4 Weeks Based on the State of ENSO and the MJO. *Weather and Forecasting*, *29*(1), 23–38. https://doi.org/10.1175/WAF-D-13-00102.1

Johnson, N. C., Xie, S.-P., Kosaka, Y., & Li, X. (2018). Increasing occurrence of cold and warm extremes during the recent global warming slowdown. *Nature Communications*, *9*(1), 1724. https://doi.org/10.1038/s41467-018-04040-y

Karpechko, A. Yu., Hitchcock, P., Peters, D. H. W., & Schneidereit, A. (2017). Predictability of downward propagation of major sudden stratospheric warmings: Downward Propagation of SSWs. *Quarterly Journal of the Royal Meteorological Society*, *143*(704), 1459–1470. https://doi.org/10.1002/qj.3017

Karpechko, A. Yu., Tyrrell, N. L., & Rast, S. (2021). Sensitivity of QBO teleconnection to model circulation biases. *Quarterly Journal of the Royal Meteorological Society*, *147*(737), 2147–2159. https://doi.org/10.1002/qj.4014

Karpechko, A. Yu., Afargan-Gerstman, H., Butler, A. H., Domeisen, D. I. V., Kretschmer, M., Lawrence, Z., et al. (2022). Northern Hemisphere Stratosphere-Troposphere Circulation Change in CMIP6 Models: 1. Inter-Model Spread and Scenario Sensitivity. *Journal of Geophysical Research: Atmospheres*, *127*(18), e2022JD036992. https://doi.org/10.1029/2022JD036992

Kenyon, J., & Hegerl, G. C. (2008). Influence of Modes of Climate Variability on Global Temperature Extremes. *Journal of Climate*, *21*(15), 3872–3889. https://doi.org/10.1175/2008JCLI2125.1

Kidston, J., Scaife, A. A., Hardiman, S. C., Mitchell, D. M., Butchart, N., Baldwin, M. P., & Gray, L. J. (2015). Stratospheric influence on tropospheric jet streams, storm tracks and surface weather. *Nature Geoscience*, *8*(6), 433–440. https://doi.org/10.1038/ngeo2424

Kim, B.-M., Son, S.-W., Min, S.-K., Jeong, J.-H., Kim, S.-J., Zhang, X., et al. (2014). Weakening of the stratospheric polar vortex by Arctic sea-ice loss. *Nature Communications*, *5*(1), 4646. https://doi.org/10.1038/ncomms5646

Kim, H., Caron, J. M., Richter, J. H., & Simpson, I. R. (2020). The Lack of QBO-MJO Connection in CMIP6 Models. *Geophysical Research Letters*, *47*(11), e2020GL087295. https://doi.org/10.1029/2020GL087295

Kobayashi, S., Ota, Y., Harada, Y., Ebita, A., Moriya, M., Onoda, H., et al. (2015). The JRA-55 Reanalysis: General Specifications and Basic Characteristics. *気象集誌. 第 2 輯*, *93*(1), 5–48. https://doi.org/10.2151/jmsj.2015-001

Kodera, K., Mukougawa, H., & Fujii, A. (2013). Influence of the vertical and zonal propagation of stratospheric planetary waves on tropospheric blockings. *Journal of Geophysical Research: Atmospheres*, *118*(15), 8333–8345. https://doi.org/10.1002/jgrd.50650

Kodera, K., Mukougawa, H., Maury, P., Ueda, M., & Claud, C. (2016). Absorbing and reflecting sudden stratospheric warming events and their relationship with tropospheric circulation. *Journal of Geophysical Research: Atmospheres*, *121*(1), 80–94. https://doi.org/10.1002/2015JD023359

Kolstad, E. W., & Charlton-Perez, A. J. (2011). Observed and simulated precursors of stratospheric polar vortex anomalies in the Northern Hemisphere. *Climate Dynamics*, *37*(7), 1443–1456. https://doi.org/10.1007/s00382-010-0919-7

Kolstad, E. W., Breiteig, T., & Scaife, A. A. (2010). The association between stratospheric weak polar vortex events and cold air outbreaks in the Northern Hemisphere. *Quarterly Journal of the Royal Meteorological Society*, *136*(649), 886–893. https://doi.org/10.1002/qj.620

Kolstad, E. W., Lee, S. H., Butler, A. H., Domeisen, D. I. V., & Wulff, C. O. (2022). Diverse Surface Signatures of Stratospheric Polar Vortex Anomalies. *Journal of Geophysical Research: Atmospheres*, *127*(20). https://doi.org/10.1029/2022JD037422

Kretschmer, M., Cohen, J., Matthias, V., Runge, J., & Coumou, D. (2018). The different stratospheric influence on cold-extremes in Eurasia and North America. *Npj Climate and Atmospheric Science*, *1*(1), 44. https://doi.org/10.1038/s41612-018-0054-4

Kushner, P. J., & Polvani, L. M. (2004). Stratosphere–Troposphere Coupling in a Relatively Simple AGCM: The Role of Eddies. *Journal of Climate*, *17*(3), 629–639. https://doi.org/10.1175/1520-0442(2004)017<0629:SCIARS>2.0.CO;2

Labe, Z., Peings, Y., & Magnusdottir, G. (2019). The Effect of QBO Phase on the Atmospheric Response to Projected Arctic Sea Ice Loss in Early Winter. *Geophysical Research Letters*, *46*(13), 7663–7671. https://doi.org/10.1029/2019GL083095

Lawrence, Z. D., Perlwitz, J., Butler, A. H., Manney, G. L., Newman, P. A., Lee, S. H., & Nash, E. R. (2020). The Remarkably Strong Arctic Stratospheric Polar Vortex of Winter 2020: Links to Record-Breaking Arctic Oscillation and Ozone Loss. *Journal of Geophysical Research: Atmospheres*, *125*(22), e2020JD033271. https://doi.org/10.1029/2020JD033271

Lee, S. H. (2021). The January 2021 sudden stratospheric warming. *Weather*, *76*(4), 135–136. https://doi.org/10.1002/wea.3966

Lee, S. H., Furtado, J. C., & Charlton-Perez, A. J. (2019). Wintertime North American Weather Regimes and the Arctic Stratospheric Polar Vortex. *Geophysical Research Letters*, *46*(24), 14892–14900. https://doi.org/10.1029/2019GL085592

Lee, S. H., Polvani, L. M., & Guan, B. (2022). Modulation of Atmospheric Rivers by the Arctic Stratospheric Polar Vortex. *Geophysical Research Letters*, *49*(18), e2022GL100381. https://doi.org/10.1029/2022GL100381

Leung, L. R., & Qian, Y. (2009). Atmospheric rivers induced heavy precipitation and flooding in the western U.S. simulated by the WRF regional climate model. *Geophysical Research Letters*, *36*(3). https://doi.org/10.1029/2008GL036445

Liang, Z., Rao, J., Guo, D., Lu, Q., & Shi, C. (2022). Northern winter stratospheric polar vortex regimes and their possible influence on the extratropical troposphere. *Climate Dynamics*, *59*(11–12), 3741–3761. https://doi.org/10.1007/s00382-022-06494-9

Liess, S., & Geller, M. A. (2012). On the relationship between QBO and distribution of tropical deep convection. *Journal of Geophysical Research: Atmospheres*, *117*(D3). https://doi.org/10.1029/2011JD016317

Limpasuvan, V., Thompson, D. W. J., & Hartmann, D. L. (2004). The Life Cycle of the Northern Hemisphere Sudden Stratospheric Warmings. *Journal of Climate*, *17*(13), 2584–2596. https://doi.org/10.1175/1520-0442(2004)017<2584:TLCOTN>2.0.CO;2

Limpasuvan, V., Hartmann, D. L., Thompson, D. W. J., Jeev, K., & Yung, Y. L. (2005). Stratosphere-troposphere evolution during polar vortex intensification. *Journal of Geophysical Research: Atmospheres*, *110*(D24). https://doi.org/10.1029/2005JD006302

Lorenz, R., Stalhandske, Z., & Fischer, E. M. (2019). Detection of a Climate Change Signal in Extreme Heat, Heat Stress, and Cold in Europe From Observations. *Geophysical Research Letters*, *46*(14), 8363–8374. https://doi.org/10.1029/2019GL082062

Lu, H., Scaife, A. A., Marshall, G. J., Turner, J., & Gray, L. J. (2017). Downward Wave Reflection as a Mechanism for the Stratosphere–Troposphere Response to the 11-Yr Solar Cycle. *Journal of Climate*, *30*(7), 2395–2414. https://doi.org/10.1175/JCLI-D-16-0400.1

Lubis, S. W., Matthes, K., Omrani, N.-E., Harnik, N., & Wahl, S. (2016). Influence of the Quasi-Biennial Oscillation and Sea Surface Temperature Variability on Downward Wave Coupling in the Northern Hemisphere. *Journal of the Atmospheric Sciences*, *73*(5), 1943–1965. https://doi.org/10.1175/JAS-D-15-0072.1

Ma, S., & Zhu, C. (2019). Extreme Cold Wave over East Asia in January 2016: A Possible Response to the Larger Internal Atmospheric Variability Induced by Arctic Warming. *Journal of Climate*, *32*(4), 1203–1216. https://doi.org/10.1175/JCLI-D-18-0234.1

Ma, W., & Chen, G. (2022). What Controls the Interannual Variability of the Boreal Winter Atmospheric River Activities over the Northern Hemisphere? *Journal of Climate*, *35*(23), 3955–3973. https://doi.org/10.1175/JCLI-D-22-0089.1

Ma, W., Chen, G., & Guan, B. (2020). Poleward Shift of Atmospheric Rivers in the Southern Hemisphere in Recent Decades. *Geophysical Research Letters*, *47*(21), e2020GL089934. https://doi.org/10.1029/2020GL089934

Martineau, P., Chen, G., & Burrows, D. A. (2017). Wave Events: Climatology, Trends, and Relationship to Northern Hemisphere Winter Blocking and Weather Extremes. *Journal of Climate*, *30*(15), 5675–5697. https://doi.org/10.1175/JCLI-D-16-0692.1

Martineau, P., Chen, G., Son, S.-W., & Kim, J. (2018). Lower-Stratospheric Control of the Frequency of Sudden Stratospheric Warming Events. *Journal of Geophysical Research: Atmospheres*, *123*(6), 3051–3070. https://doi.org/10.1002/2017JD027648

Martius, O., Polvani, L. M., & Davies, H. C. (2009). Blocking precursors to stratospheric sudden warming events. *Geophysical Research Letters*, *36*(14). https://doi.org/10.1029/2009GL038776

Matsuno, T. (1970). Vertical Propagation of Stationary Planetary Waves in the Winter Northern Hemisphere. *Journal of the Atmospheric Sciences*, *27*(6), 871–883. https://doi.org/10.1175/1520-0469(1970)027<0871:VPOSPW>2.0.CO;2

Maycock, A. C., & Hitchcock, P. (2015). Do split and displacement sudden stratospheric warmings have different annular mode signatures? *Geophysical Research Letters*, *42*(24), 10,943-10,951. https://doi.org/10.1002/2015GL066754

McIntyre, M. E. (1982). How Well do we Understand the Dynamics of Stratospheric Warmings? *Journal of the Meteorological Society of Japan. Ser. II*, *60*(1), 37–65. https://doi.org/10.2151/jmsj1965.60.1_37

Messori, G., Kretschmer, M., Lee, S. H., & Wendt, V. (2022). Stratospheric downward wave reflection events modulate North American weather regimes and cold spells. *Weather and Climate Dynamics*, *3*(4), 1215–1236. https://doi.org/10.5194/wcd-3-1215-2022

Millin, O. T., & Furtado, J. C. (2022). The Role of Wave Breaking in the Development and Subseasonal Forecasts of the February 2021 Great Plains Cold Air Outbreak. *Geophysical Research Letters*, *49*(21), e2022GL100835. https://doi.org/10.1029/2022GL100835

Mitchell, D. M., Gray, L. J., Anstey, J., Baldwin, M. P., & Charlton-Perez, A. J. (2013). The Influence of Stratospheric Vortex Displacements and Splits on Surface Climate. *Journal of Climate*, *26*(8), 2668–2682. https://doi.org/10.1175/JCLI-D-12-00030.1

Nakagawa, K. I., & Yamazaki, K. (2006). What kind of stratospheric sudden warming propagates to the troposphere? *Geophysical Research Letters*, *33*(4). https://doi.org/10.1029/2005GL024784

Nishii, K., Nakamura, H., & Orsolini, Y. J. (2011). Geographical Dependence Observed in Blocking High Influence on the Stratospheric Variability through Enhancement and Suppression of Upward Planetary-Wave Propagation. *Journal of Climate*, *24*(24), 6408–6423. https://doi.org/10.1175/JCLI-D-10-05021.1

Oldenborgh, G. J. van, Mitchell-Larson, E., Vecchi, G. A., Vries, H. de, Vautard, R., & Otto, F. (2019). Cold waves are getting milder in the northern midlatitudes. *Environmental Research Letters*, *14*(11), 114004. https://doi.org/10.1088/1748-9326/ab4867

Overland, J. E., Ballinger, T. J., Cohen, J., Francis, J. A., Hanna, E., Jaiser, R., et al. (2021). How do intermittency and simultaneous processes obfuscate the Arctic influence on midlatitude winter extreme weather events? *Environmental Research Letters*, *16*(4), 043002. https://doi.org/10.1088/1748-9326/abdb5d

Peings, Y., Labe, Z. M., & Magnusdottir, G. (2021). Are 100 Ensemble Members Enough to Capture the Remote Atmospheric Response to +2°C Arctic Sea Ice Loss? *Journal of Climate*, *34*(10), 3751–3769. https://doi.org/10.1175/JCLI-D-20-0613.1

Perera, A. T. D., Nik, V. M., Chen, D., Scartezzini, J.-L., & Hong, T. (2020). Quantifying the impacts of climate change and extreme climate events on energy systems. *Nature Energy*, *5*(2), 150–159. https://doi.org/10.1038/s41560-020-0558-0

Perlwitz, J., & Harnik, N. (2003). Observational Evidence of a Stratospheric Influence on the Troposphere by Planetary Wave Reflection. *Journal of Climate*, *16*(18), 3011–3026. https://doi.org/10.1175/1520-0442(2003)016<3011:OEOASI>2.0.CO;2

Perlwitz, J., & Harnik, N. (2004). Downward Coupling between the Stratosphere and Troposphere: The Relative Roles of Wave and Zonal Mean Processes. *Journal of Climate*, *17*(24), 4902–4909. https://doi.org/10.1175/JCLI-3247.1

Plumb, R. A. (1985). On the Three-Dimensional Propagation of Stationary Waves. *Journal of the Atmospheric Sciences*, *42*(3), 217–229. https://doi.org/10.1175/1520-0469(1985)042<0217:OTTDPO>2.0.CO;2

Pohlmann, H., Müller, W. A., Kulkarni, K., Kameswarrao, M., Matei, D., Vamborg, F. S. E., et al. (2013). Improved forecast skill in the tropics in the new MiKlip decadal climate

predictions. *Geophysical Research Letters*, *40*(21), 5798–5802. https://doi.org/10.1002/2013GL058051

Polvani, L. M., & Waugh, D. W. (2004). Upward Wave Activity Flux as a Precursor to Extreme Stratospheric Events and Subsequent Anomalous Surface Weather Regimes. *Journal of Climate*, *17*(18), 3548–3554. https://doi.org/10.1175/1520-0442(2004)017<3548:UWAFAA>2.0.CO;2

Randall, D. A., Tziperman, E., Branson, M. D., Richter, J. H., & Kang, W. (2023). The QBO–MJO Connection: A Possible Role for the SST and ENSO. *Journal of Climate*, *36*(18), 6515–6531. https://doi.org/10.1175/JCLI-D-23-0031.1

Rao, J., Garfinkel, C. I., & White, I. P. (2020). Impact of the Quasi-Biennial Oscillation on the Northern Winter Stratospheric Polar Vortex in CMIP5/6 Models. *Journal of Climate*, *33*(11), 4787–4813. https://doi.org/10.1175/JCLI-D-19-0663.1

Rao, J., Garfinkel, C. I., Ren, R., Wu, T., & Lu, Y. (2023). Southern Hemisphere Response to the Quasi-Biennial Oscillation in the CMIP5/6 Models. *Journal of Climate*, *1*(aop), 1–45. https://doi.org/10.1175/JCLI-D-22-0675.1

Reichler, T., & Jucker, M. (2022). Stratospheric wave driving events as an alternative to sudden stratospheric warmings. *Weather and Climate Dynamics*, *3*(2), 659–677. https://doi.org/10.5194/wcd-3-659-2022

Richter, J. H., Anstey, J. A., Butchart, N., Kawatani, Y., Meehl, G. A., Osprey, S., & Simpson, I. R. (2020). Progress in Simulating the Quasi-Biennial Oscillation in CMIP Models. *Journal of Geophysical Research: Atmospheres*, *125*(8), e2019JD032362. https://doi.org/10.1029/2019JD032362

Scaife, A. A., Athanassiadou, M., Andrews, M., Arribas, A., Baldwin, M., Dunstone, N., et al. (2014). Predictability of the quasi-biennial oscillation and its northern winter teleconnection on seasonal to decadal timescales. *Geophysical Research Letters*, *41*(5), 1752–1758. https://doi.org/10.1002/2013GL059160

Scaife, A. A., Baldwin, M. P., Butler, A. H., Charlton-Perez, A. J., Domeisen, D. I. V., Garfinkel, C. I., et al. (2022). Long-range prediction and the stratosphere. *Atmospheric Chemistry and Physics*, *22*(4), 2601–2623. https://doi.org/10.5194/acp-22-2601-2022

Schneidereit, A., Peters, D. H. W., Grams, C. M., Quinting, J. F., Keller, J. H., Wolf, G., et al. (2017). Enhanced Tropospheric Wave Forcing of Two Anticyclones in the Prephase of the January 2009 Major Stratospheric Sudden Warming Event. *Monthly Weather Review*, *145*(5), 1797–1815. https://doi.org/10.1175/MWR-D-16-0242.1

Seviour, W. J. M., Gray, L. J., & Mitchell, D. M. (2016). Stratospheric polar vortex splits and displacements in the high-top CMIP5 climate models. *Journal of Geophysical Research: Atmospheres*, *121*(4), 1400–1413. https://doi.org/10.1002/2015JD024178

Shaw, T. A., & Perlwitz, J. (2010). The Impact of Stratospheric Model Configuration on Planetary-Scale Waves in Northern Hemisphere Winter. *Journal of Climate*, *23*(12), 3369–3389. https://doi.org/10.1175/2010JCLI3438.1

Shaw, T. A., & Perlwitz, J. (2013). The Life Cycle of Northern Hemisphere Downward Wave Coupling between the Stratosphere and Troposphere. *Journal of Climate*, *26*(5), 1745–1763. https://doi.org/10.1175/JCLI-D-12-00251.1

Shaw, T. A., Perlwitz, J., & Harnik, N. (2010). Downward Wave Coupling between the Stratosphere and Troposphere: The Importance of Meridional Wave Guiding and Comparison with Zonal-Mean Coupling. *Journal of Climate*, *23*(23), 6365–6381. https://doi.org/10.1175/2010JCLI3804.1

Shaw, T. A., Perlwitz, J., & Weiner, O. (2014). Troposphere-stratosphere coupling: Links to North Atlantic weather and climate, including their representation in CMIP5 models. *Journal of Geophysical Research: Atmospheres*, *119*(10), 5864–5880. https://doi.org/10.1002/2013JD021191

Shen, X., Wang, L., Scaife, A. A., Hardiman, S. C., & Xu, P. (2022). The Stratosphere-Troposphere Oscillation as the Dominant Intraseasonal Coupling Mode between the Stratosphere and Troposphere. *Journal of Climate*, *36*(7), 2259–2276. https://doi.org/10.1175/JCLI-D-22-0238.1

Sigmond, M., Scinocca, J. F., Kharin, V. V., & Shepherd, T. G. (2013). Enhanced seasonal forecast skill following stratospheric sudden warmings. *Nature Geoscience*, *6*(2), 98–102. https://doi.org/10.1038/ngeo1698

Smith, D. M., Screen, J. A., Deser, C., Cohen, J., Fyfe, J. C., García-Serrano, J., et al. (2019). The Polar Amplification Model Intercomparison Project (PAMIP) contribution to CMIP6: investigating the causes and consequences of polar amplification. *Geoscientific Model Development*, *12*(3), 1139–1164. https://doi.org/10.5194/gmd-12-1139-2019

Smith, K. L., & Kushner, P. J. (2012). Linear interference and the initiation of extratropical stratosphere-troposphere interactions. *Journal of Geophysical Research: Atmospheres*, *117*(D13). https://doi.org/10.1029/2012JD017587

Smith, K. L., Neely, R. R., Marsh, D. R., & Polvani, L. M. (2014). The Specified Chemistry Whole Atmosphere Community Climate Model (SC-WACCM). *Journal of Advances in Modeling Earth Systems*, *6*(3), 883–901. https://doi.org/10.1002/2014MS000346

Song, Y., & Robinson, W. A. (2004). Dynamical Mechanisms for Stratospheric Influences on the Troposphere. *Journal of the Atmospheric Sciences*, *61*(14), 1711–1725. https://doi.org/10.1175/1520-0469(2004)061<1711:DMFSIO>2.0.CO;2

Stockdale, T. N., Kim, Y.-H., Anstey, J. A., Palmeiro, F. M., Butchart, N., Scaife, A. A., et al. (2022). Prediction of the quasi-biennial oscillation with a multi-model ensemble of QBO-resolving models. *Quarterly Journal of the Royal Meteorological Society*, *148*(744), 1519–1540. https://doi.org/10.1002/qj.3919

Sun, L., Robinson, W. A., & Chen, G. (2011). The Role of Planetary Waves in the Downward Influence of Stratospheric Final Warming Events. *Journal of the Atmospheric Sciences*, *68*(12), 2826–2843. https://doi.org/10.1175/JAS-D-11-014.1

Sun, L., Robinson, W. A., & Chen, G. (2012). The Predictability of Stratospheric Warming Events: More from the Troposphere or the Stratosphere? *Journal of the Atmospheric Sciences*, *69*(2), 768–783. https://doi.org/10.1175/JAS-D-11-0144.1

Sun, L., Deser, C., & Tomas, R. A. (2015). Mechanisms of Stratospheric and Tropospheric Circulation Response to Projected Arctic Sea Ice Loss. *Journal of Climate*, *28*(19), 7824–7845. https://doi.org/10.1175/JCLI-D-15-0169.1

Sun, L., Deser, C., Simpson, I., & Sigmond, M. (2022). Uncertainty in the Winter Tropospheric Response to Arctic Sea Ice Loss: The Role of Stratospheric Polar Vortex Internal Variability. *Journal of Climate*, *35*(10), 3109–3130. https://doi.org/10.1175/JCLI-D-21-0543.1

Tan, X., & Bao, M. (2020). Linkage Between a Dominant Mode in the Lower Stratosphere and the Western Hemisphere Circulation Pattern. *Geophysical Research Letters*, *47*(17). https://doi.org/10.1029/2020GL090105

Tatebe, H., Ogura, T., Nitta, T., Komuro, Y., Ogochi, K., Takemura, T., et al. (2019). Description and basic evaluation of simulated mean state, internal variability, and climate sensitivity in MIROC6. *Geoscientific Model Development*, *12*(7), 2727–2765. https://doi.org/10.5194/gmd-12-2727-2019

Thompson, D. W. J., & Wallace, J. M. (1998). The Arctic oscillation signature in the wintertime geopotential height and temperature fields. *Geophysical Research Letters*, *25*(9), 1297–1300. https://doi.org/10.1029/98GL00950

Thompson, D. W. J., Baldwin, M. P., & Wallace, J. M. (2002). Stratospheric Connection to Northern Hemisphere Wintertime Weather: Implications for Prediction. *Journal of Climate*, *15*(12), 1421–1428. https://doi.org/10.1175/1520-0442(2002)015<1421:SCTNHW>2.0.CO;2

Thompson, D. W. J., Furtado, J. C., & Shepherd, T. G. (2006). On the Tropospheric Response to Anomalous Stratospheric Wave Drag and Radiative Heating. *Journal of the Atmospheric Sciences*, *63*(10), 2616–2629. https://doi.org/10.1175/JAS3771.1

Tyrlis, E., Manzini, E., Bader, J., Ukita, J., Nakamura, H., & Matei, D. (2019). Ural Blocking Driving Extreme Arctic Sea Ice Loss, Cold Eurasia, and Stratospheric Vortex Weakening in Autumn and Early Winter 2016–2017. *Journal of Geophysical Research: Atmospheres*, *124*(21), 11313–11329. https://doi.org/10.1029/2019JD031085

Tyrlis, E., Bader, J., Manzini, E., Ukita, J., Nakamura, H., & Matei, D. (2020). On the role of Ural Blocking in driving the Warm Arctic–Cold Siberia pattern. *Quarterly Journal of the Royal Meteorological Society*, qj.3784. https://doi.org/10.1002/qj.3784

Vajda, A., Tuomenvirta, H., Juga, I., Nurmi, P., Jokinen, P., & Rauhala, J. (2014). Severe weather affecting European transport systems: the identification, classification and frequencies of events. *Natural Hazards*, *72*(1), 169–188. https://doi.org/10.1007/s11069-013-0895-4

Vigaud, N., Robertson, A. W., & Tippett, M. K. (2018). Predictability of Recurrent Weather Regimes over North America during Winter from Submonthly Reforecasts. *Monthly Weather Review*, *146*(8), 2559–2577. https://doi.org/10.1175/MWR-D-18-0058.1

Waliser, D., & Guan, B. (2017). Extreme winds and precipitation during landfall of atmospheric rivers. *Nature Geoscience*, *10*(3), 179–183. https://doi.org/10.1038/ngeo2894

Wang, L., Yang, H., Wen, Q., Liu, Y., & Wu, G. (2023). The Tibetan Plateau's Far-Reaching Impacts on Arctic and Antarctic Climate: Seasonality and Pathways. *Journal of Climate*, *36*(5), 1399–1414. https://doi.org/10.1175/JCLI-D-22-0175.1

White, I. P., Garfinkel, C. I., Cohen, J., Jucker, M., & Rao, J. (2021). The Impact of Split and Displacement Sudden Stratospheric Warmings on the Troposphere. *Journal of Geophysical Research: Atmospheres*, *126*(8). https://doi.org/10.1029/2020JD033989

Woollings, T., Charlton-Perez, A., Ineson, S., Marshall, A. G., & Masato, G. (2010). Associations between stratospheric variability and tropospheric blocking. *Journal of Geophysical Research*, *115*(D6), D06108. https://doi.org/10.1029/2009JD012742

Wright, C. J., Hall, R. J., Banyard, T. P., Hindley, N. P., Krisch, I., Mitchell, D. M., & Seviour, W. J. M. (2021). Dynamical and surface impacts of the January 2021 sudden stratospheric warming in novel Aeolus wind observations, MLS and ERA5. *Weather and Climate Dynamics*, *2*(4), 1283–1301. https://doi.org/10.5194/wcd-2-1283-2021

Wu, Z., & Reichler, T. (2020). Variations in the Frequency of Stratospheric Sudden Warmings in CMIP5 and CMIP6 and Possible Causes. *Journal of Climate*, *33*(23), 10305–10320. https://doi.org/10.1175/JCLI-D-20-0104.1

Xiang, B., Lin, S., Zhao, M., Johnson, N. C., Yang, X., & Jiang, X. (2019). Subseasonal Week 3–5 Surface Air Temperature Prediction During Boreal Wintertime in a GFDL Model. *Geophysical Research Letters*, *46*(1), 416–425. https://doi.org/10.1029/2018GL081314

Yalew, S. G., van Vliet, M. T. H., Gernaat, D. E. H. J., Ludwig, F., Miara, A., Park, C., et al. (2020). Impacts of climate change on energy systems in global and regional scenarios. *Nature Energy*, *5*(10), 794–802. https://doi.org/10.1038/s41560-020-0664-z

Yang, H., Sun, L., & Chen, G. (2015). Separating the Mechanisms of Transient Responses to Stratospheric Ozone Depletion–Like Cooling in an Idealized Atmospheric Model. *Journal of the Atmospheric Sciences*, *72*(2), 763–773. https://doi.org/10.1175/JAS-D-13-0353.1

Yu, Y., Cai, M., Ren, R., & Dool, H. M. van den. (2015). Relationship between Warm Airmass Transport into the Upper Polar Atmosphere and Cold Air Outbreaks in Winter.

Journal of the Atmospheric Sciences, *72*(1), 349–368. https://doi.org/10.1175/JAS-D-14-0111.1

Zhang, J., Xie, F., Ma, Z., Zhang, C., Xu, M., Wang, T., & Zhang, R. (2019). Seasonal Evolution of the Quasi-biennial Oscillation Impact on the Northern Hemisphere Polar Vortex in Winter. *Journal of Geophysical Research: Atmospheres*, *124*(23), 12568–12586. https://doi.org/10.1029/2019JD030966

Zhang, P., Wu, Y., Simpson, I. R., Smith, K. L., Zhang, X., De, B., & Callaghan, P. (2018). A stratospheric pathway linking a colder Siberia to Barents-Kara Sea sea ice loss. *Science Advances*, *4*(7), eaat6025. https://doi.org/10.1126/sciadv.aat6025

Zhang, P., Wu, Y., Chen, G., & Yu, Y. (2020). North American cold events following sudden stratospheric warming in the presence of low Barents-Kara Sea sea ice. *Environmental Research Letters*, *15*(12), 124017. https://doi.org/10.1088/1748-9326/abc215

Zhang, R., Screen, J. A., & Zhang, R. (2022). Arctic and Pacific Ocean Conditions Were Favorable for Cold Extremes over Eurasia and North America during Winter 2020/21. *Bulletin of the American Meteorological Society*, *103*(10), E2285–E2301. https://doi.org/10.1175/BAMS-D-21-0264.1

Zhu, Y., & Newell, R. E. (1998). A Proposed Algorithm for Moisture Fluxes from Atmospheric Rivers. *Monthly Weather Review*, *126*(3), 725–735. https://doi.org/10.1175/1520-0493(1998)126<0725:APAFMF>2.0.CO;2

Zou, C., & Zhang, R. (2024). Arctic Sea Ice Loss Modulates the Surface Impact of Autumn Stratospheric Polar Vortex Stretching Events. *Geophysical Research Letters*, *51*(3), e2023GL107221. https://doi.org/10.1029/2023GL107221

Zou, C., Zhang, R., Zhang, P., Wang, L., & Zhang, R. (2023). Contrasting physical mechanisms linking stratospheric polar vortex stretching events to cold Eurasia between autumn and late winter. *Climate Dynamics*. https://doi.org/10.1007/s00382-023-07030-z

Zuo, J., Xie, F., Yang, L., Sun, C., Wang, L., & Zhang, R. (2022). Modulation by the QBO of the Relationship between the NAO and Northeast China Temperature in Late Winter. *Journal of Climate*, *35*(24), 4395–4411. https://doi.org/10.1175/JCLI-D-22-0353.1